DOKUZ EYLÜL UNIVERSITY

GRADUATE SCHOOL OF NATURAL AND APPLIED SCIENCES

ENGINEERING GEOLOGY OF THE STATE HIGHWAY SLOPES BETWEEN BAĞARASI-FOÇA (İZMİR)

by

Mawuko Luke Yaw ANKAH

July, 2017

İZMİR

ENGINEERING GEOLOGY OF THE STATE HIGHWAY SLOPES BETWEEN BAĞARASI-FOÇA (İZMİR)

A Thesis Submitted to the
Graduate School of Natural and Applied Sciences of Dokuz Eylül University
In Partial Fulfillment of the Requirements for the Degree of Master of
Science in Geological Engineering, Applied Geology Program

by

Mawuko Luke Yaw ANKAH

July, 2017

İZMİR

M.Sc THESIS EXAMINATION RESULT FORM

We have read the thesis entitled **"ENGINEERING GEOLOGY OF THE STATE HIGHWAY SLOPES BETWEEN BAĞARASI-FOÇA (IZMIR)"** completed by **MAWUKO LUKE YAW ANKAH** under supervision of **ASSOC. PROF. DR. CEM KINCAL** and we certify that in our opinion it is fully adequate, in scope and in quality, as a thesis for the degree of Master of Science.

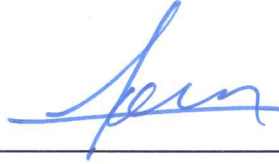Assoc. Prof. Dr. Cem KINCAL

Supervisor

Prof.Dr.M.Yalçın KOCA   Assist.Prof.Dr.Öznur KARACA

(Jury Member)   (Jury Member)

Prof.Dr. Emine İlknur CÖCEN

Director

Graduate School of Natural and Applied Sciences

ACKNOWLEDGEMENT

ENGINEERING GEOLOGY OF THE STATE HIGHWAY SLOPES BETWEEN BAĞARASI-FOÇA (İZMİR)

ABSTRACT

Slope failures frequently occur along the Bağarasi-Foça (Izmir) State Highway. The major rock formation in the study area is volcanic tuffs. Volcanic tuffs are weak rocks, and easily undergo weathering and slaking. A detailed geotechnical analysis including slope stability analysis of the state highway slopes was conducted using field works, laboratory works and software analyses. Field works conducted include geological mapping, scanline mapping and sample collection. Laboratory tests were conducted on highly, moderately and slightly weathered samples obtained from the field. Laboratory studies conducted include petrographic analysis, whole rock geochemical analysis, X-Ray Diffractometer (XRD) studies, porosity and unit weight tests, P-wave velocity (Vp) tests, uniaxial compressive strength (UCS) and triaxial compression tests, point load and slake durability index tests, Brazilian tests and direct shear strength tests. The rocks were classified as andesitic vitric and lithic tuffs and rhyolitic vitric and lithic tuffs based on the petrographic and geochemical studies. The main mineral identified from XRD analyses conducted on discontinuity infill material was smectite, an expansive clay mineral. The tuffs were classified as 'Very low-Low strength' based on the UCS tests and as 'Low-Moderate strength' based on sonic wave tests. Kinematic analysis conducted using Dips software indicate that the highway slopes have potentials of planar, wedge and toppling failures. The stability of the slopes were analysed using Phase^2 software (Strength Reduction Factor-SRF analysis) under non-seismic conditions (water saturated and dry conditions) and under seismic conditions of 0.1g and 0.2g. Results of the SRF analyses indicate that some slope panels of the highway have a high risk of failure while the others with lower failure risks could fail under increased pore water pressure or seismic conditions.

Keywords: Material properties, Volcanic tuff, Slope stability, Phase^2, XRD

BAĞARASI-FOÇA (İZMİR) ARASİNDAKİ KARAYOLU ŞEVLERİNİN MÜHENDİSLİK JEOLOJİSİ

ÖZ

Bağarası – Foça (İzmir) devlet karayolu boyunca şev yenilmeleri sıkça meydana gelmektedir. Çalışma alanındaki baskın jeolojik formasyon volkanik tüflerdir. Volkanik tüfler düşük dirençli kayaçlardır (zayıf kayaçlar) ve kolaylıkla ayrışıp, bozunabilirler. Saha araştırmaları, laboratuvar çalışmaları ve yazılım analiz verilerinin kullanıldığı devlet karayolu şevlerinin stabilite analizini içeren detaylı bir jeoteknik analiz yapılmıştır. Saha araştırmaları, jeolojik haritalama, hat etüdleri ve örnek alımını içermektedir. Laboratuvar çalışmaları sahadan temin edilmiş olan oldukça ayrışmış, orta derecede ayrışmış ve az ayrışmış örnekler üzerinde yapılmıştır. Petrografik analiz, tüm kayaç jeokimyasal analizi, X-ışını difraktometre çalışmasını, porozite ve birim hacim ağırlık testleri, P-dalga hızı testleri, tek eksenli basınç ve üç eksenli basınç testleri, nokta yükleme ve suda dağılmaya karşı direnç testleri, Brazilian indirekt çekme dayanımı ve direkt makaslama dayanımı testlerini kapsayan laboratuvar çalışmaları yapılmıştır. Kayaçlar petrografik ve jeokimyasal çalışmalara dayanarak; andezitik litik ve vitrik tüf ve riyolitik litik ve vitrik tüf olarak sınıflandırılmıştır. Süreksizlik dolgu malzemelerinden yapılmış olan XRD analizlerinde, şişebilen bir kil türü olan simektit tanımlanmıştır. Tüfler; tek eksenli basınç test sonuçlarına göre "Çok düşük-düşük dirençli", P-dalga hızı testlerine göre "düşük-orta dirençli" kayaçlar olarak sınıflandırılmıştır. Dips yazılımı kullanılarak yapılmış olan kinematik analizlere göre, devlet karayolu şevlerinde düzlemsel kayma, kama tipi kayma ve devrilme türü yenilme potansiyeli olduğu belirlenmiştir. Şevlerin stabilitesi Phase2 yazılımı (Gerilim azaltma faktörü analizi) kullanılarak, statik koşullarda (suya doygun ve kuru koşullar), 0.1 g ve 0.2 g sismik ivme verilerek analiz edilmiştir. SRF analiz sonuçları; bazı şev kesimlerinin yüksek yenilme riski varken, diğerlerinde ise düşük yenilme riski olduğunu göstermiştir. Düşük yenilme riskine sahip şevlerde, boşluk suyu basıncı ve sismik koşullarda artış meydana geldiğinde yenilme oluşabileceği yine SRF analizleriyle belirlenmiştir.

Anahtar kelimeler: Malzeme Özellikleri, Tüf, Şev stabilite, Phase^2, XRF

CONTENTS

LIST OF FIGURES

LIST OF TABLES

CHAPTER ONE
INTRODUCTION

1.1 Introduction

This study was conducted as a Master of Science Thesis in partial fulfillment of the requirements necessary for the award of a Master of Science Degree in Geological Engineering by the Graduate School of Natural and Applied Sciences, Dokuz Eylül University, Turkey.

1.2 Location and Accessibility of the Study Area

The study area (Figure 1.1) is located in Izmir, Turkey, on the Aegean coast between the towns of Bağarası and Foça at about 69 km (43 mi) northwest of Izmir city center. Transport to and from the study area is by bus. The area has a good road network with asphalted roads.
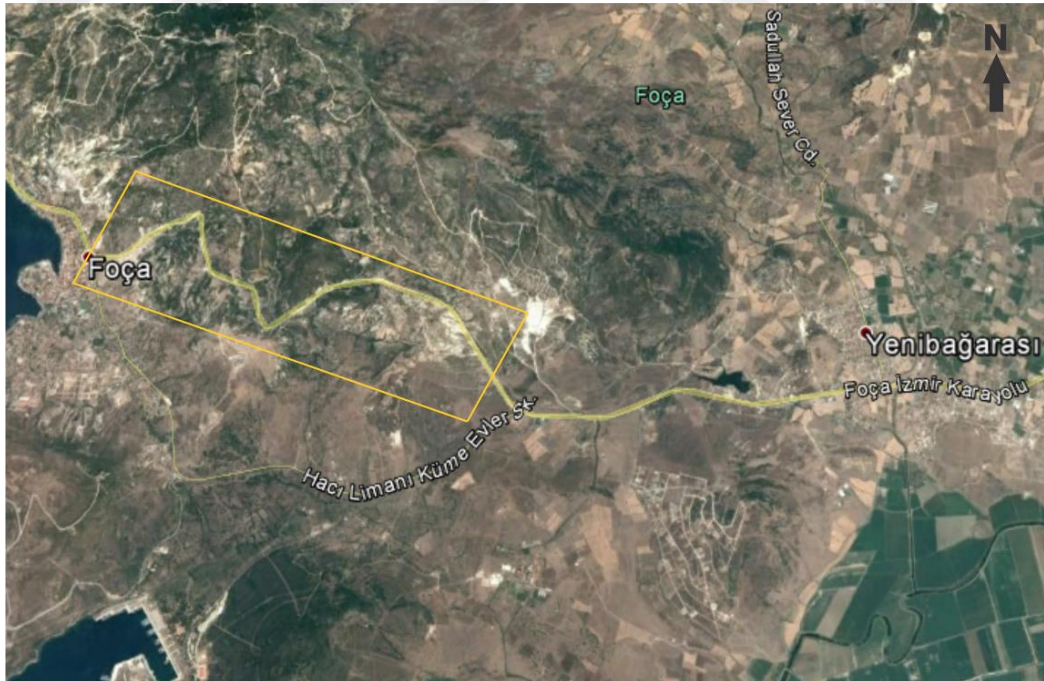
Figure 1.1 Location of the study area (Google Earth, 2016)

1.3 Aims of the study

The main rock formation in the study area is volcanic tuffs. Volcanic tuffs are weak rocks and easily undergo weathering and deformation (Muti, 2009). However, the highway was opened to traffic without considering the right slope angle/slope height, carrying out a thorough geotechnical analysis and conducting slope stability analysis.

Due to this, after rainy seasons, toppling failure as well as sliding frequently occurs in the volcanic tuffs along the state highway between Bağarası and Foça (Izmir). As a result of these failures the road is usually blocked to traffic. In addition, these failures may cause significant harm to both life and property.

The aim of this study, therefore, is to conduct a detailed geotechnical analysis including slope stability analysis of the State Highway Slopes.

1.4 Methods Used

1.4.1 Field Works

Detailed field studies of the entire study area was conducted. The lithologies in the study area were carefully studied and mapped. The lithologies mapped were volcanic tuff (vitric and lithic), basalt and rhyolite. A geological map of 1/10000 was prepared. Scanline mapping was conducted on the slopes of the Bağarası-Foça (Izmir) State Highway to obtain discontinuity data necessary for slope stability analysis. Block samples of different weathering grades (SW-HW) were collected from ten different locations along the State Highway Slope.

1.4.2 Laboratory Tests and Analyses

Laboratory tests and analyses were conducted on samples (SW-HW) from the ten locations (S1, S2, S3, SA, SB, SC, SD, SE, SF, and SG). Tests and analyses conducted include petrographic analyses on thin sections, whole rock chemical analysis, X-Ray Diffractometer analysis and various physico-mechanical property tests.

Physico-mechanical properties such as unit weight, compressive strength (uniaxial and triaxial), p-wave velocity as well as point load and slake durability indices were determined from the physico-mechanical laboratory tests.

1.4.3 Slope Stability Analyses

Slope stability analyses were conducted to assess the stability state of the Bağarası-Foça (Izmir) State Highway Slopes. Dips and Phase^2 software (by Rocscience) were used in conducting the slope stability analyses.

CHAPTER TWO
GEOLOGY OF THE STUDY AREA

2.1 Introduction

The study area falls within the western coast of the Aegean region. Akay (2000) and Akay & Erdogan (2004) identified three different suites of volcanic rocks in the Foca region. These are (from youngest to oldest): The Foça alkaline volcanic rocks, Foca volcanic rocks and the Yuntdag volcanic rocks.

Agostini et al. (2010) reported that the Foca volcanics consist of pyroclastics, volcano-sedimentary series, lava flows and domes of calc-alkaline rocks which are overlain and crosscut by younger lavas and NW-trending dikes. Savascin (1978) used a cross-cut relationship to date the Foca tuff as older than 16 Ma. Altunkaynak & Yilmaz (2000) however dated the Foca Tuffs to be between 15.5 and 14.5 Ma.

In this study, detailed geological mapping was conducted in the study area. The lithologies mapped in the study area (from oldest to youngest) were:

 i.   fine-grained (vitric) volcanic tuff unit,
 ii.   lithic tuff unit,
 iii. rhyolite unit,
 iv.   basalt dikes (width of about 8m), and
 v.   Quaternary sediments (alluvium).

Basalt dikes intruded the vitric and lithic tuffs. These dikes formed unconformable contacts with the tuffs. A number of N-E trending faults were observed in the tuffs. A 1/10000 scale geological map (Figure 2.1, Appendix 1) of the study area was prepared. A geological cross-section of the study area is presented in Figure 2.2.
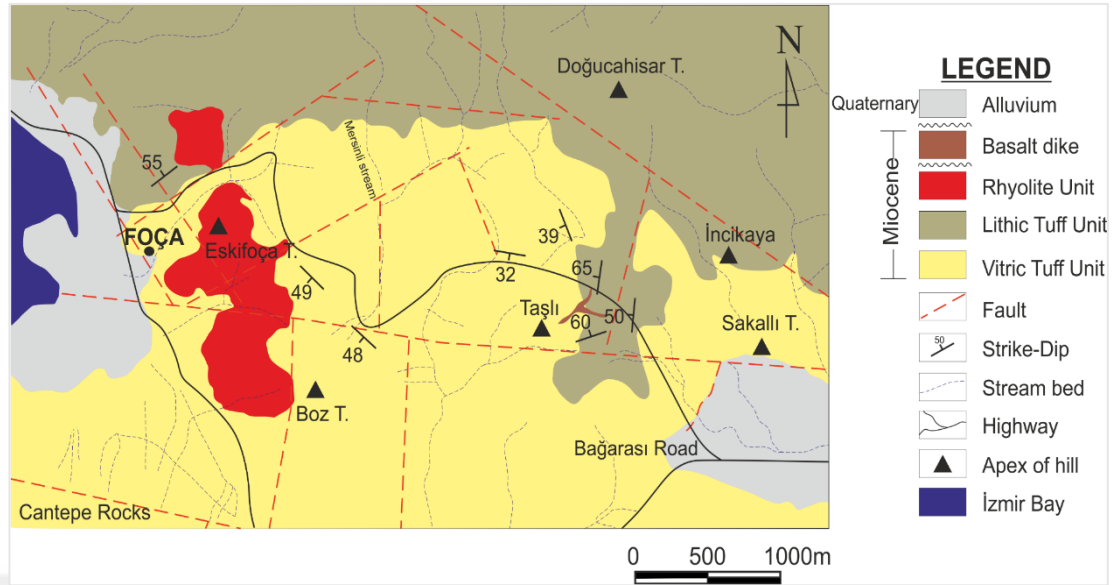
Figure 2.1 General geology map of the study area
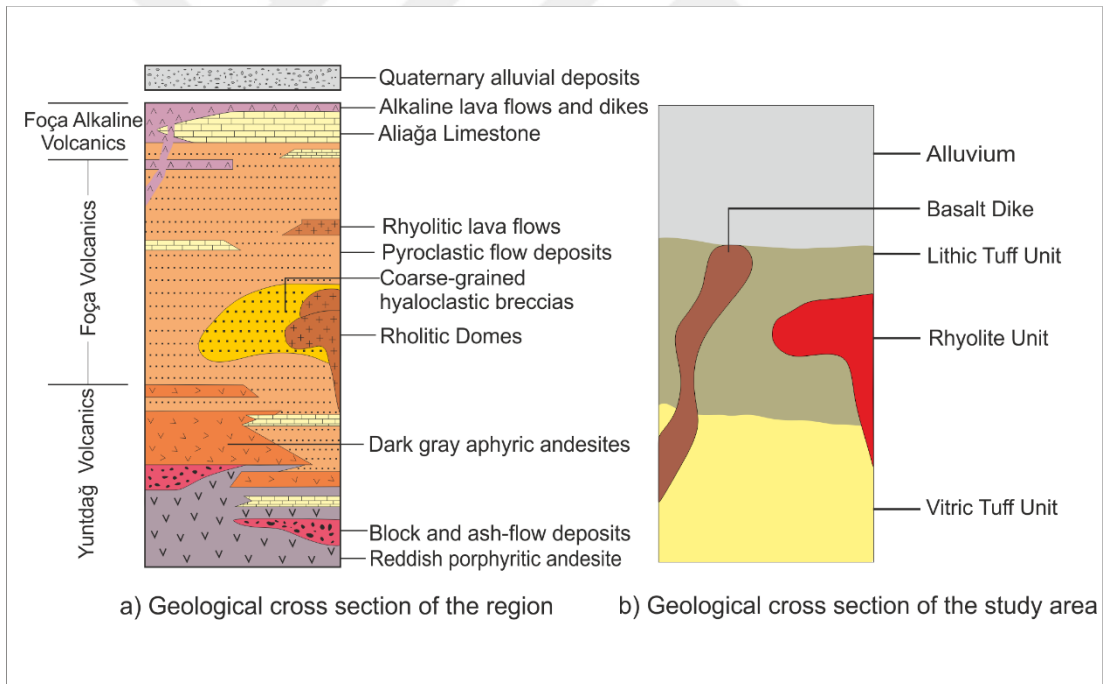
Figure 2.2 a) Geological cross section of the region (Modified after Akay, 2000) and b) Geological cross section of the study area

5

2.1 Lithological Units

2.1.1 Vitric Tuff Unit

The oldest lithological unit in the study area is the Vitric Tuff (Figure 2.3). The Vitric Tuff (VT) covers a significant section of the study area and the best outcrops of this rock unit were observed at Sakkali Hill and Boz Hill. The VT varied in colour from creamy-white to whitish gray. The VT was observed to generally have weak strength with significant indentation when struck with a geological hammer.

The vitric tuffs were generally highly fractured with glass fragment size less than 4 mm. The VT was observed to have high weathering degrees. The glass fragments had varied shapes-linear, circular and squares. The VT directly overlies the Yuntdag volcanics.

Figure 2.3 Vitric tuff

2.1.2 Lithic Tuff Unit

The Lithic Tuff (LT) unit outcrops predominantly on the hills found at the northern part of the study area with minor extensions towards the southern parts. The LT varies in colour from ash to brown. The LT was found to be of medium strength with little indentation when struck with a geological hammer. The lithic tuffs were formed from a consolidation of volcanic ash and rock fragments. Discontinuities in the LT were fewer in number compared to those observed in VT. The LT also had a generally lower degree of weathering compared to the VT.

Hand specimen examination indicated that the LT consisted mainly of over 60% rock fragments, mineral particles and fine material (volcanic glass). The rock fragments had a particle size range of 1 cm - 5 cm. The LT directly overlies the vitric tuffs. An image of the lithic tuff unit observed in the field is presented in Figure 2.4.

Figure 2.4 Lithic tuff

2.1.3 Rhyolite Unit

The best outcrops of the Rhyolite Unit (RU) were observed on Eskifoça Hill. Both fresh and weathered surface of the RU were pink in colour. The RU was massive and generally slightly weathered. Field tests (blows of geological hammer) of the strength of the RU indicated that it was of high strength.

No flow structure was observed in the rhyolite. Akay (2004) observed that the Rhyolite Unit in the study area had a dome structure. This explains why no flow structure was observed in the RU. Microcrystalline textures were observed in the rhyolite in thin section analysis. An image of the Rhyolite Unit is presented in Figure 2.5.

Figure 2.5 Rhyolite unit

2.1.4 Basalt Unit

The Basalt Unit (BU) outcrops north-west of the Taşli Hill. The BU formed as an intrusion (dike) in the volcanic tuffs. The BU has a massive structure with a brownish gray to dark brown colour. Cooling and shrinkage joints were observed in the unit. Flow structures were also observed in the unit. The BU generally had an aphanitic texture. Key mineral components observed in the BU were plagioclase and pyroxene. Plagioclase occurs as both phenocrysts and matrix in basalts (Nakipoğlu, 1994). An image of the BU is presented in Figure 2.6.

Figure 2.6 Basalt dike

2.1.5 Alluvium Unit

The Alluvium Unit (AU) outcrops in the southwestern and western part of the study area. The AU is composed of pebbles, sand and silt sized granules. The unit lies unconformably over the vitric tuff and basalt dike.

2.2 Structural Geology

The study area is located in the Foça depression, which forms part of the Middle East Aegean Depression. The Foça depression is the product of vertical displacements along the main N-NE trending structural facies (Kaya, 1978). Small scale faults are present in the study area (Figure 2.7).

Figure 2.7 Normal fault observed in the study area

The main structures in the study area originated from volcanism. These structures are volcanic fractures and joints. Tectonic activities caused a change in the strike and dip of the miocene vitric tuff unit (the oldest unit in the study area) and the development of faults. The vitric tuff has a strike direction of NW-SE with dip amounts varying from 30 degrees to 50 degrees. The beds dip in the South-Western (SW) direction.

After the formation of the vitric tuff unit, a new episode of volcanic activities led to the formation of the lithic tuffs directly above the vitric tuffs. Renewed volcanism caused the formation of the Basalt Unit which cross-cut the volcanic tuffs.

Flow structures are generally in the NE direction. Cooling fissures are usually associated with the flow structures (Nakipoğlu, 1994). In the study area, fracture and joint systems (Figure 2.8) developed after volcanism.

Figure 2.8 Fractures and joints

2.3 Geomorphology

Generally, the highest elevations in the study area are Eski Foça Hills, Boz Hill, Dogucahisar Hill and Sakalli Hill. The lowest elevations are the Eski Foça settlement area and surroundings. The vegetation in the study area is quite dense. The study area has a Mediterranean climate, which is typically associated with shrubs. Near the settlement areas, olive farming and horticulture are common. The most important rivers in the region are SW flowing Reşitbey Stream, NE flowing Karaman Stream, SW flowing Foça Stream, and the south flowing Mersin Stream.

CHAPTER THREE

MINERALOGICAL, PETROGRAPHICAL AND GEOCHEMICAL STUDY

3.1 Mineralogy and Petrography

Petrographic studies were conducted on 22 thin sections prepared from samples obtained from ten different locations along the Foca-Bagarasi (Izmir) State highway slope. These locations (slopes) are designated as Slope 1 (S1), Slope 2 (S2), Slope 3 (S3), Slope A (SA), Slope B (SB), Slope C (SC), Slope D (SD), Slope E (SE), Slope F (SF) and Slope G (SG). The samples had different weathering grades (SW-HW). Separate petrographic analyses were conducted for each of the ten sample groups. Images of rock specimens from the ten slopes are presented in Figure 3.1.
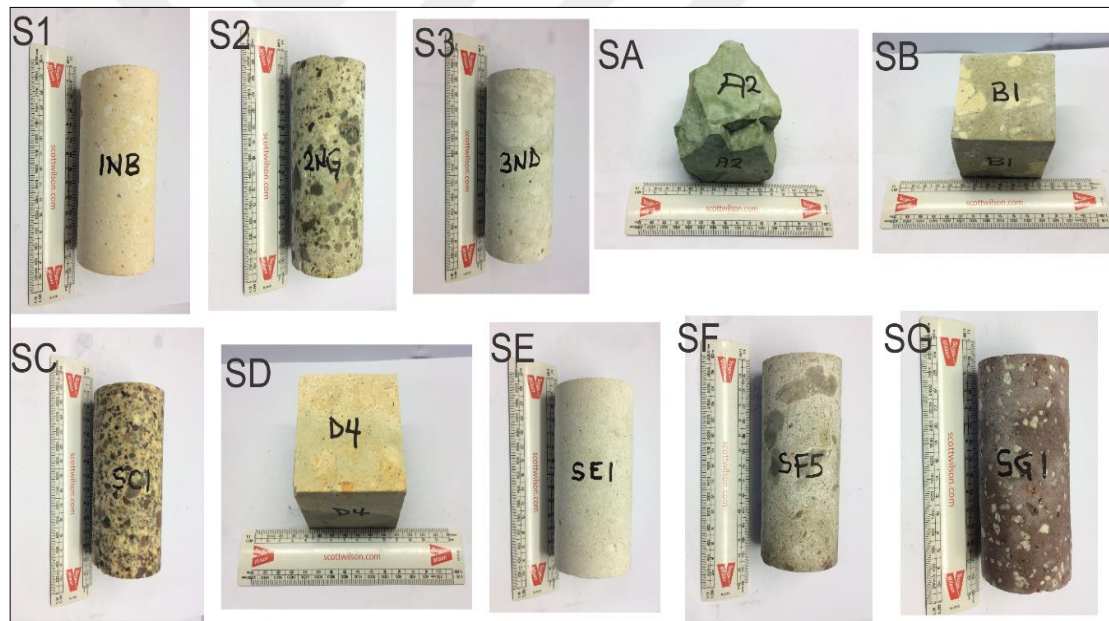
Figure 3.1 Images of rock specimens from the ten slopes

The thin sections (except SG) were primarily composed of volcanic glass, mineral particles and lithic fragments. Minerals that were identified in the thin sections include plagioclase, orthoclase (sanidine), pyroxene, biotite and quartz. Quartz was observed in all the thin sections except S1, S2 and S3, which were rich in plagioclase. The matrix of the specimens were principally made up of glass shards, pumice, quartz and calcite.

Chalcedony, formed from devitrified volcanic glass, was observed in some of the thin sections (SB, SC, SE and SF). Flow banding was also observed in the petrographic analyses. Flow banding and glassy matrixes are associated with pyroclastic flows. SG is the only sample group in which pyroclastic textures were not observed.

SG was composed of a large quantity of quartz, a quartz rich matrix, sanidine and biotite. SG was classified as rhyolite using the Quartz-Alkali feldspar-Plagioclase-Feldspathoid (QAPF) diagram developed by IUGS (Streckeisen, 1980) for classifying volcanic rocks (Figure 3.2).
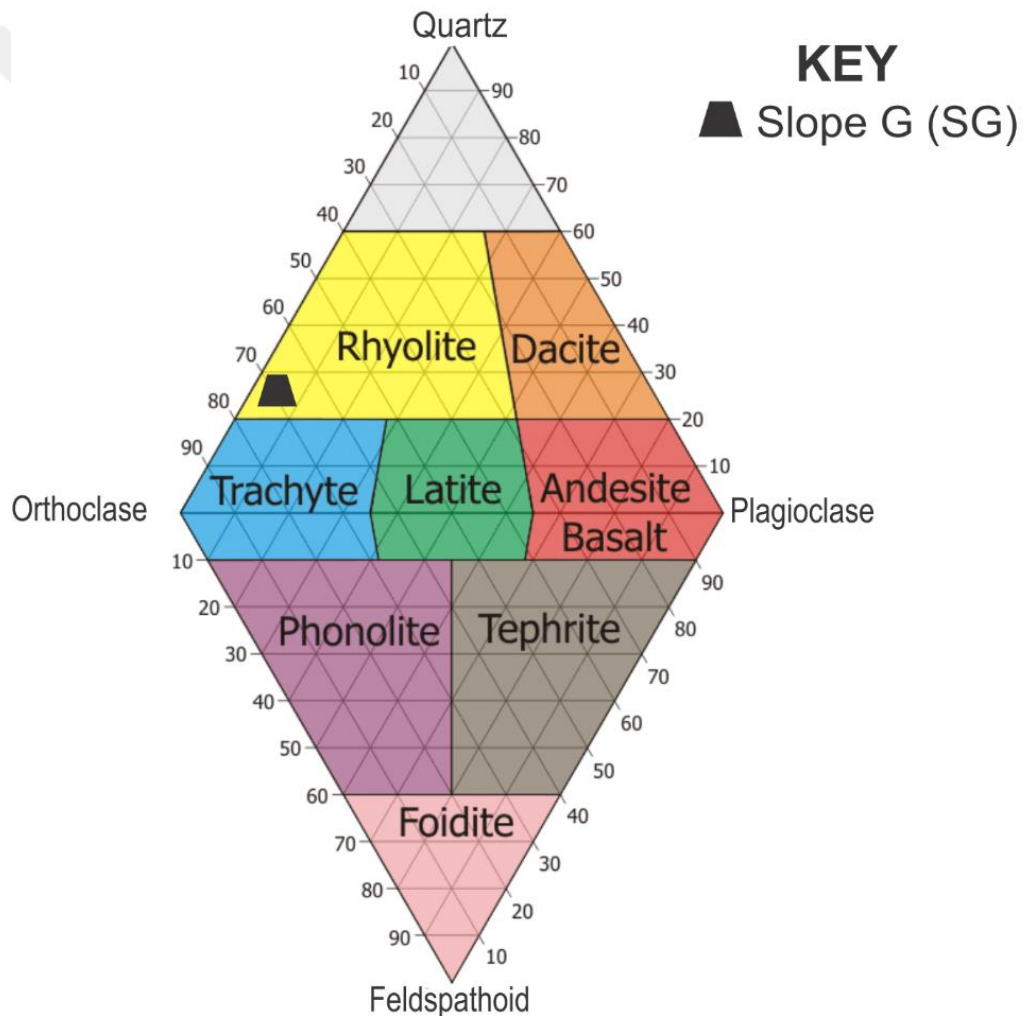
Figure 3.2 IUGS classification of Slope G (SG) (after Streckeisen, 1980)

13

The other sample groups (S1, S2, S3, SA, SB, SC, SD, SE and SF) were identified as volcanic tuffs and were classified as Lithic Tuff (LT) or Vitric Tuff (VT) using a Glass, Crystals and Rock fragments (GCR) diagram. S2 and SC had significant quantities of rock fragments and were classified as lithic tuffs. On the other hand, S1, S3, SA, SB, SD, SE and SF, had high quantities of volcanic glass as well as pumice and were therefore classified as vitric tuffs.

The relative compositions of glass, crystals and rock fragments in the thin sections were determined using visual estimation and plotted on a GCR diagram (after Pettijohn et al. 1987 and Andreis et al. 2007). The GCR compositions (%) of the specimens are contained in Table 3.1 while the GCR plot is presented in Figure 3.3.

Table 3.1 GCR compositions (%) of the various sample groups

Sample Group	Glass (%)	Crystals (%)	Rock fragments (%)
S1	86-90	6-10	1-4
S2	25-30	10-20	50-60
S3	80-95	5-20	0-10
SA	92-96	4-8	0
SB	70-75	10-20	10-15
SC	20-25	4-8	70-76
SD	90-94	1-4	3-7
SE	87-92	2-5	4-8
SF	60-65	4-7	30-35
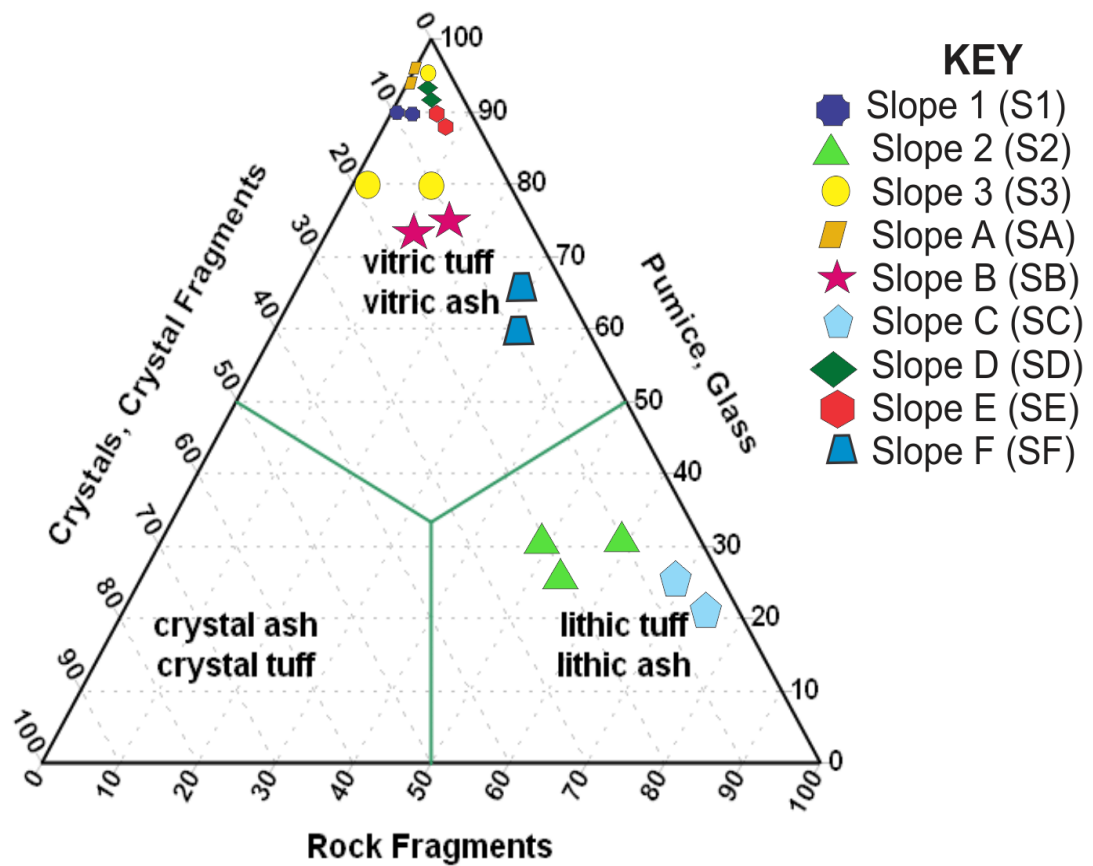
Figure 3.3 relative compositions of Glass, Crystals and Rock fragments (GCR) of the specimens (modified after Pettijohn et al. 1987 and Andreis et al. 2007)

Microscopic images of the thin sections of the various specimens are presented in Figure 3.4, 3.5, 3.6, 3.7, 3.8, 3.9, 3.10, 3.11, 3.12 and 3.13.
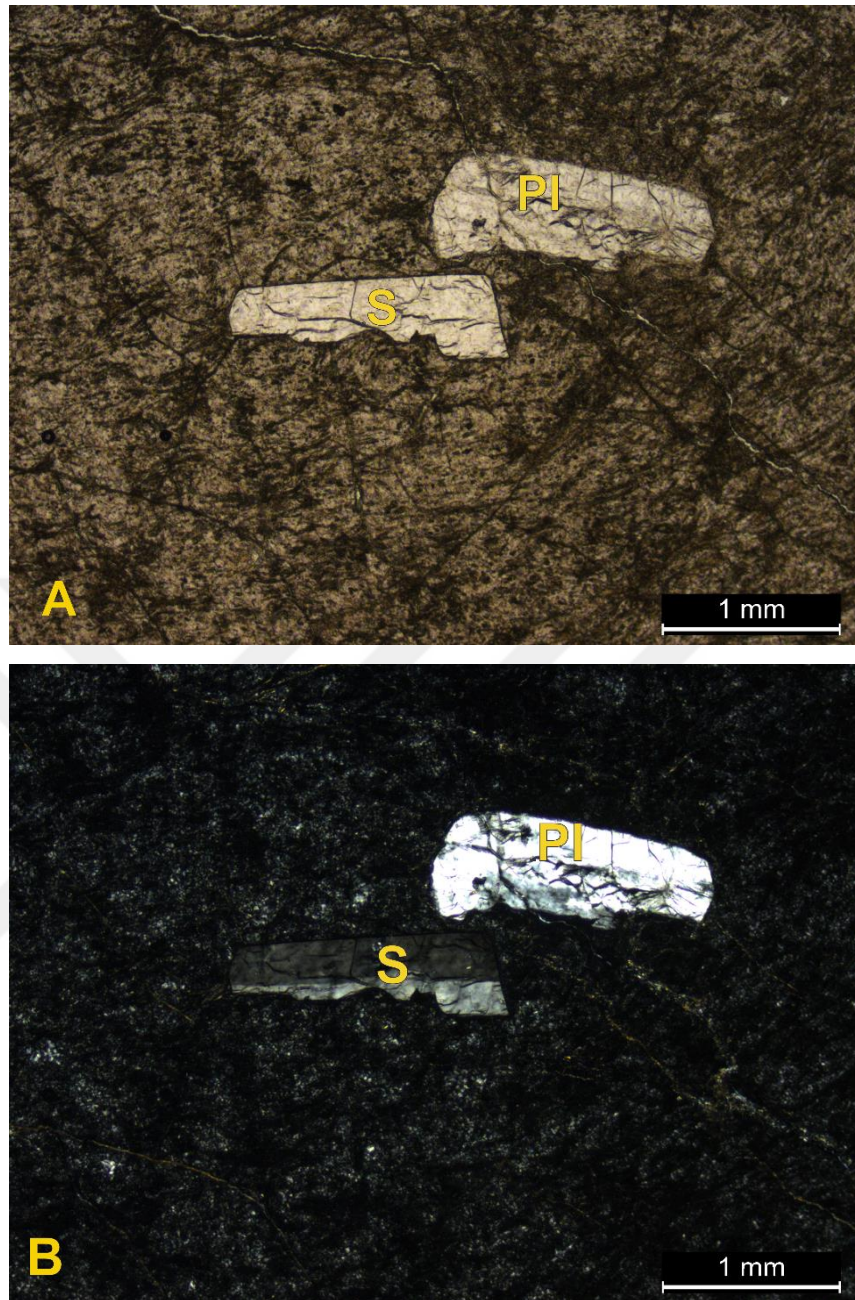
Figure 3.4 SA (HW vitric tuff) -Observations under Plane Polarised light (A) and Cross Polarised Light (B) (Pl-Plagioclase feldspar, F-Feldspar, Px-Pyroxene, Bt-Biotite, Rf-Rock fragment, S-Sanidine, Qtz-Quartz, Ch-Chalcedony formed from devitrified glass, Pm-Pumice)
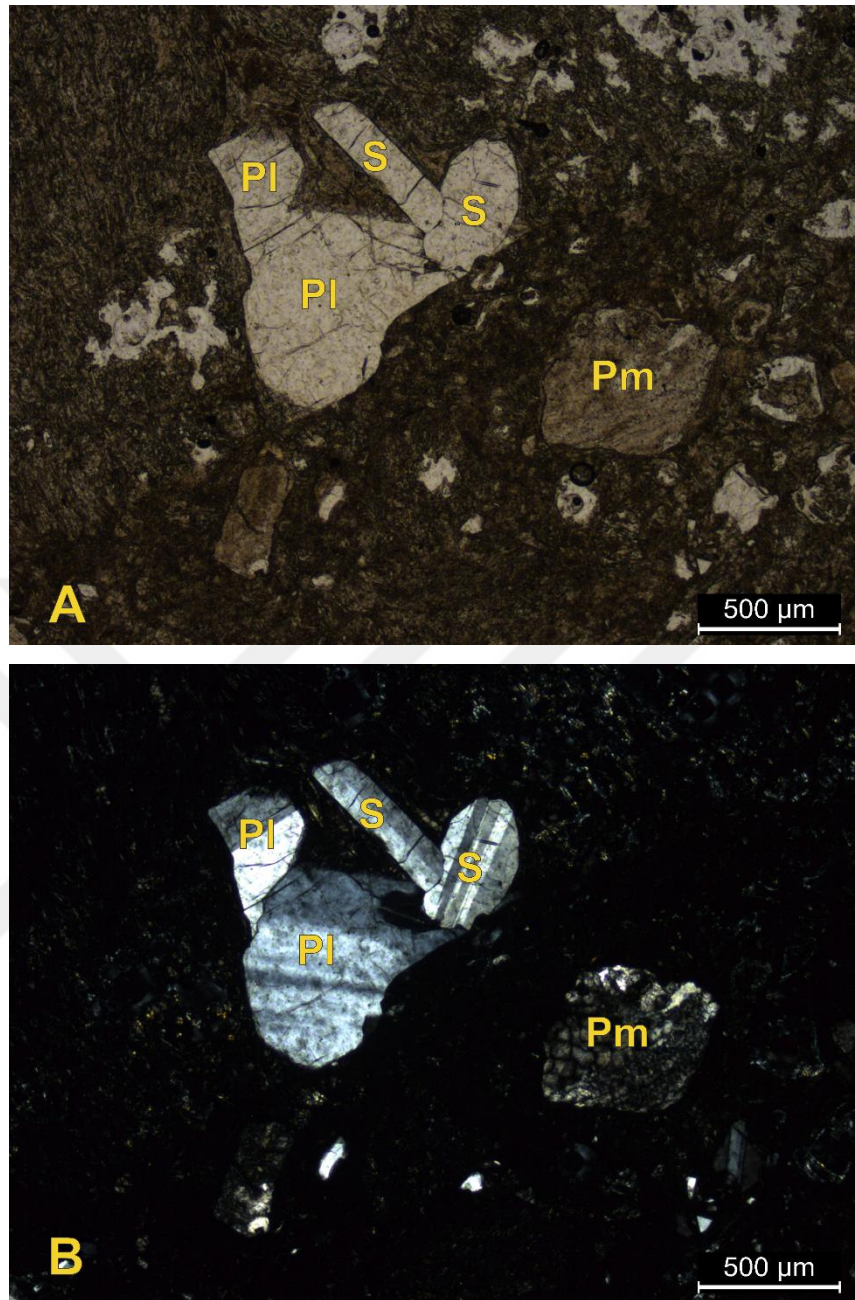
Figure 3.5 SB (MW vitric tuff)-Observations under Plane Polarised light (A) and Cross Polarised Light (B) (Pl-Plagioclase feldspar, F-Feldspar, Px-Pyroxene, Bt-Biotite, Rf-Rock fragment, S-Sanidine, Qtz-Quartz, Ch-Chalcedony formed from devitrified glass, Pm-Pumice)
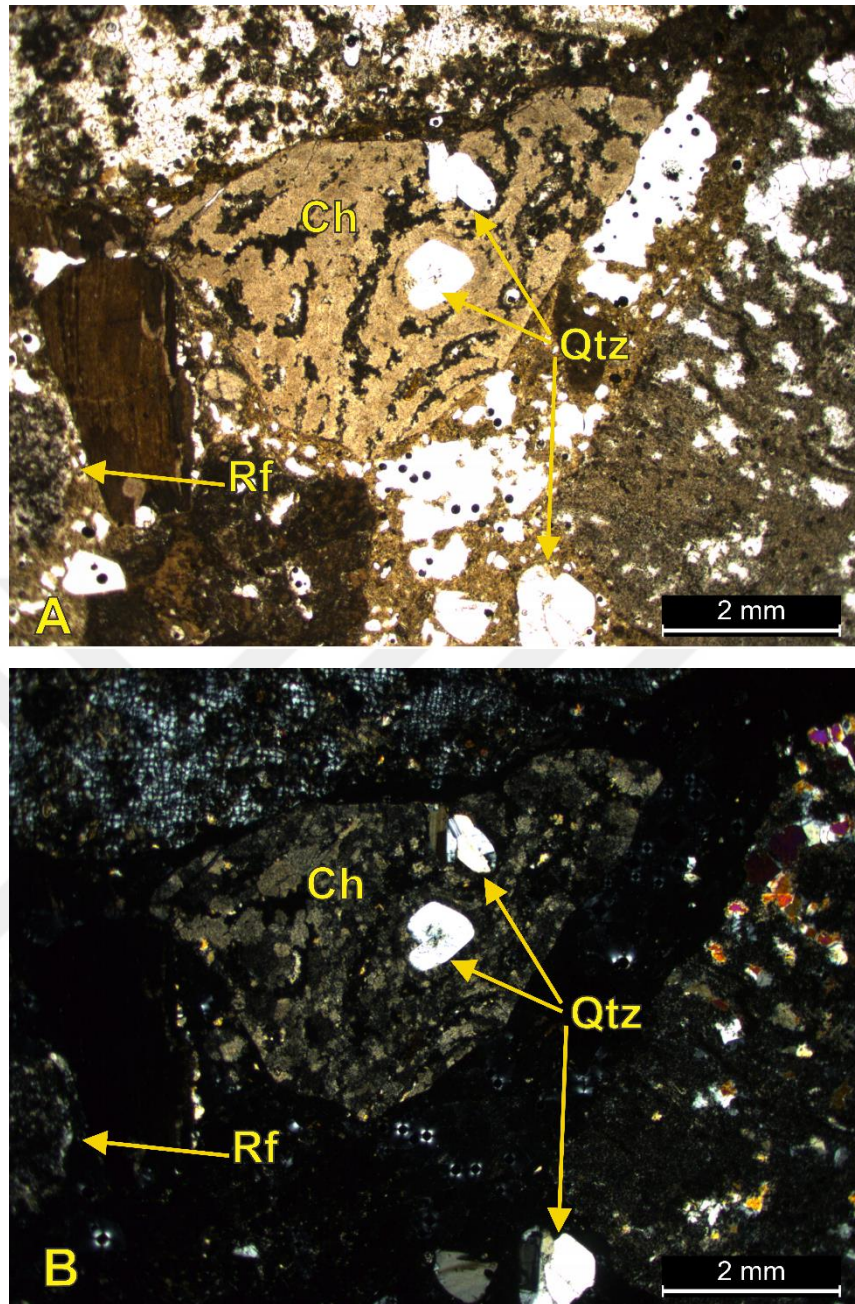
Figure 3.6 SC (SW lithic tuff) -Observations under Plane Polarised light (A) and Cross Polarised Light (B) (Pl-Plagioclase feldspar, F-Feldspar, Px-Pyroxene, Bt-Biotite, Rf-Rock fragment, S-Sanidine, Qtz-Quartz, Ch-Chalcedony formed from devitrified glass, Pm-Pumice)
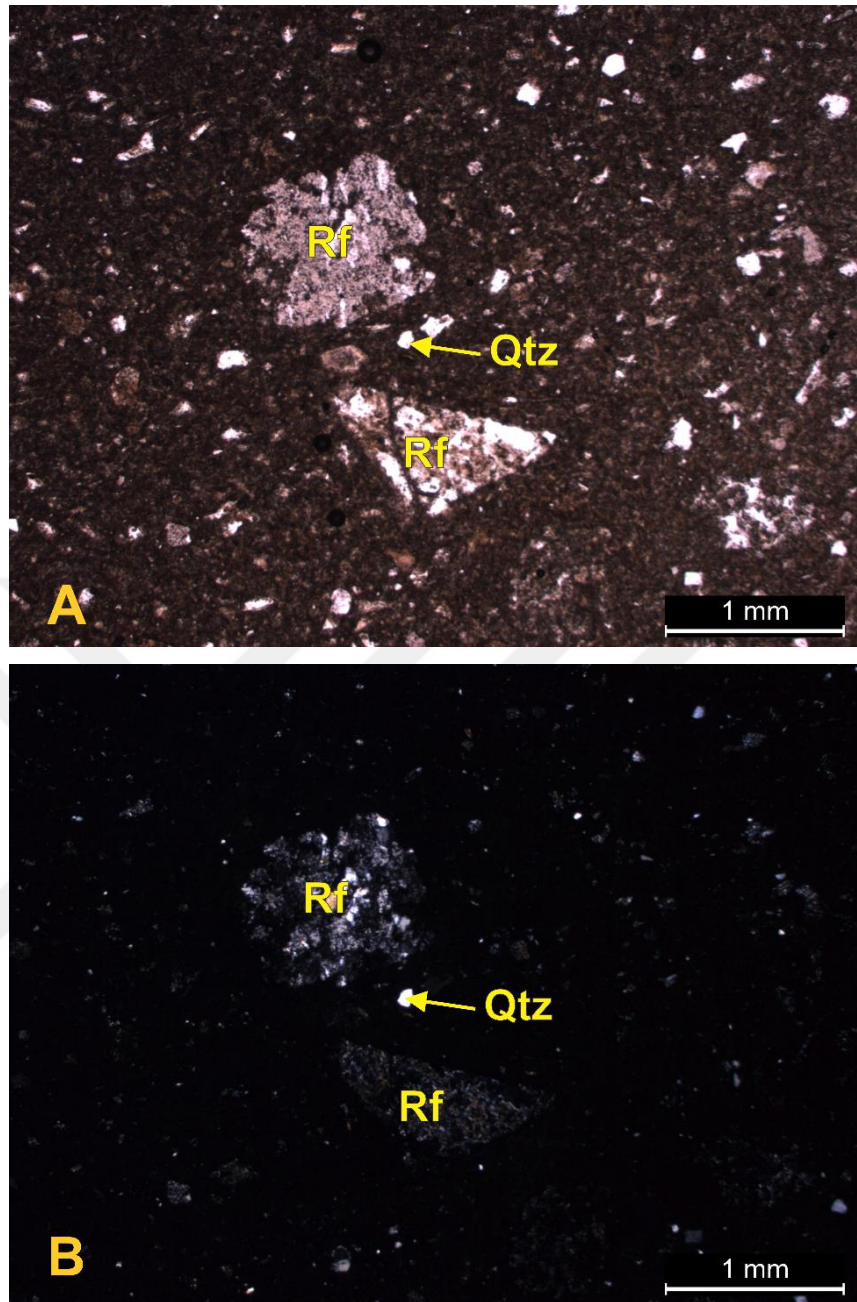
Figure 3.7 SD (HW vitric tuff) -Observations under Plane Polarised light (A) and Cross Polarised Light (B) (Pl-Plagioclase feldspar, F-Feldspar, Px-Pyroxene, Bt-Biotite, Rf-Rock fragment, S-Sanidine, Qtz-Quartz, Ch-Chalcedony formed from devitrified glass, Pm-Pumice)
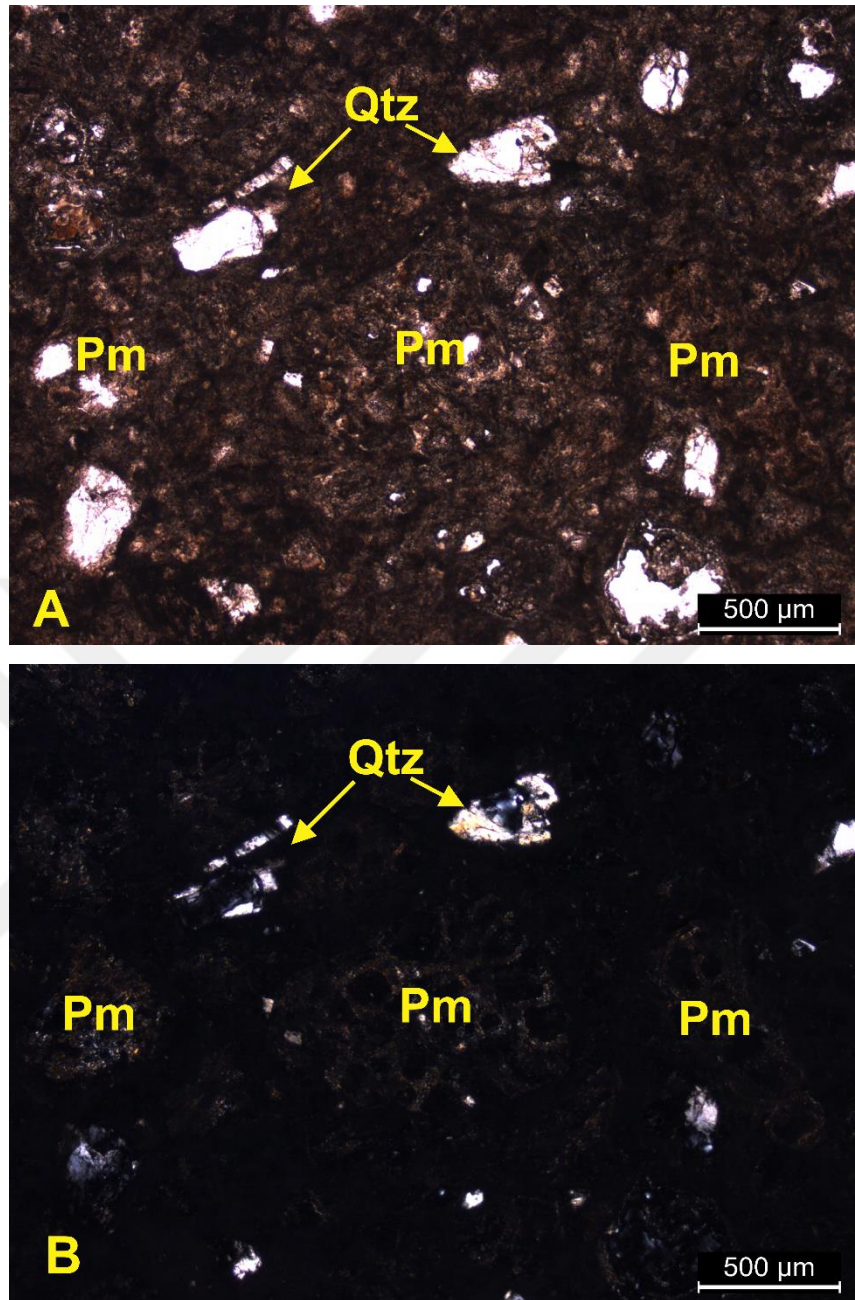
Figure 3.8 SE (MW vitric tuff) -Observations under Plane Polarised light (A) and Cross Polarised Light (B) (Pl-Plagioclase feldspar, F-Feldspar, Px-Pyroxene, Bt-Biotite, Rf-Rock fragment, S-Sanidine, Qtz-Quartz, Ch-Chalcedony formed from devitrified glass, Pm-Pumice)
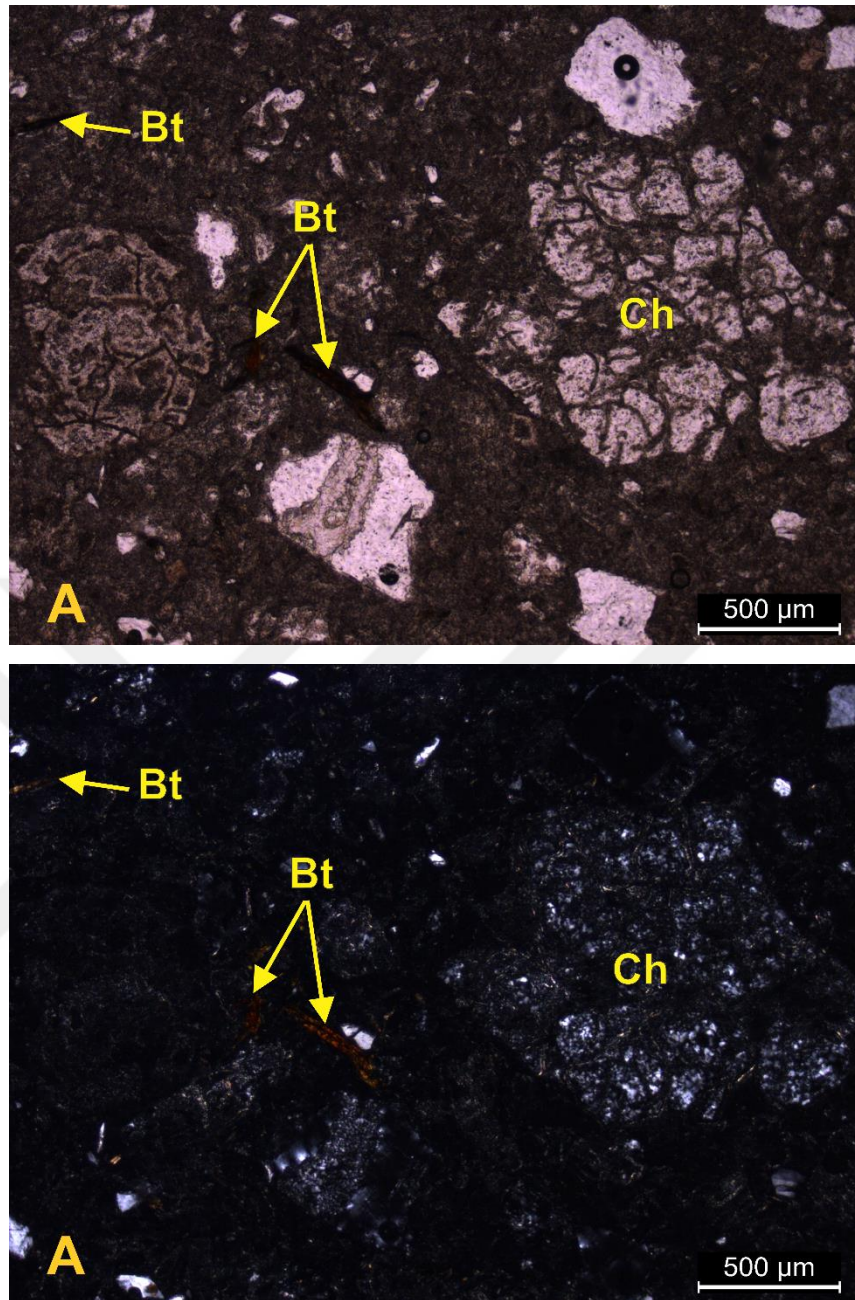
Figure 3.9 SF (MW vitric tuff) -Observations under Plane Polarised light (A) and Cross Polarised Light (B) (Pl-Plagioclase feldspar, F-Feldspar, Px-Pyroxene, Bt-Biotite, Rf-Rock fragment, S-Sanidine, Qtz-Quartz, Ch-Chalcedony formed from devitrified glass, Pm-Pumice)
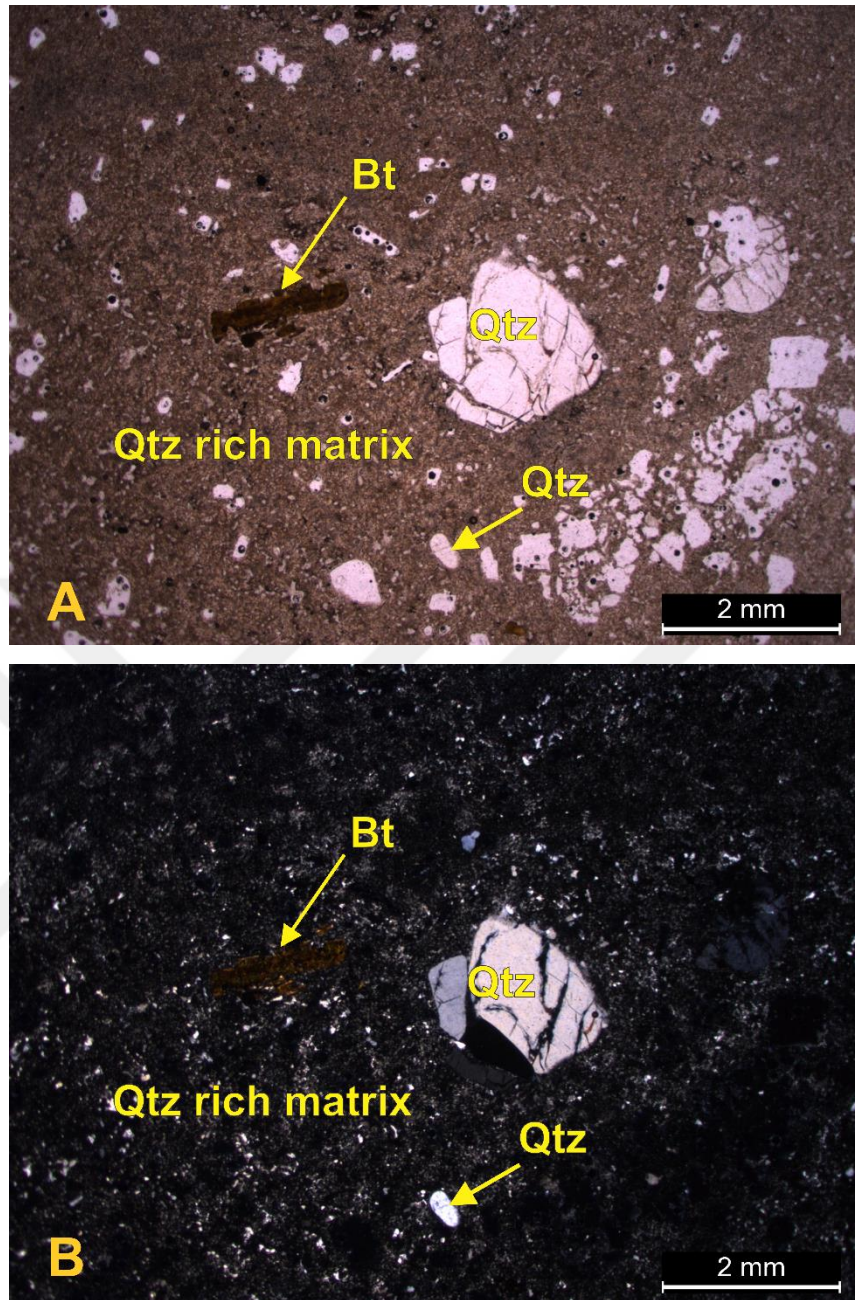
Figure 3.10 SG (Rhyolite)-Observations under Plane Polarised light (A) and Cross Polarised Light (B) (Pl-Plagioclase feldspar, F-Feldspar, Px-Pyroxene, Bt-Biotite, Rf-Rock fragment, S-Sanidine, Qtz-Quartz, Ch-Chalcedony formed from devitrified glass, Pm-Pumice)
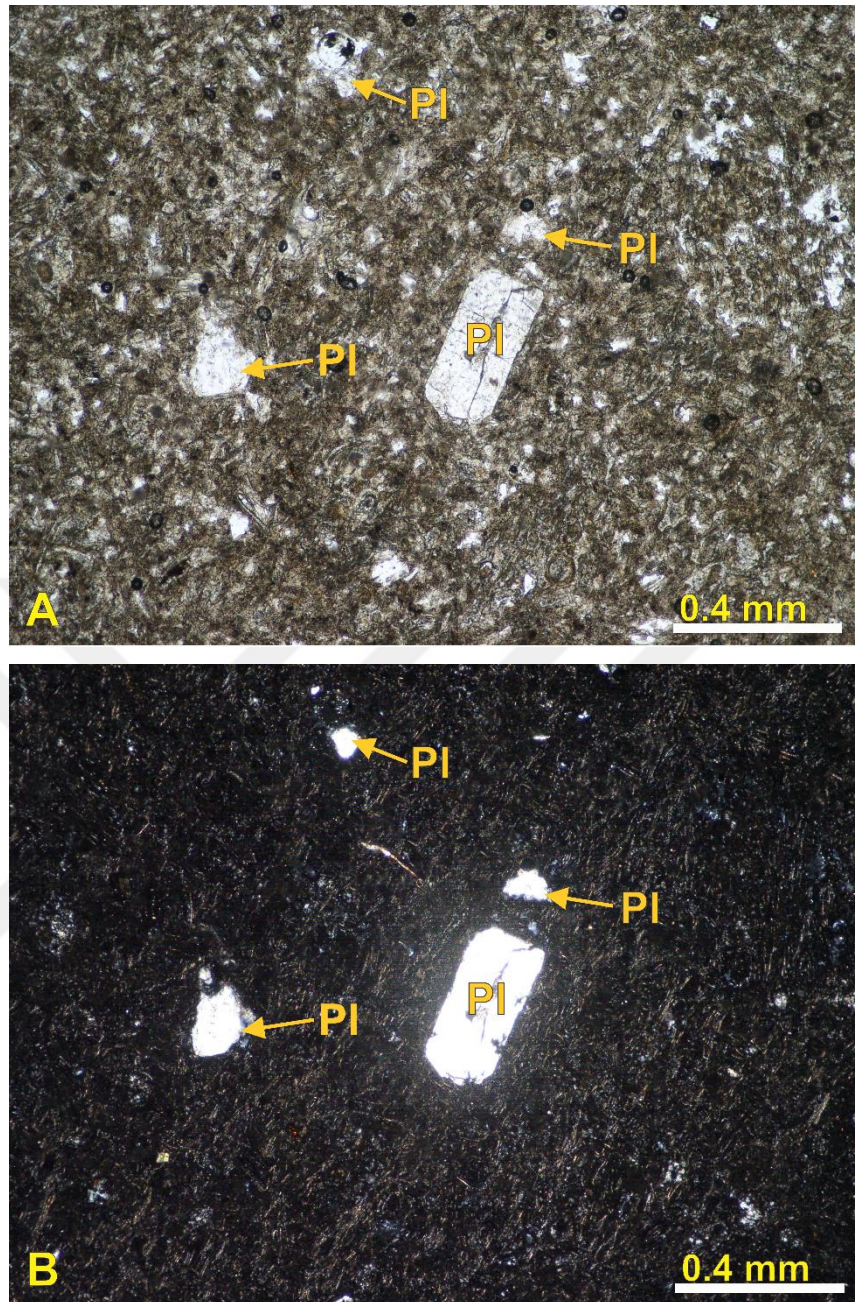
Figure 3.11 S1 (HW vitric tuff)-Observations under Plane Polarised light (A) and Cross Polarised Light (B) (Pl-Plagioclase feldspar, F-Feldspar, Px-Pyroxene, Bt-Biotite, Rf-Rock fragment, S-Sanidine, Qtz-Quartz, Ch-Chalcedony formed from devitrified glass, Pm-Pumice)
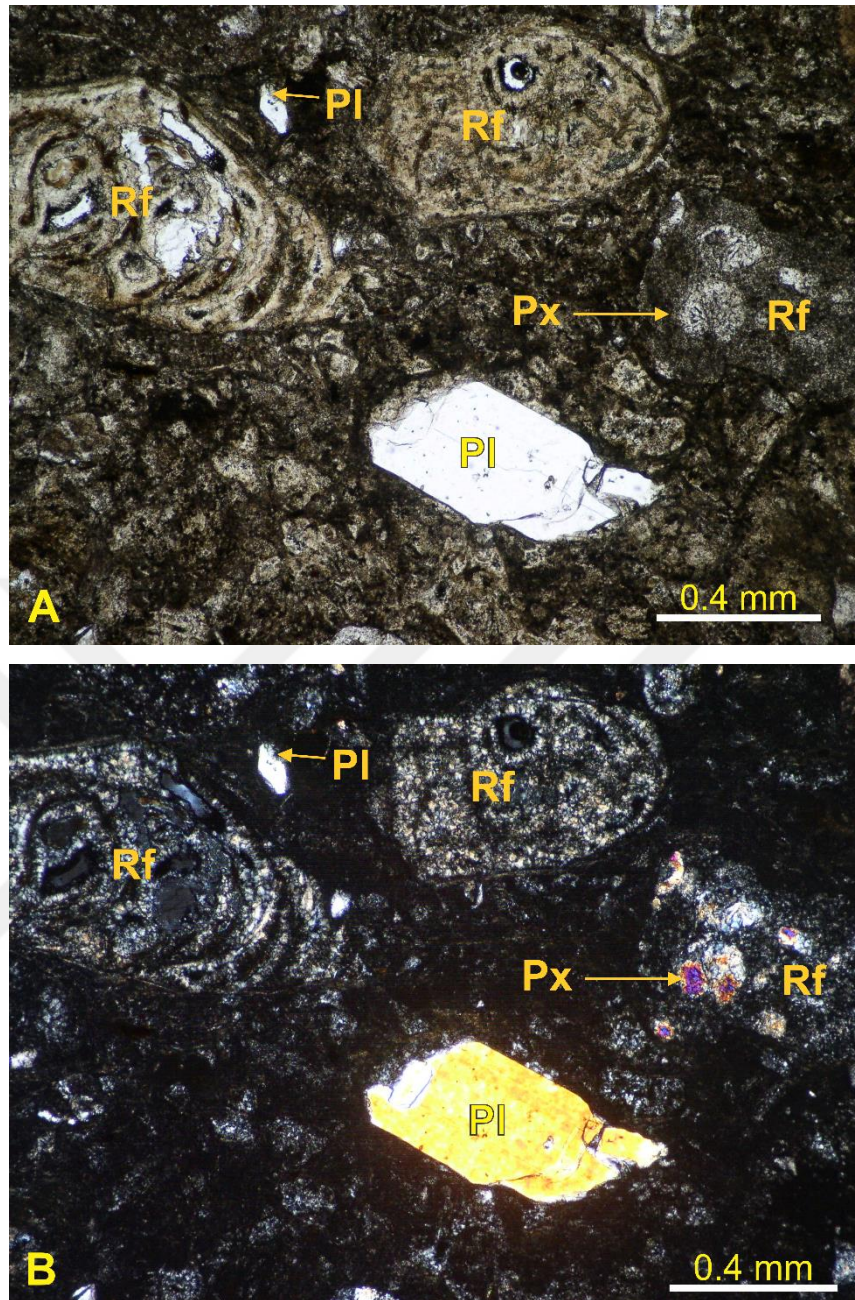
Figure 3.12 S2 (SW lithic tuff)-Observations under Plane Polarised light (A) and Cross Polarised Light (B) (Pl-Plagioclase feldspar, F-Feldspar, Px-Pyroxene, Bt-Biotite, Rf-Rock fragment, S-Sanidine, Qtz-Quartz, Ch-Chalcedony formed from devitrified glass, Pm-Pumice)
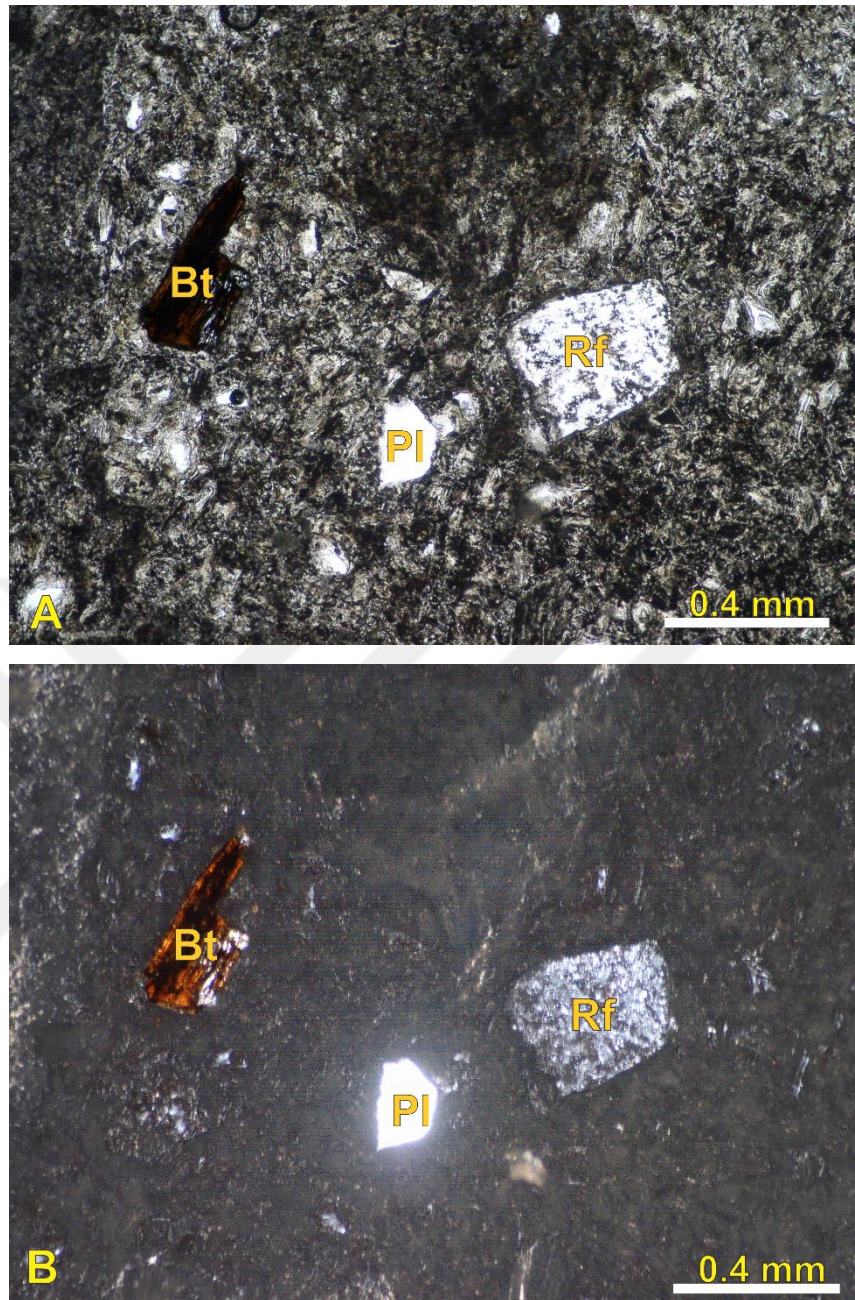
Figure 3.13 S3 (HW vitric tuff)-Observations under Plane Polarised light (A) and Cross Polarised Light (B) (Pl-Plagioclase feldspar, F-Feldspar, Px-Pyroxene, Bt-Biotite, Rf-Rock fragment, S-Sanidine, Qtz-Quartz, Ch-Chalcedony formed from devitrified glass, Pm-Pumice)

3.2 Geochemical Studies

3.2.1 Whole Rock Chemical Analysis

Whole rock geochemical analysis was conducted on rock samples obtained from the field. Samples were chosen from each of the ten slopes (sample groups). These rocks were prepared by crushing and grinding into fine powder. An Atomic Absorption Spectrophotometer (AAS) was used for the analysis. The analysis was conducted for nine (9) major elements in their oxide form: K_2O, Na_2O, SiO_2, Al_2O_3, MnO, TiO_2, FeO, CaO, MgO. The results of these analyses are presented in Table 3.2 and Table 3.3. The rocks were classified as andesitic tuffs (S1, S2 and S3), rhyolitic tuffs (SA, SB, SC, SD, SE and SF) and rhyolite based on the percentage of silica they contain.

Table 3.2 Chemical composition of S1, S2 and S3 (Andesitic Tuff)

Sample→ Element ↓	S1	S2	S3
SiO_2	54.023	53.370	54.030
Al_2O_3	16.575	17.044	17.065
$\sum Fe_2O_3$	5.708	6.833	6.626
MgO	1.546	1.032	1.714
CaO	3.442	3.158	3.657
Na_2O	3.547	4.489	4.680
K_2O	5.740	3.756	4.087
MnO	0.025	0.016	0.017
TiO_2	0.395	0.637	0.185
Loss on Ignition	8.11	8.87	8.06
Total	99.111	99.205	100.121

Table 3.3 Chemical composition of SA, SB, SC, SD, SE, SF (Rhyolitic tuff) and SG (Rhyolite)

Sample → Element ↓	SA	SB	SC	SD	SE	SF	SG
SiO_2	66.751	72.359	77.941	73.248	73.124	73.459	77.878
Al_2O_3	11.243	10.201	9.554	9.064	9.914	9.605	8.975
$\sum Fe_2O_3$	1.022	0.782	0.711	0.703	0.484	2.094	2.942
MgO	0.179	0.412	0.056	0.106	0.121	0.861	0.283
CaO	4.49	1.148	0.881	1.504	1.298	1.014	0.263
Na_2O	1.587	1.54	2.283	1.969	1.581	1.617	2.24
K_2O	2.082	3.876	4.394	3.568	2.865	4.033	4.197
MnO	0.004	0.012	0.014	0.011	0.014	0.065	0.058
TiO_2	0.002	0.003	0.006	0.004	0.008	0.006	0.007
Loss on Ignition	12.661	9.673	4.277	9.898	10.583	7.235	3.607
Total	100.02	100.01	100.12	100.08	99.99	99.99	100.45

3.2.2 X-Ray Diffractometer (XRD) Analysis

Infill materials (clay samples) were obtained from discontinuities of the ten slopes (sample groups) along the Bağarası-Foça (Izmir) State Highway. X-Ray Diffractometer (XRD) analyses were conducted on the clay samples obtained from the field. Separate XRD analyses were conducted for each of the ten slopes. The dominant mineral identified from the XRD analyses was smectite, a clay mineral with a high swell potential. Very high quantities of smectite were found in all the samples.

As high as 8000 counts of smectitie was recorded in SF and SG. Other minerals identified from the XRD analyses were zeolite, mica, chlorite, kaolinite, K-feldspar, plagioclase, amphibole, cristobalite and quartz. X-Ray diffraction diagrams of the ten slopes are presented in Figure 3.14, 3.15, 3.16 and 3.17.
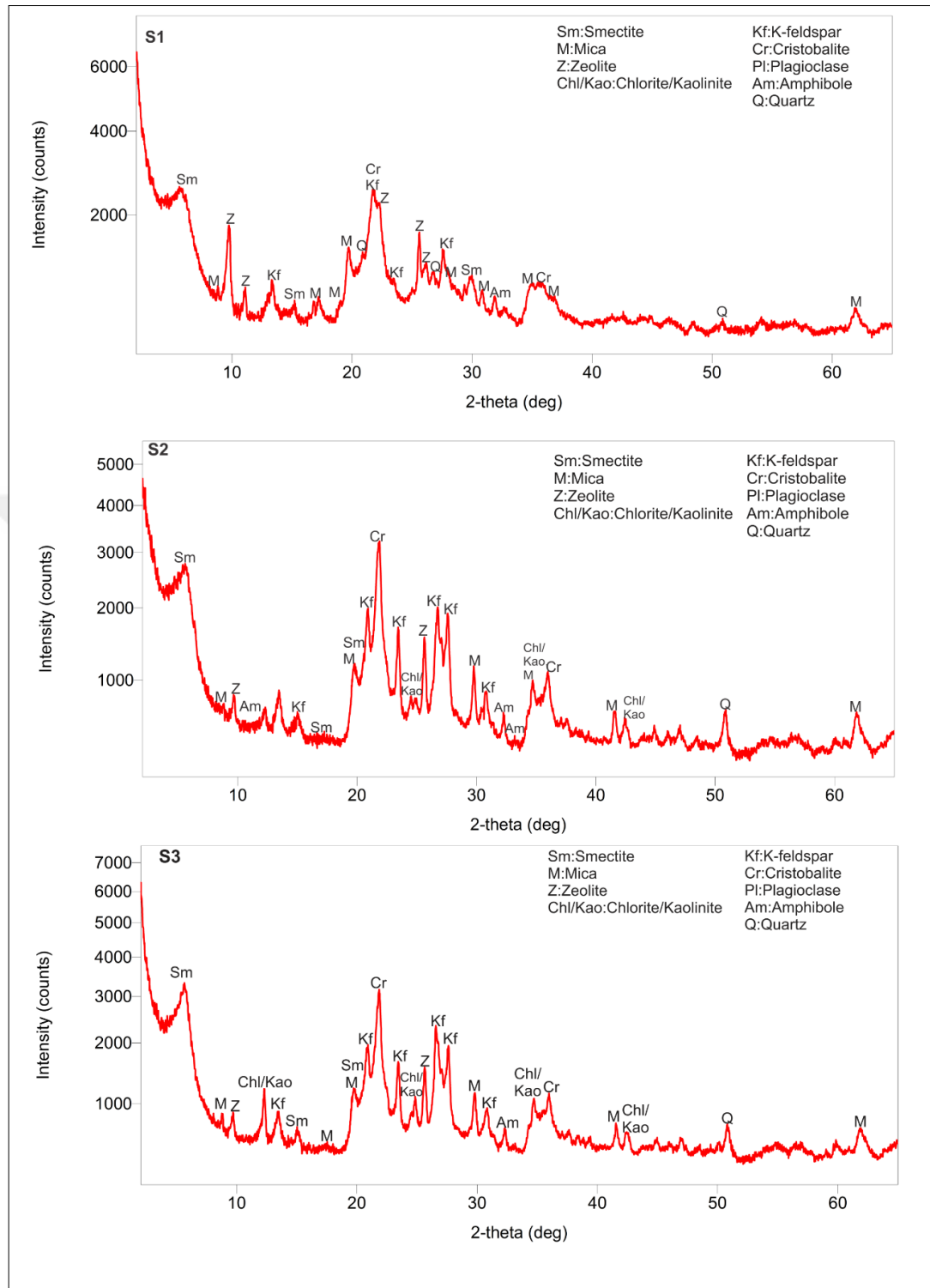
Figure 3.14 X-Ray diffraction diagrams of S1, S2 and S3
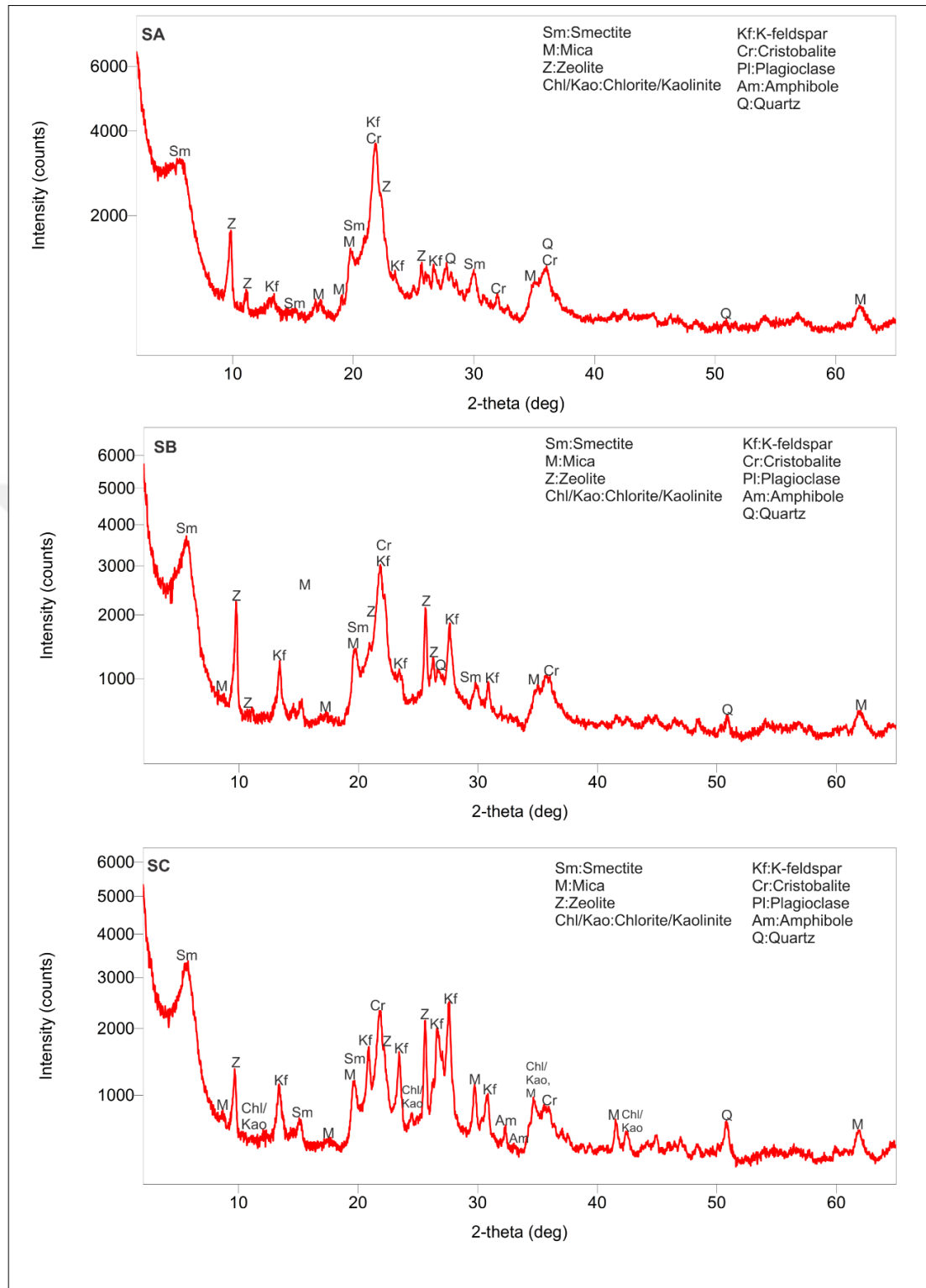
Figure 3.15 X-Ray diffraction diagrams of SA, SB and SC
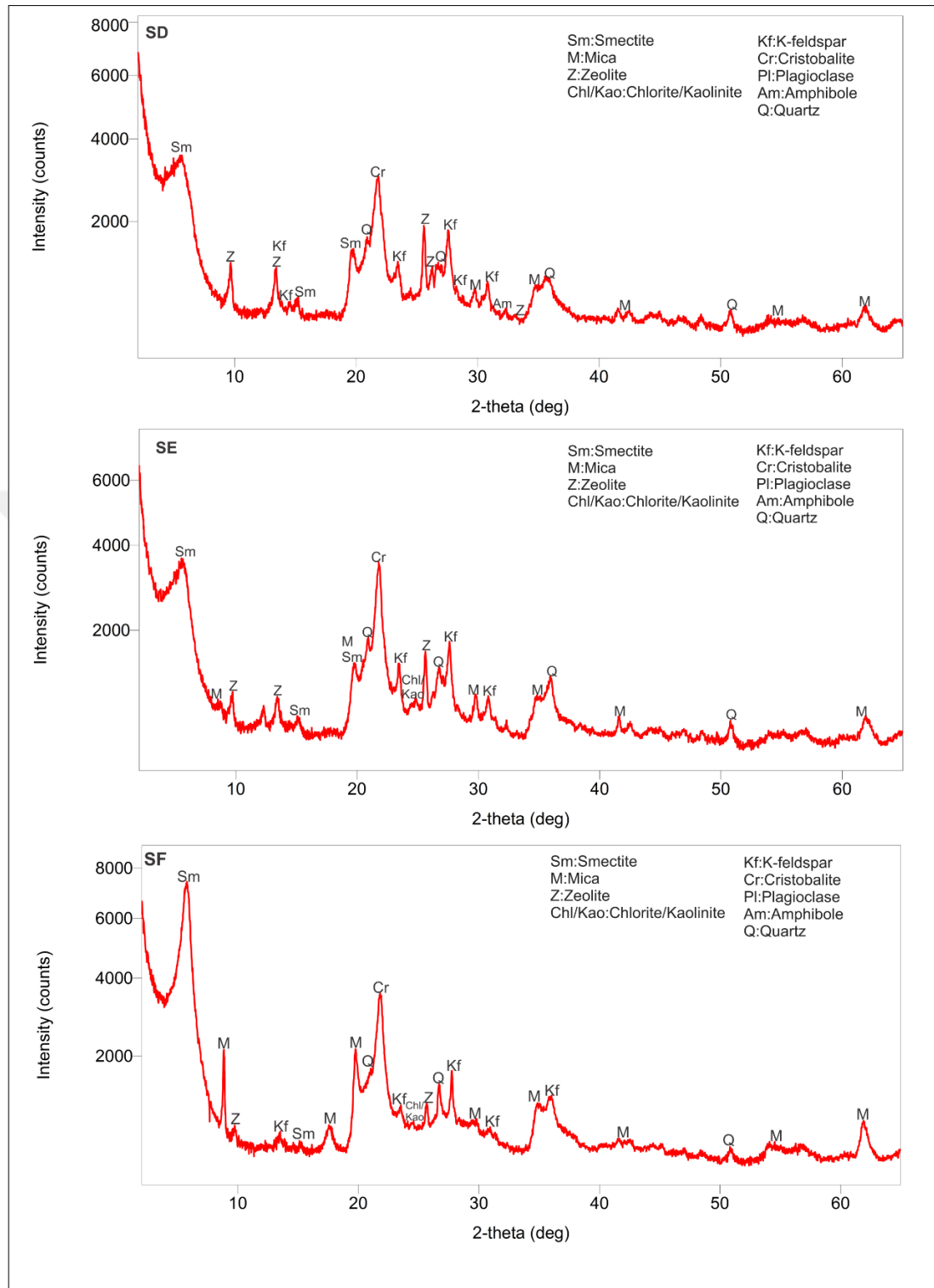
Figure 3.16 X-Ray diffraction diagrams of SD, SE and SF
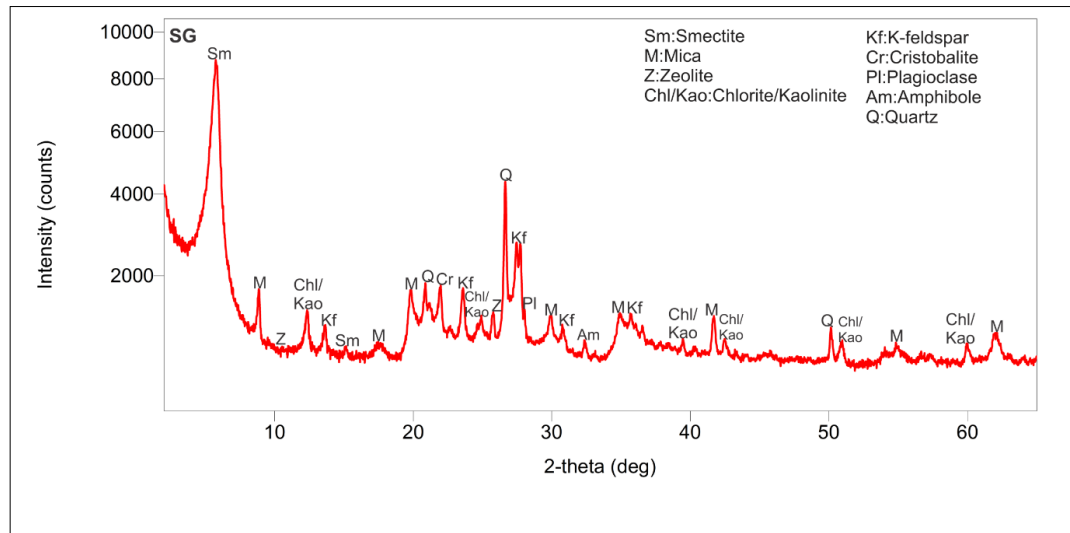
Figure 3.17 X-Ray diffraction diagrams of SG

CHAPTER FOUR
ENGINEERING GEOLOGY

4.1 Introduction

This chapter presents the literature review, laboratory test results, field works and software analyses (Dips 5.1 and Phase^2 by Rocscience), which were employed to determine the engineering geology of the Bagarasi-Foca (Izmir) State Highway.

Laboratory tests conducted to determine the physico-mechanical properties of the rock materials include unit weight and porosity tests, p-wave velocity tests (saturated and dry),uniaxial compressive strength tests (saturated and dry), point load index tests (dry), Brazilian indirect tensile strength tests, slake durability index tests (Id$_5$-5 cycles), shear box test and triaxial compressive strength tests.

Field works conducted include lithological mapping, sample collection and discontinuity data collection (scanline mapping of discontinuities). Kinematic analysis was done using Dips 5.1 software while Phase^2 software was used to determine the Strength Reduction Factor (SRF) of the slopes.

4.2 Literature Review

Rock slopes are important in engineering. Investigation of rock slope stability is therefore an important component of engineering projects such as mining pit slopes, highways, dams and building projects (Wyllie & Mah, 2004; Hoek *et al*., 2000). Ulusay (2013) commented on the importance of engineering geology in rock slope stability assessment in the book "Rock Characterisation, Modelling and Engineering Methods".

The author stated that engineering geological considerations are necessary in the design, construction and monitoring of rock slopes. Five important factors which form the foundation of rock slope assessment were identified by the author.

These factors are lithology, structure, state of deterioration, hydrogeological conditions prevailing in rock slopes and correct selection of rock mass geomechanical parameters. One other important factor which was identified is external forces, such as dynamic loading due to earthquakes for slopes found at earthquake-prone regions.

4.2.1 Previous Studies in the Study Area

Koca & Kincal (2004) conducted a research on "Abandoned Stone Quarries in and around the Izmir City and Their Geo-Environmental Impacts". These quarries (originally at the outskirts of Izmir) were used in the past for obtaining building/construction materials but became a source of danger to people as a result of the rapid expansion of the city.

Scanline mapping was done and the data obtained were used to prepare discontinuity maps of the study area. Stereographic projections were used to analyze discontinuity data obtained from the field. Shear tests were also carried out to determine the shear strength parameters of the rocks in the study area. Weathering maps were prepared and the rocks were classified based on their weathering grades.

Key findings from this research include the following:

a. Mass movements which have developed in the abandoned quarries could damage the buildings in the vicinity unless the stability of the quarry slopes is improved.
b. Different modes of failure (such as planar, toppling and wedge failure) were identified. It was therefore recommended that building in the area or using it as a damping site should not be permitted.
c. Slopes of andesite quarries were observed to be more prone to failure compared to those of limestone, dacite and flysch. The reason given for this is that the limestone beds and joint surfaces have a high surface friction angle as well as closed and calcite filled discontinuities which give them greater stability.

Demirbasa (2005) conducted research on the engineering properties of volcanic tuffs in Çeşme (Izmir). The author noted that volcanic tuffs, when exposed and subjected to surface conditions coupled with the presence of water, rapidly undergo weathering. Consequently, this inherent weakness of the tuffs negatively affects their engineering (physico-mechanical) properties. Volcanic rocks observed in the study area include tuff, tuffite, agglomerates, andesite and basalt. Microscopic studies were conducted on thin sections of tuffs from the study area. Minerals identified include: quartz, biotite, calcite, plagioclase, hornblende, pumice and quartzite.

X-ray diffraction studies were also conducted on the tuffs. Minerals identified from this study include: calcite, K-feldspar, quartz, plagioclase, smectite, dolomite and illite. Geochemical studies, as well, were conducted on the tuffs to determine the chemical properties of the different weathering grades. It was observed that as degree of weathering increases, the rates of chemical weathering index and Parker index increase. An important finding from this work is that as the speed of P-waves increase, natural unit weight increases and porosity decreases.

Muti (2009) conducted research on "Engineering Geology of the Foça (Izmir) Tuff". It was noted that volcanic tuffs are widely prevalent in the western part of Turkey. The author observed that many engineering structures have been built on the volcanic tuffs in Izmir. Minerals identified from petrographic and X-ray diffraction studies include: quartz in matrix, calcite, plagioclase and biotite.

Uniaxial Compressive Strength (UCS) tests were also conducted on nineteen tuff samples obtained from the field. The weathering degrees of the samples were noted prior to crushing. It was observed that the highly weathered samples had the weakest strength while the slightly weathered rocks had the greatest strength. Based on this, it was concluded that as degree of weathering increases, rock strength (UCS) reduces. The tuffs were generally classified as having strength of hard soil-weak rock.

The relations between the tuffs and their physico-mechanical properties was determined as follows: a) as degree of weathering of the tuffs increases, values of porosity and void ratio decrease and natural unit weight increases and b) as degree of weathering increases, the P-wave values decrease.

Kincal et al (2009) conducted a landslide susceptibility assessment in Izmir and its surroundings using logistic regression method. A significant percentage of the total landslide area was covered by weathered volcanic rocks and a key observation was that major landslides largely occurred in these areas. Independent variables used in the study were slope angle, lithology and distance to drainage. The presence or absence of landslides, on the other hand, was chosen as the dependent variable.

The study revealed that landslides in the area tend to occur in weak rocks (shale, limestone), weathered volcanic rocks and laminated marls as well as in clayey levels of the Neogene sedimentary rocks. Factors identified as triggers of landslide in the area include heavy rainfall and seismic activity. Landslide susceptibility maps were produced to serve as a reliable guide to relevant stakeholders in managing landslide hazards in the area.

Kincal (2014) conducted a research on slope stability in the Alipaşa Albite Mine (in the Menderes Massif-Turkey) using two new stereographic projection techniques. These techniques are: Overlay Linear-Element Process (OLEP), and Crack Pattern Analysis (CPA).OLEP is based on the comparison of the kinematic analysis with the detected slope movements. Foliation planes constituted an essential component of slope stability analysis in this study. It is noteworthy that surface friction angle of the sliding surface was not taken into consideration.

CPA on the other hand, is based on the relationship between the discontinuities and tension cracks developed on the catch benches. The author noted that the main lithology in the study area was ortho-gneiss and the main discontinuities observed in this formation were tectonic joints and foliation planes.

It was stated that the opened joints served as conduits of water and as a result of the high rate of infiltration of water through these conduits significant degrees of weathering occurred in certain areas of the slope. Being situated in a high risk earthquake zone, the slopes in the area were observed to have the possibility of failing as a result of earthquakes.

An interesting observation in the study is that only plane failures were detected and sliding occurred along the foliation planes. Key findings in the study include the following:

a. OLEP and CPA were successfully used in determining which discontinuity sets formed the tension cracks and to measure the angles formed by the intersecting tension cracks.

b. OLEP and CPA are suitable for both planar failure and wedge failure analysis. In planar failure analysis, ground movement directions are used as linear elements while in wedge failure analysis, the joints forming the wedge are used as linear elements.

c. By using OLEP and CPA the relationship between tension cracks on an upper slope face and discontinuities in deep rock slopes can be safely determined.

4.2.2 General Overview of Slope Failures

Kliche & Charles (1999) in their book "Rock slope Stability" defined slope stability as the resistance of inclined surfaces to failure by sliding or collapsing. The author sidentified four basic modes of failure in their work. These are:

a. Planar failure
b. Rotational failure
c. Wedge failure and
d. Toppling failure

On the above modes of failure, the Kliche (1999) note that:

a. Planar failure occurs when the strike of the plane on which sliding occurs is within ±20° of the strike of the slope. Also, the failure plane must dip at an angle lesser than that of the slope face, and the internal angle of friction for the discontinuity must be less than the dip of the discontinuity (Hoek and Bray 1981).

b. Rotational failures generally occur in weak rock slopes and do not always occur along circular arcs.

c. Wedge failure occurs in rock masses with two or more sets of discontinuities whose line of intersection is approximately perpendicular to the strike of the slope and dips toward the plane of the slope.

d. Toppling failures occur as a result of the overturning of columns of rock layers, formed by steeply dipping discontinuities in a rock mass.

4.2.3 Factors That Cause Slope Failure

Varnes (1978) put the factors that cause slope failures into two major groups. These are:

a. factors that contribute to increased shear stress (examples include: removal of lateral support, transitory earth stresses and the addition of surcharge to the load).

b. factors that contribute to reduced shear strength (examples include: Changes in shear strength caused by weathering as well as other physical and chemical reactions and factors originating from the inherent properties of the material).

4.2.4 Slope Stability Analyses

Many methods have been developed and used over the years for slope stability analyses. These include limit equilibrium technique, back analysis, finite element and finite difference, the "key block" concept and stochastic medium theory and probabilistic methods.

However, the limit equilibrium method (based on equating the driving or shearing forces due to water and gravity to the resisting forces due to cohesion and friction) is the most widely used method (Piteau and Martin, 1982).

In the wake of advancements in science and technology, a number of computer software have been developed and are currently in use in slope stability analysis. Examples of such software are Phase^2, Slide and Dips by Rocscience. In carrying out a successful slope stability analysis, Abramson et al. (2002) note that, an in-depth knowledge and comprehension of the geology of the area is required.

Some of the geological features which were identified by the researchers as having the potential to affect the stability of a slope are:

a. Fabric of slope material (example: mineral types)
b. Discontinuities and bedding planes
c. Orientation and stratification of minerals
d. Geological anomalies (example: previously sheared zones)
e. Weathering degree
f. Groundwater
g. In situ stresses
h. History of previous landslides

4.2.5 Socioeconomic Consequences of Slope Failure

The consequences of slope failures vary widely. They could result in blocking roads/highways, destruction of engineering structures and even burial of cities (Hunt, 2005). In mines, slope failures could lead to production loss and potential ore reserve losses. Urbanized areas stand to suffer greater consequences from slope failures because even small slides can damage buildings and block access to traffic (Transportation Research Board, 1996).

4.2.6 Slope Stabilization Methods

Many methods are currently in use in stabilizing rock/soil slopes. Some of these methods include benching, rock bolting, wire meshes, dewatering and vegetation cover. Slope stabilization methods can be put into five major groups. These are making modifications to the geometry of the slope to reduce the driving forces or increase the resisting forces, controlling infiltration of surface water to minimize seepage forces, controlling internal seepage to minimize the driving forces and increase the strengths of materials, providing lateral support to increase the resisting forces and increasing soil/rock strength with injections (Hunt, 2007).

4.2.7 Review of Research on Slope Stability

4.2.7.1 Deterministic Method based Research

Kentli and Topal (2004) assessed the stability of ten (10) cut rock slopes along the Ankara-Pozanti motorway in Turkey. Detailed field studies and mapping were conducted. The dominant lithologies mapped were microgabbro, limestone and dolomite –limestone. The earthquake history of the area was researched and a suitable Peak Ground Acceleration (PGA) value (0.2 g-0.3 g) was chosen. Laboratory tests were conducted to determine the physico-mechanical properties of the intact rock. Dips 5.0 and Swedge 3.0 software by Rocscience were used for kinematic and limit equilibrium analyses respectively.

Generally, high Factor of Safety values were obtained from the analyses. A slight modification of the slopes was recommended by the authors to ensure safety. The excavatability of the rocks was also assessed in the study. Based on the assessment, blasting was recommended for areas with widely spaced discontinuities where ripping may not be feasible.

Khanlari and Mohammadi (2005) assessed the instability of slopes in heavily jointed limestone rock in an Australian quarry. Field studies (scan line mapping) were done and various laboratory tests were conducted on rock samples obtained from the field to determine the physico-mechanical properties of the rock material. Kinematic analysis was conducted on discontinuity orientation data, which was plotted on stereonets. The possibility of different modes of failure such as planar and wedge failure occurring was successfully evaluated using kinematic analysis.

Panthi and Nilsen (2006) conducted research on numerical analysis of stresses and displacements for a rockslide in Norway using Phase ^{2} software. Input data for the analysis was obtained from laboratory testing of rock specimens. Hoek-Brown failure criterion was used for the analysis. Stresses acting on the slope before and after the slide as well as the future behavior of the slope were successfully analyzed and evaluated using Phase^2 software from Rocscience.

Oztekin et al. (2006) assessed the degradation and stability of a highway cut slope in Ankara, Turkey. The main rock type in the study was limestone. DIPS, Roclab and Slide software by Rocscience as well as GIS tools were employed in the study. Discontinuity data from scanline mapping was represented on a stereograph using DIPS. Roclab was used to calculate shear strength parameters of the rocks while Slide software was used to model the slope and calculate Factor of Safety. GIS tools were used to estimate the possibility of failure recurring in areas which have experienced failure previously.

Zhang et al. (2010) conducted research on 'Engineering geology and stability of the Jishixia landslide, Yellow River, China'. Limiting equilibrium methods were employed in the study to determine the prevailing stability state of the landslide. Two slip surfaces were identified with the main slip surface at the contact of two lithologies: i) medium-grained sandstone intercalated with siltstone and conglomerate and ii) conglomerate intercalated with thin medium-grained sandstone.

In order to predict the future potential stability of the landslide, a pick ground acceleration of 0.11g was assigned based on past earthquake history. The landslide was found to be subject to atmospheric moisture and variations in groundwater level. Construction of retaining walls were recommended in order to prevent casualties in the event of failure.

Futalan et al. (2010) assessed potential failure sites at Mount Can-abag (Phillipines). The dominant lithology in the study area were sandstones and mudstones. The mudstones were identified as having the highest risk of failure. Schmidt hammer test results indicated that the mudstones generally had low uniaxial compressive strength. The low permeability of the mudstones was also reported to be a cause for concern due to its water storage potential which could increase pore water pressure. Another factor observed in the study as contributing to the instability of the slope was clay infills. The infills in the apertures of the discontinuities prevented the free flow of water out of the slope thereby increasing the risk of instability.

Yilmaz et al. (2012) conducted research on GIS-based kinematic slope instability and Slope Mass Rating (SMR) maps using a railway route in Turkey as a case study. Various discontinuity orientation measurements were taken in the field and the data was input into ArcGIS software. Analysis was then conducted for plane and wedge failures. The results showed that planar and wedge failure was likely to occur at some sections of the route. Slope Mass Rating was used to classify the slopes. The authors noted that the SMR results agreed with and validated the results of the kinematic analysis.

Irigaray et al. (2012) suggested a method of slope stability analysis that combined GIS technology and probabilistic analysis. Field studies included scanline mapping as well as tilt test for determining friction angle. Technological tools employed in the study were DIPS 5.0, ArcGIS 9.3, RocPlane 2.0 and Swedge 5.0.

Kinematic analysis was done with the aid of DIPS 5.0 and ArcGIS 9.3 software while Factor of Safety and Probability of Failure were calculated using RocPlane 2.0 and Swedge 5.0 software. A high degree of accuracy was found (90% of the slopes) when the results of the analyses were compared to field observations. The authors therefore recommended the method they used as suitable for initial assessment of rock slope stability.

Kaşmer et al. (2013) assessed the stability of natural slopes and man-made caves in Cappadocia, Turkey. The authors stated that the dominant lithology in the study is volcanic tuff. Petrographic and X-ray studies as well as physico-mechanical laboratory tests were conducted on rock specimens obtained from the field. Petrographic studies gave the composition of the rock as plagioclase feldspar, biotite, lithic fragments and pumice. Minerals identified from X-ray diffraction analyses were quartz, feldspar, mica and clay minerals (smectite).

Physico-mechanical property tests on the volcanic tuff showed that they had a weak strength with significant strength reduction when saturated. Phase^2 software was used for numerical modelling of the slopes. The main factor of concern in the modelling was toe erosion. Mohr-Coulomb failure criterion was used for the analysis.

Results from the analysis indicated that the tuffs were liable to different types of rock failure such as plane, toppling and rock falls. Erosion at the toe of the slopes was found to be a significant factor in the stability of the slopes.

Singh et al. (2014) evaluated the stability of road-cut slopes in Himalaya, India. Both limit equilibrium and finite element (numerical analysis) methods were used in the study. The authors noted that Himalaya is hilly and prone to landslides. Factors identified as triggers of landslide in the region include earthquakes, high rainfall as well as road widening and construction of structures such as dams, tunnels and bridges. Series of discontinuity orientation measurements were taken in the field and various laboratory tests were run on specimens prepared from field samples. Slide and Plaxis software were used for the limit equilibrium and finite element analysis respectively.

The difference in the factor of safety values obtained using the two methods was small with an average difference in value of 0.16. Some of the slopes were found to be at risk and rock bolts were recommended.

Hosseinitoudeshki (2014) analyzed the stability of rock slopes along a road in Iran. The slopes were made up of two lithologies; andesitic tuff and porphyrites. Separate stability analyses were conducted for each of the two lithologies using Phase ^{2} software. Shear strength reduction analysis was done using both Hoek-Brown and Mohr-Coulomb criteria. Input data for the analyses was derived from field tests and laboratory tests on borehole samples. The andesitic tuffs had an average Uniaxial Compressive Strength (UCS) value of 83 MPa while the porphyrites had an average UCS of 112 MPa.

Roclab software by Rocscience was used to calculate the shear strength parameters and other rock mass property values which were necessary for the stability analysis. The author noted that in each case, analyses conducted based on Hoek-Brown criterion produced better results compared to that of Mohr-Coulomb criterion. Results of the analyses showed that the slopes were not likely to undergo rotational failure. Hoek-brown criterion was recommended by the author to be used for analyses when dealing with rocks in the study area.

Ghosh et al. (2014) analyzed the stability of a failing rock slope in Sikkim Himalayas, India. The slopes were described in the study as vulnerable because of their high and steeply dipping nature coupled with their susceptibility to earthquakes. The lithologies were adequately mapped and slopes were classified using Slope Mass Rating after Romana (1985).

Kinematic analysis was conducted to identify the modes of failure that could occur. The authors recommended construction of a tunnel as a mitigation measure against the frequent slope failures in the study area since all other measures were either not suitable or cost effective.

Kaya et al. (2016) conducted slope stability analysis on a highway tunnel route in the black sea region (Turkey) using three analytical techniques: kinematic, limit equilibrium and numerical analytical techniques. Phase^2 (a numerical modelling software by Rocscience) was used for the numerical analysis. The areas identified in the study as most problematic were covered by volcanic tuffs. Kinematic analysis was used in identifying potential modes of failure and limit equilibrium analysis proved useful in determining whether or not the identified failure modes were likely to occur. Results from the numerical analysis showed that circular failure was likely to occur on the slope. Phase^2 software was used to model a more stable slope.

Qi et al. (2016) assessed the stability of a complex rock slope at Xiari, China. The authors noted that the stability of rock slopes at Xiari was a cause for concern because the rock masses were of poor quality with unfavorable discontinuity orientations. The topography was described as complex with a high tendency to deform. The region was regarded by the authors as important because of its potential for hydropower generation.

The rock mass structure and quality were studied with the aid of boreholes and exploratory adits. Various discontinuity orientation measurements were taken across the slope face and this data was represented on stereoplots. The stability of the slope was analyzed using kinematic, limit equilibrium and numerical analytical methods. Kinematic analysis was used to determine the various modes of failure that could occur; limit equilibrium method was used to calculate the factor of safety of the slope; detailed analysis of the behavior of the slope was done using numerical methods. One important finding from this work was that the volume of blocks which could be displaced in the event of failure was large enough to cause a tsunami.

Schmidt et al. (2016) conducted studies on the use of Phase^2 (a finite element analysis software by RocScience) in conducting slope stability analysis. The generalized Hoek-Brown failure criterion was used in the study. The authors noted that Phase^2 is useful in analyzing stresses and in calculating factor of safety. The stability of two slopes were analyzed in the study using Phase^2.

The factor of safety values obtained from the two analyses were compared to the actual stability state of the slopes for validation. The factor of safety values obtained were found to accurately represent the actual stability state of the slopes observed in the field. The software was therefore considered reliable and useful in analyzing the stability of slopes.

4.2.7.2 Probabilistic Method based Research

Shaban et al. (2001) conducted research on the instability of a road slope in Lebanon. Reasons they found for the unstable nature of the rock slopes include weak lithologies, undulating topography and the steepness of the slopes. Structures such as faults were also found to be contributing factors to the instability of the slopes.

Field studies, aerial photographs and Global Information System (GIS) tools were employed in the study. Hazard assessment maps were generated which indicate the level of risk of various sections of the slope. It was recommended that high risk zones should be given adequate attention.

Park et al. (2005) conducted research on the use of probabilistic analysis in rock slope stability assessment. A western North Carolina (USA) highway was used as a case study. The authors identified some limitations of deterministic methods of slope stability analysis (one of which is not accounting for variations in rock mass properties and conditions) and noted that probabilistic analysis provides solutions to such limitations. The dominant lithology mapped in the study area was siltstone.

Both deterministic and probabilistic slope stability analyses were done and the results were compared to each other. A significant difference was reported by the authors in one of the joint sets analyzed. Whereas the deterministic analysis indicated that the slope was stable and safe, the probabilistic analysis showed that the slope had a 34% likelihood of failure. The reason stated for this was that even though there was no daylighting, variations in joint orientations made the slope with this particular joint set susceptible to failure.

Pantelidis (2011) reviewed highway slope instability risk assessment systems. The author identified significant weaknesses in both quantitative and qualitative landslide risk analysis methods in use. Weaknesses identified in the quantitative methods include not giving considerations to: i) geological structures and slope conditions, ii) oversimplification of traffic and landslide assumptions, and iii) socio-economic consequences. Weaknesses identified in the qualitative methods include considering: i) high rock slopes as safe even though rockfalls could be tragic, and ii) wide roads as safe despite the fact that the presence of a fallen rock on the road poses danger to traffic and could result in loss of lives.

Li and Xu (2016) conducted research on application of Slope Stability Probability Classification (SSPC) in rock slope stability assessment. The authors mentioned that SSPC by Hack (2002) is based on two analyses methods: orientation dependent and orientation independent stability analyses. Slope stability assessment was conducted on ten (10) excavation rock slopes using SSPC and an accuracy of 70% was found indicating the reliability of the method.

Canal & Akin (2016) assessed the stability of a state highway cut slope in Adilcevaz-Bitlis (Turkey). Slope Stability Probability Classification (SSPC) method was used in the study. The authors noted that SSPC by Hack (1998) is based on three parameters. These are i) Exposure Rock Mass ii) Reference Rock Mass and iii) Slope Rock Mass. It was mentioned in the study that factor of safety values obtained from deterministic analyses may not always be a true reflection of the actual stability state of a slope due to variations in geotechnical properties of a rock mass on a regional scale.

Discontinuity property data was obtained from scanline mapping at seven (7) distinct sections of the rock slopes along the highway. The rock slope was cut in limestone. Point load tests were done in the field to estimate the uniaxial compressive strength of the intact rock. The authors noted that the slopes were prone to different modes of failure.

Steeply dipping discontinuities at some sections of the slope were reported to stand the risk of toppling failure or rock falls. Generally, no infills were observed in the discontinuities. Rebound values of 27-44 were obtained from Schmidt hammer tests conducted in the field.

Roclab software was used to calculate the shear strength parameters of the rock mass. DIPS 5.0 was used to conduct kinematic analysis on the discontinuity data. SSPC was then conducted. Results from the SSPC analysis showed that whereas the probability of toppling failure was low for some sections of the slope, it was as high as 80-90% for other sections.

High probability of planar failure was also found for certain parts of the slope. Slide software was used in the study to conduct limit equilibrium analysis for circular failure. The results of this analysis indicated that circular failure was not likely to occur.

4.2.8 Effect of Clay minerals and Weathering on Slope Stability

Hatzor and Levin (1997) conducted a research on 'the shear strength of clay-filled bedding planes in a phosphate mine by back analyzing a slope failure'. The major lithology in the study area was phosphatic limestones. No groundwater seepage or seismic activity was noted prior to the failure of the slope. For this reason, the authors noted that the failure must have occurred under static load. The clay (infill material) had a thickness between 2 and 5cm and was classified as being of high plasticity.

X-ray diffraction studies showed that the clay (infill material) was predominantly made up of montmorillonite (smectite group). Sliding failure was found to have occurred along the clay-filled bedding plane. Results from consolidated direct shear test conducted on the infill material showed that it had a very high shear strength. Further studies revealed that the failure did not occur within the clay (infill material) itself but rather at the contact between the clay and the limestone.

Baron et al. (2004) conducted a research on some 'deep-seated slope failures in Czech Republic'. The study was conducted on three different failures which occurred in flysch-type of lithology. X-ray diffraction analysis conducted on the clay in the weathered zones of the slope revealed that the clay contained expansive minerals such as smectite; other minerals include: quartz, feldspar, mica and kaolinite. Geomorphic mapping and 2D subsurface imaging were done and all important details of the failure were noted. One of the factors which was identified in the study as causing the failure of the slopes was the swelling pressures of the expansive clay minerals.

Shuib et al. (2006) conducted a study on 'discontinuity controlled cut-slope failures' along a highway in Malaysia. Many rock units were mapped in the study area. Some of these were: shale-sandstone, tuff, phyllite, schist and granite. Infillings were observed in the mapped discontinuities and it was reported in the study that the infillings had the same mineralogy as that of the weathered rock.

Some of the joints were clay filled. A landslide was observed at a section of the slope which was covered by weathered foliated shales with clay filled joints. Kinematic analysis conducted on the landslide indicated that the slope failed as a result of poor discontinuity orientations. In addition, field observations showed that the clay-filled joints played a significant role in the failure of that section of the slope. Other causes of instability which were mentioned in the study were: vibration from moving cars and surface water infiltration.

Maleki (2011) conducted a study on the 'engineering geological problems of the Havasan Dam (Iran) with emphasis on the clay filled joints in the right abutment'. The major lithology in the study area was limestone. Detailed field studies were conducted. Discontinuity orientation data taken from the field was plotted on stereonets using Dips 5.1 software by Rocscience (2002). From the stereo-plot, it was observed that bedding planes were the major discontinuities which controlled the properties of the rock mass. Subsurface investigations were conducted using exploration boreholes. Opened clay filled joints were observed in the abutment; these joints had an average width of 7-9 cm.

Laboratory tests were conducted on samples of the clay infill material. The laboratory results showed a wide variation in the plasticity of the clay infillings. X-ray diffraction studies indicated that the clay was composed of minerals with high swelling potential such as illite and montmorillonite. The authors noted that the clay infillings negatively affected the stability of the slope because the infilling decreased the shear strength of the joints. Kinematic analysis showed that wedge failure could occur on the abutment. The authors concluded that the site was not suitable for dam construction.

Sharma et al. (2012) evaluated the stability of a cut slope along a road in India. The role of clay minerals in the stability of the slope formed an important component of the study. The dominant lithology in the study area were sandstone and shale. The discontinuities mapped were mainly joints and bedding planes. The rock masses were classified using Rock Mass Rating (RMR) proposed by Bieniawski (1973) and Slope Mass Rating (SMR) after Romana (1988). RMR and SMR values of 62 and 56 were obtained, respectively.

X-ray diffraction analyses were conducted on clay minerals (overburden material) to determine their composition. It was observed from the analysis that clay minerals, which were formed from weathered shales in one of the formations studied, contained up to 13.5% montmorillonite. The authors stated that the presence of montmorillonite was the reason why sections of the slope with weathered shales experienced failure frequently.

Regmi et al. (2012) examined the 'effect of rock weathering, clay mineralogy and geological structures in the formation of a large landslide'. The lithologies of the study area include: slates, phyllites, quartzites and dolomite. Detailed field studies and lithological mapping were conducted. X-ray diffraction analysis was conducted on both whole rock and clay minerals obtained from the failure zone. Minerals identified from petrographic and X-ray diffraction analysis on the rock sample include: quartz, feldspar and muscovite. The weathered rocks contained smectite and chlorite.

An important finding from this study was that the clay minerals which formed due to weathering negatively affected the stability of the rock. In addition to reducing the strength of the rock mass, the high swelling potential of the smectite rich clay minerals adversely affected the stability of the rock slope.

Miscevic and Vlastelica (2014) conducted a research on 'the impact of weathering on slope stability in soft rock mass'. The major rock formations in the study area were marl and sandstone. The authors reported that differential weathering resulted in blocks of sandstone being exposed on the slope. The reason given for this was that marl undergoes weathering much faster than sandstone. These exposed blocks later fail when their weights are no longer supported due to the weathering. Minerals identified from X-ray diffraction analysis conducted on marl samples include: calcite, dolomite, quartz and smectite.

The shear strength parameters of the rocks were determined using direct shear tests. The authors observed from the study that water had a great influence on the weathering process. They noted that swelling pressures from smectite minerals disintegrate rocks. The weathering process was simulated in the laboratory using drying and wetting cycles. A key observation was that samples which contained more than 50% clay minerals showed full disintegration at a smaller number of drying-wetting cycle. Significant seepage through joints was observed to cause an increase in the rate of weathering.

Two factors were identified in the study as important when analyzing the stability of the slopes in the study area. These were: i) the degree of weathering that occurs with time, and ii) the depth to which weathering occurs. In order to stabilize the slope, it was recommended that degraded material should be kept on the slope face to facilitate growth of vegetation.

4.3 Laboratory Tests: Physico-Mechanical Properties

Block samples (Figure 4.1) of slightly weathered (SW), moderately weathered (MW) and highly weathered (HW) volcanic tuffs were obtained from ten locations (S1, S2, S3, SA, SB, SC, SD, SE, SF and SG) along the Bagarasi-Foca (Izmir) State Highway. Core specimens were prepared from the block samples in the Rock Mechanics Laboratory (Geological Engineering Department of Dokuz Eylül University). The samples were cut into a length to diameter ratio of 2:1. However, due to the weak nature of the rock samples, core specimen preparation was difficult and some of the specimens could not meet this criterion.

The upper and lower surfaces of the specimens were then smoothened to ensure that each core had faces which were smooth and parallel to each other. This was done to ensure reliable laboratory test results. Cube specimens of dimension 70x70x70 mm were prepared for weak slopes where laboratory coring was not possible.

Figure 4.1 Block sample collection from one of the slopes in the study area

4.3.1 Tests for Porosity and Unit Weight (dry and saturated)

The tests were performed based on ISRM (2007) standards. The length and diameters of each sample was first measured using a Vernier caliper. Next, the specimens were immersed in water for twenty-four hours to get them saturated. They were then removed and after the surfaces were air-dried the saturated-submerged weight of the specimens were determined with the aid of a wire basket.

After this was done, the specimens were weighed in air to determine their saturated weight. They were then oven dried at $110°C$ for twenty four (24) hours and re-weighed to obtain the respective dry weights. A summary of the results obtained is presented in Table 4.1. Detailed Results and Computations for the various properties are presented in Appendix 2.

Table 4.1 Mean unit weight and standard deviation (SD) values of the slopes

Slope Name	Mean (X) dry unit weight (ɣd) (g/cm³)	SD		Mean(X) saturated unit weight (ɣs) (g/cm³)	SD		Mean (X) Effective porosity (n) %	SD	Weathering Degree
S1	1.77	0.03		1.94	0.03		17.39	1.15	HW
S2	2.08	0.11		2.16	0.10		8.41	1.38	SW
S3	1.76	0.05		1.97	0.03		21.22	0.03	HW
SA	1.63	0.03		1.94	0.01		30.85	0.01	HW
SB	2.01	0.07		2.11	0.05		9.96	2.19	MW
SC	2.05	0.06		2.13	0.05		8.49	1.38	SW
SD	1.78	0.08		1.99	0.03		21.26	5.38	HW
SE	1.87	0.06		2.03	0.03		15.73	3.29	MW
SF	2.09	0.03		2.18	0.02		9.54	0.91	MW
SG	2.27	0.07		2.35	0.05		8.80	2.54	SW

4.3.1.1 Relations between Porosity and Unit Weight (Saturated and Dry)

The relation between porosity, saturated unit weight and dry unit weight was analyzed. An inverse linear relation was observed between saturated unit weight and porosity and between dry unit weight and porosity for all the specimen groups. Strong linear regression values were obtained for these data sets. Thus, the regression linear equations of these lines are reliable. The graphs and regression equations for these relations are presented below.
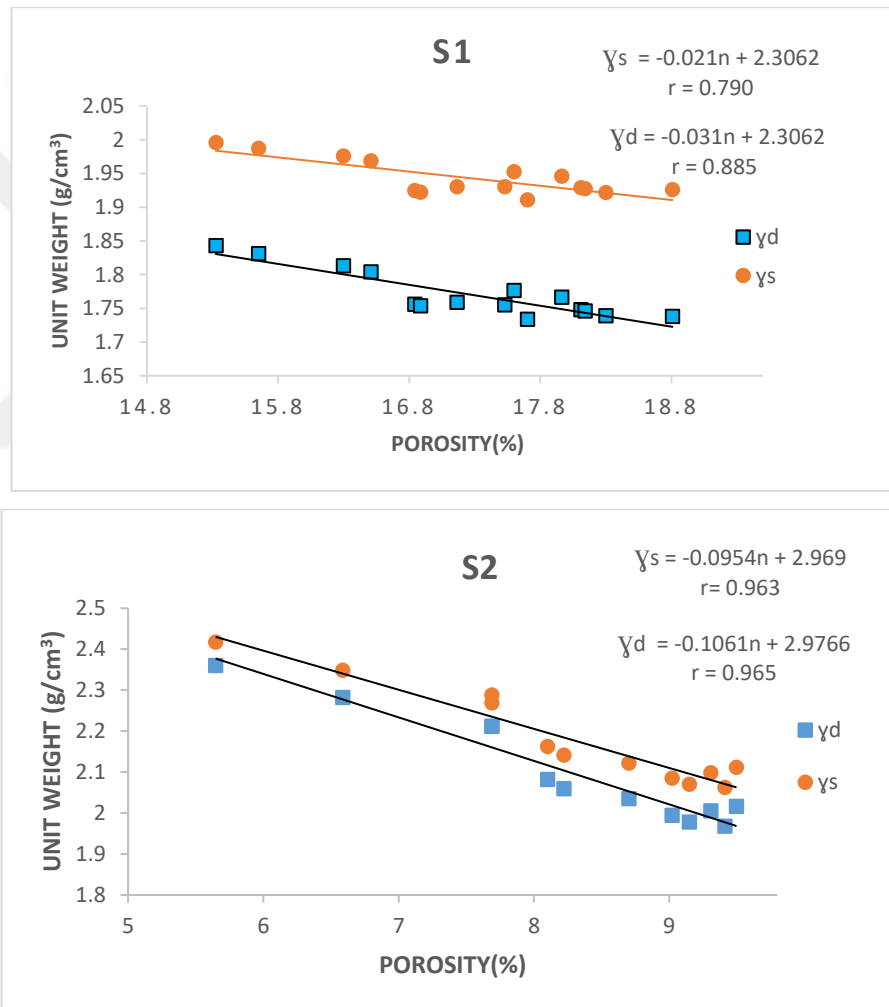
Figure 4.2 Relations between unit weight and porosity (S1 and S2)
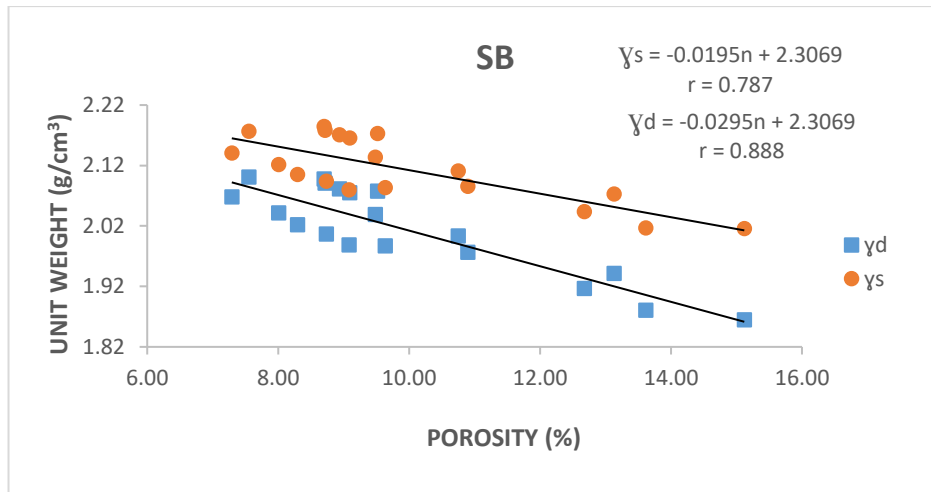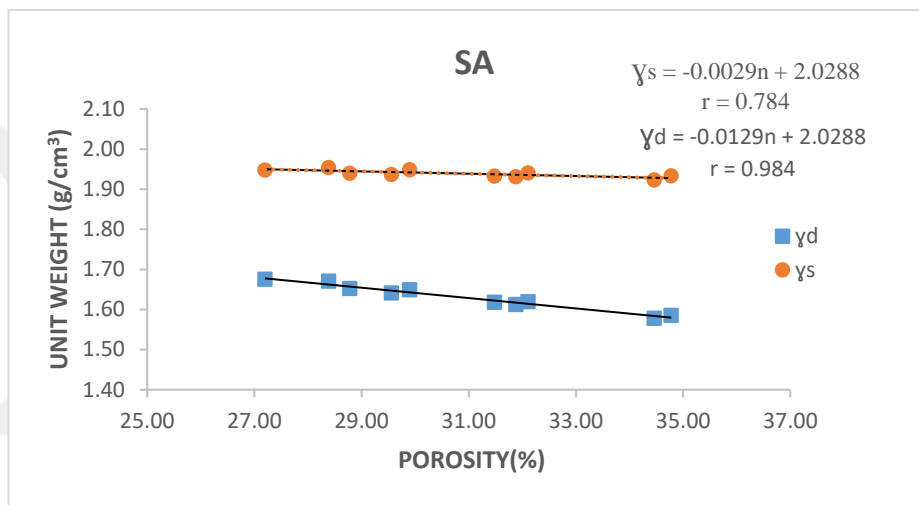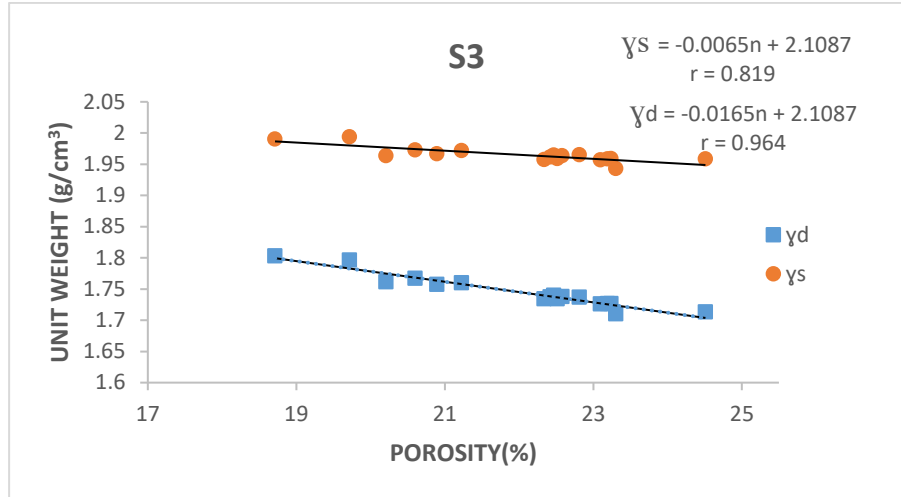
Figure 4.3 Relations between unit weight and porosity (S3, SA and SB)
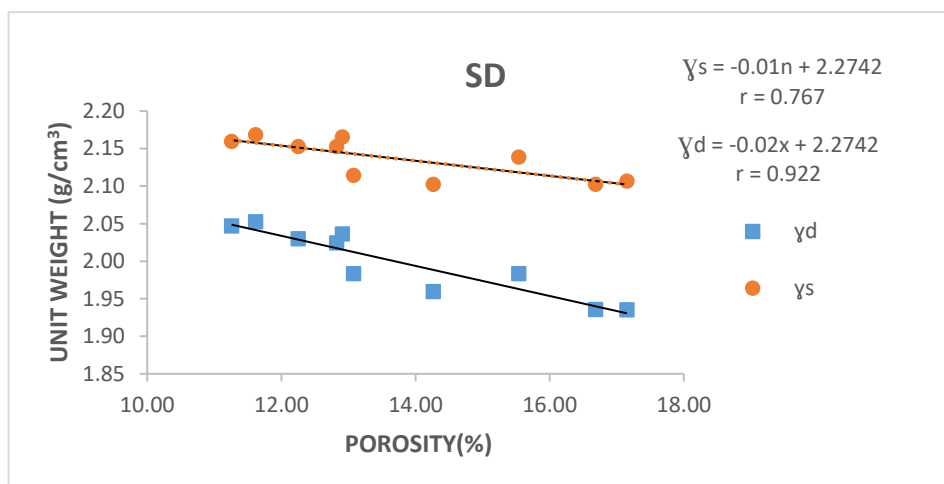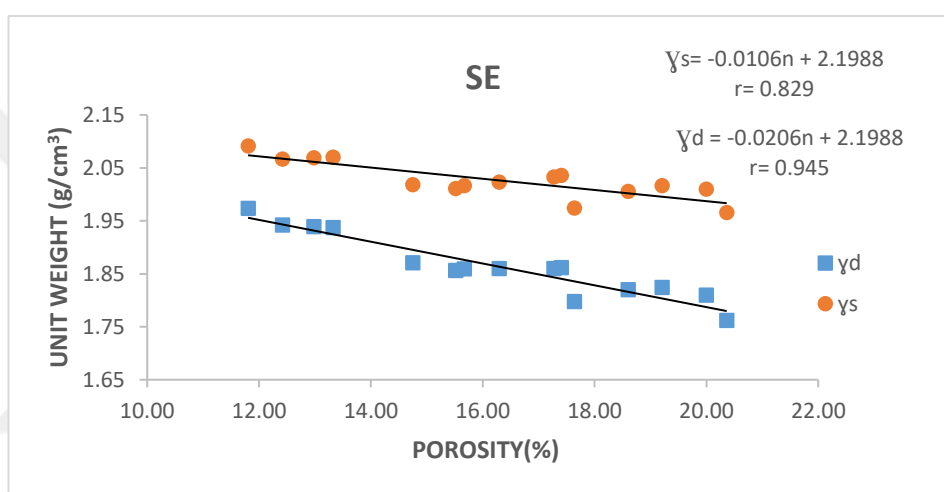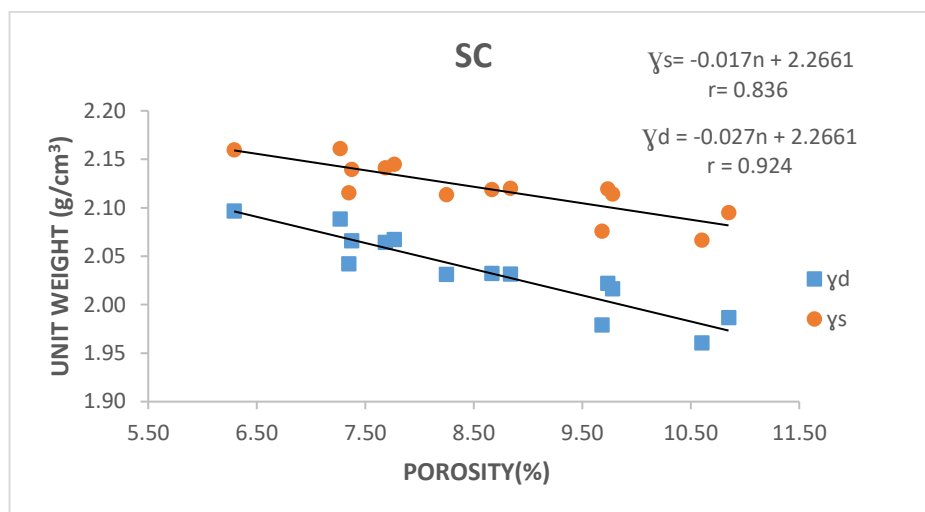
Figure 4.4 Relations between unit weight and porosity (SC, SE and SD)
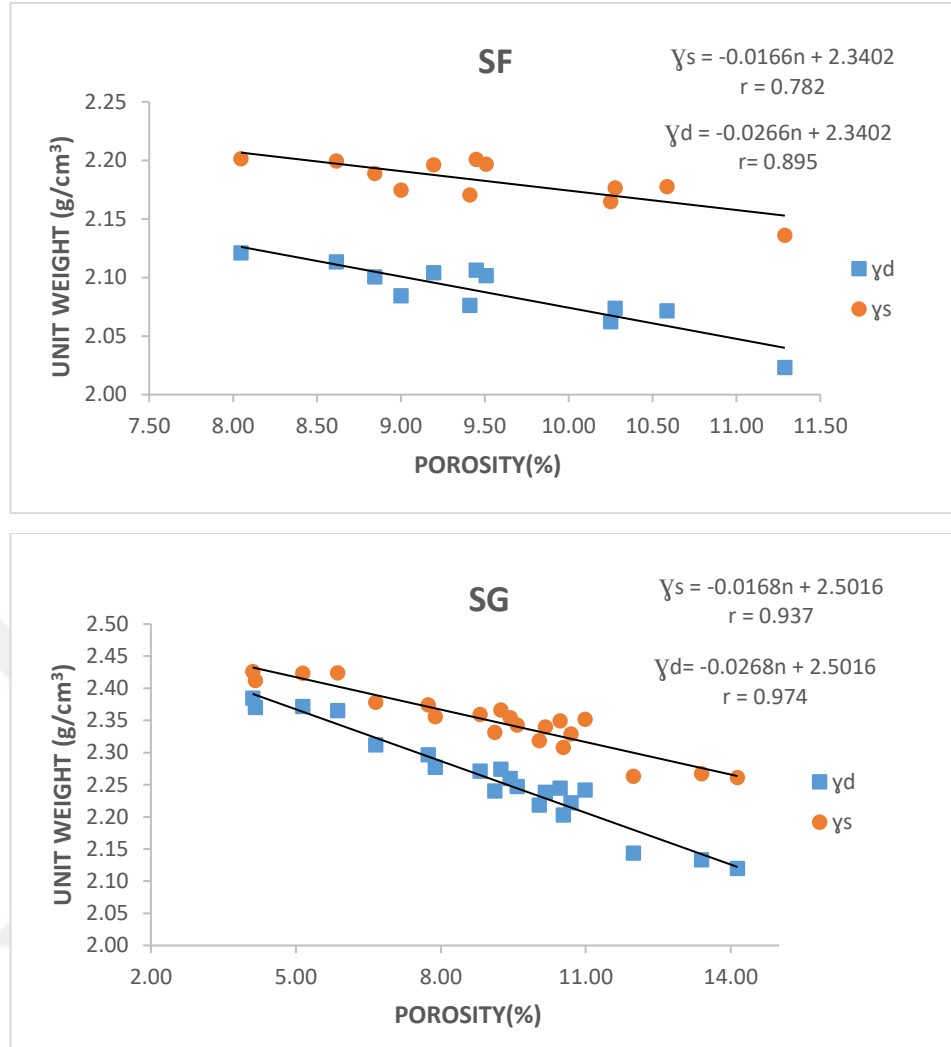
Figure 4.5 Relations between unit weight and porosity (SF and SG)

4.3.2 P-wave Velocity Test on the specimens

P-wave velocity test is a non-destructive method of testing rocks. It can be performed in the laboratory or in the field. It is widely used in many industries, for example, civil and geotechnical engineering. Seismic techniques are useful in predicting the rock mass deformation and stress as well as rock mass characterization and weathering rate (Yagiz, 2011). P-wave velocity tests were conducted on 78 rock specimens (69 core specimens from S1, S2, S3, SC, SE, SF, SG and 9 cube specimens from SD). P-wave velocity tests could not be conducted for SA and SB due to the weathered nature of SA and SB in addition to the presence of multiple joints, which made sample preparation not possible.

The Pundit Lab (Figure 4.6), an ultrasonic pulse velocity instrument, was used for this test. The data and results of the P-wave velocity tests are presented in Table 4.2. P-wave velocity classification (after IAEG, 1979) is presented in Table 4.3.

Figure 4.6 A Pundit device in operation

Table 4.2 Data and results of the P-wave velocity test

Specimen No.	Length (m)	Diameter (mm)	Porosity (n%)	Pundit-Dry (μs)	Pundit-Sat. (μs)	Vp-Dry (m/s)	Vp-Sat. (m/s)
1Ci	0.0884	51.7	17.60	31.9	33.5	2769.9	2637.6
1Ei	0.1032	51.7	18.11	38.0	41.0	2715.0	2516.3
1Di	0.1108	52.1	16.01	38.1	40.9	2909.2	2710.0
1Fi	0.1090	52.2	19.58	41.2	43.9	2646.1	2483.4
1Gi	0.1088	52.2	18.81	41.2	44.2	2640.8	2461.5
1Ji	0.1041	51.7	16.33	36.4	38.7	2859.3	2689.4
1Li	0.1096	51.7	16.84	39.0	41.2	2809.7	2659.7
1Mi	0.0943	51.6	18.14	33.5	36.2	2814.6	2604.7
1Pi	0.0954	51.8	17.17	33.7	35.4	2829.4	2693.5
					X	2777.1	2606.2
					SD	92.9	95.7
2B	0.1149	52.6	10.46	28.9	32.4	3975.8	3546.3
2C	0.1178	52.7	10.82	29.7	33.2	3965.3	3547.3
2H	0.0852	52.6	9.67	20.5	23.8	4154.1	3578.2
21E	0.1195	52.9	6.59	26.1	27.1	4577.8	4408.9
23k	0.0540	52.8	8.10	12.2	13.8	4426.2	3913.0

Table 4.2 Data and results of the P-wave velocity test (cont.)

Specimen No.	Length (m)	Diameter (mm)	Porosity (n%)	Pundit-Dry (μs)	Pundit-Sat. (μs)	Vp-Dry (m/s)	Vp-Sat. (m/s)
2I	0.0764	52.6	7.69	16.9	19.0	4520.7	4021.1
21F	0.1184	52.7	9.15	27.9	31.5	4244.4	3759.4
2L	0.1192	52.5	9.41	29.6	31.8	4028.4	3749.7
2F	0.0770	52.6	9.02	19.2	20.8	4008.9	3700.5
2Ai	0.0735	52.8	9.50	18.6	19.9	3950.5	3692.5
2Bi	0.0741	52.7	8.22	17.5	19.0	4234.3	3900.0
					X	4189.7	3801.5
					SD	231.2	254.1
3Ai	0.1178	53.2	18.71	32.8	34.9	3591.5	3375.4
3Di	0.1150	53.0	22.52	36.5	38.7	3151.5	2972.4
3Ei	0.1109	53.3	20.60	32.8	35.2	3381.7	3151.1
3Fi	0.1078	53.1	20.21	30.9	33.7	3488.3	3198.5
3Gi	0.1008	53.3	23.30	32.4	35.4	3111.4	2847.7
3Hi	0.0926	53.1	17.78	24.0	27.1	3856.3	3415.1
3Ii	0.0839	53.1	20.90	25.0	27.0	3356.0	3107.4
3D	0.1195	53.2	23.19	37.3	42.2	3204.3	2832.2
3H	0.0739	53.2	22.47	22.2	26.2	3330.2	2821.8
					X	3385.7	3080.2
					SD	234.9	227.2
SC 2A	0.1009	53.7	8.27	23.5	24.8	4291.9	4066.9
SC3A	0.1064	54.7	10.60	25.6	26.5	4157.4	4016.2
SC4A	0.0978	54.3	9.78	23.2	24.1	4214.2	4056.8
SC5A	0.0868	54.0	9.73	20.4	21.4	4254.9	4056.1
SC6A	0.0901	53.6	7.68	20.8	21.9	4330.3	4112.8
SC7A	0.1099	54.0	6.92	25.6	26.5	4293.4	4147.5
SC8A	0.0969	54.4	8.80	22.9	23.7	4232.8	4089.9
SC10A	0.0984	54.0	7.35	22.7	24.0	4333.5	4098.8
SC11A	0.0905	54.2	7.66	21.0	21.9	4309.5	4132.4
					X	4268.7	4086.4
					SD	58.8	41.6
SD1A	0.0706	70.6	19.08	24.9	26.2	2835.3	2694.7
SD2A	0.0705	70.8	15.26	24.0	25.6	2937.5	2753.9

Table 4.2 Data and results of the P-wave velocity test (cont.)

Specimen No.	Length (m)	Diameter (mm)	Porosity (n%)	Pundit-Dry (μs)	Pundit-Sat. (μs)	Vp-Dry (m/s)	Vp-Sat. (m/s)
SD3A	0.0701	70.1	15.07	23.4	25.4	2995.3	2759.4
SD4A	0.0709	70.4	17.90	24.8	26.1	2858.1	2715.7
SD5A	0.0703	70.1	18.67	24.5	26.3	2869.8	2673.4
SD7A	0.0708	70.6	16.16	23.8	25.7	2975.6	2755.6
SD8A	0.0708	70.5	20.40	25.8	26.9	2743.0	2630.9
SD15A	0.0706	70.5	14.55	23.3	25.2	3029.6	2801.2
SD16A	0.0706	69.5	16.13	24.0	25.8	2941.3	2736.0
					X	2909.5	2724.5
					SD	90.4	51.7
SE1A	0.0780	53.5	16.60	26.4	28.5	2955.3	2738.5
SE2A	0.1115	53.3	12.50	32.3	35.8	3451.1	3113.7
SE3A	0.1004	53.6	17.64	35.2	37.9	2852.3	2649.1
SE4A	0.0704	53.1	14.27	21.3	24.6	3305.6	2862.2
SE5A	0.0853	53.4	13.03	25.0	27.8	3413.8	3068.7
SE6A	0.0901	53.6	17.36	31.7	34.4	2842.6	2619.5
SE7A	0.0751	53.7	11.80	20.6	23.5	3652.7	3195.7
SE8A	0.0881	53.8	14.75	26.1	30.9	3375.5	2847.4
SE9A	0.0730	54.0	15.51	23.4	25.5	3121.4	2864.3
SE10A	0.0831	53.5	16.32	27.0	29.8	3076.3	2787.2
					X	3204.7	2874.6
					SD	276.0	194.7
SF1A	0.0837	53.7	9.63	24.9	23.7	3360.2	3530.4
SF2A	0.0851	53.5	9.41	24.8	24.0	3431.5	3544.4
SF3A	0.0862	53.3	8.05	23.5	22.8	3668.1	3780.7
SF4A	0.0813	54.1	9.53	23.9	23.3	3400.8	3488.4
SF5A	0.1005	53.5	8.62	27.9	27.3	3602.2	3681.3
SF6A	0.1010	53.8	9.12	28.8	27.8	3505.2	3631.3
SF7A	0.0953	53.5	8.84	26.8	25.9	3555.2	3678.8
SF8A	0.0879	54.2	9.59	26.2	25.3	3355.3	3474.7
SF9A	0.0909	54.3	9.00	25.9	25.1	3509.3	3621.1
SF10A	0.0804	53.6	9.19	23.0	22.2	3494.8	3628.9
SF11A	0.0929	53.8	8.53	25.9	25.1	3594.2	3701.6
					X	3497.9	3614.7
					SD	102.8	95.8

Table 4.2 Data and results of the P-wave velocity test (cont.)

Specimen No.	Length (m)	Diameter (mm)	Porosity (n%)	Pundit-Dry (µs)	Pundit-Sat. (µs)	Vp-Dry (m/s)	Vp-Sat. (m/s)
SG1	0.0739	53.6	6.65	16.8	17.2	4397.0	4294.8
SG2	0.1101	53.4	7.89	25.5	26.0	4317.6	4234.6
SG3	0.0742	53.3	9.16	17.3	17.8	4291.3	4170.8
SG4	0.0722	53.3	9.12	16.9	17.2	4274.0	4199.4
SG5	0.0763	52.8	10.69	18.1	18.4	4216.6	4147.8
SG6	0.0803	53.2	10.04	18.9	19.3	4249.7	4161.7
SG7	0.0761	52.7	6.39	17.2	17.7	4426.2	4301.1
SG8	0.0949	53.3	8.16	22.0	22.4	4314.1	4237.1
SG9	0.0980	53.3	7.24	22.5	23.0	4357.0	4260.4
SG10	0.1101	53.4	5.44	24.8	25.1	4439.5	4386.5
					X	4328.3	4239.4
					SD	75.1	74.3

Table 4.3 P-wave velocity classification (after IAEG, 1979)

Vp (m/s)	Description
<2500	Very Low
2500-3500	Low
3500-4000	Moderate
4000-5000	High
>5000	Very High

4.3.2.1 Relations between P-Wave Velocity and Porosity

Relations between P-wave velocity and porosity were analyzed for each of the groups of specimens. Inverse linear relations were obtained between P-wave velocity and porosity for all specimen groups. The graphs and regression equations for these relations are presented in Figure 4.7, 4.8 and 4.9.
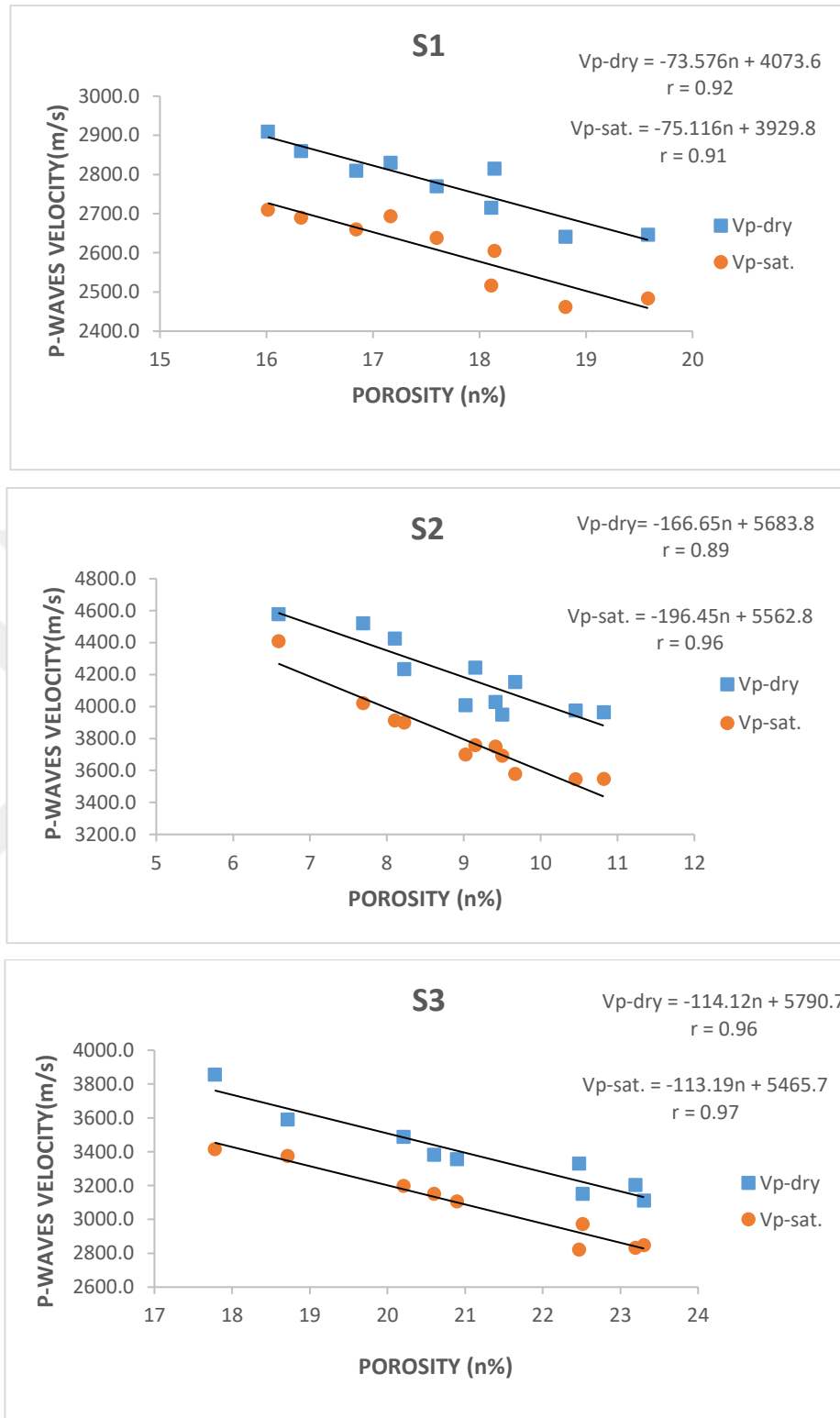
Figure 4.7 Relations between P-wave velocity (Vp-dry, Vp-sat.) and porosity (S1, S2 and S3)
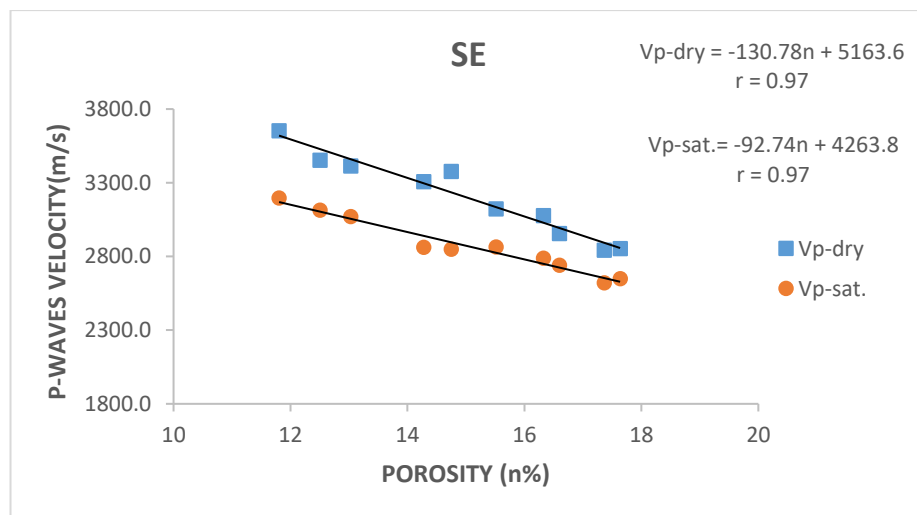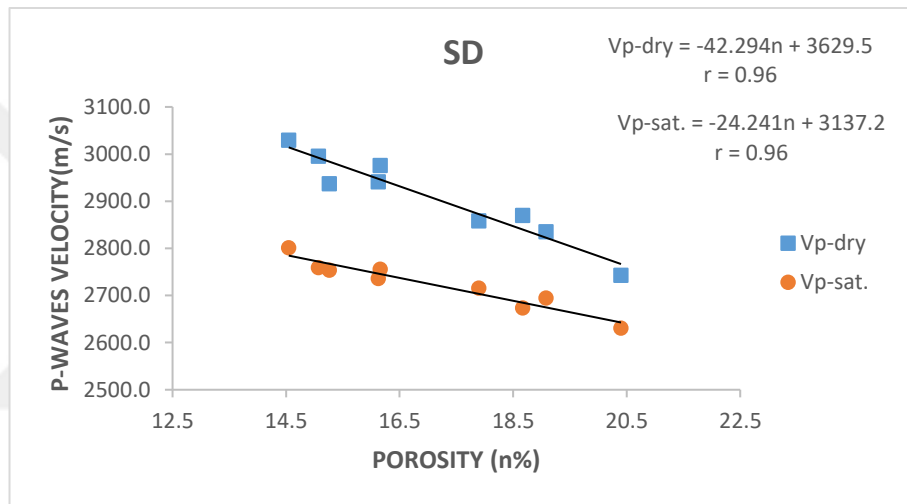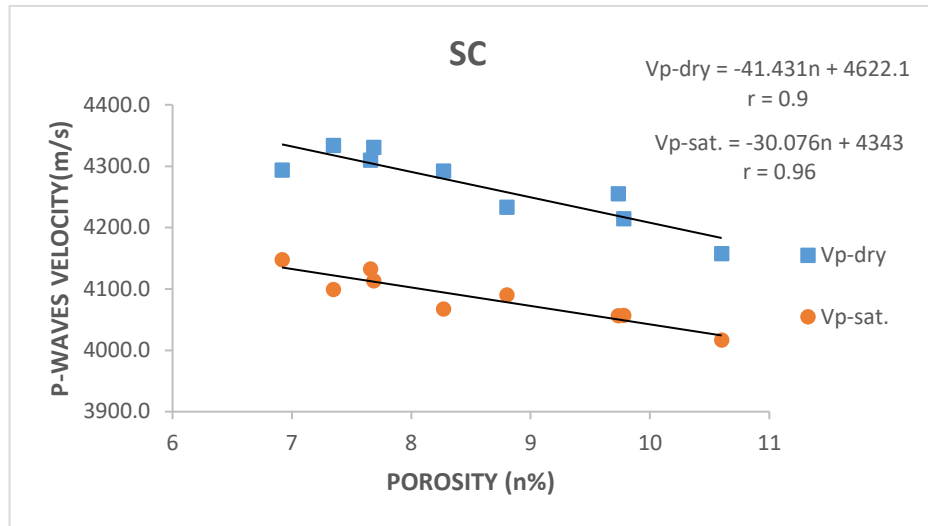
Figure 4.8 Relations between P-wave velocity (Vp-dry, Vp-sat.) and porosity (SC, SD and SE)
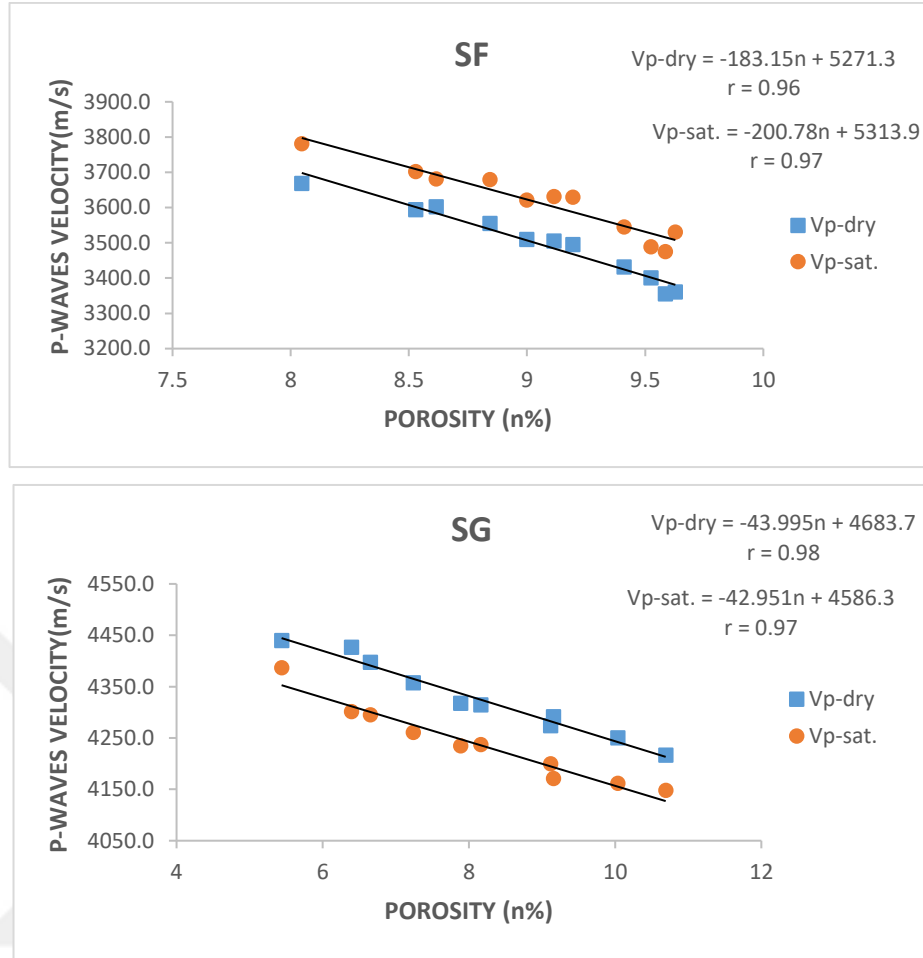
Figure 4.9 Relations between P-wave velocity (Vp-dry, Vp-sat.) and porosity (SF and SG)

4.3.3 Uniaxial Compressive Strength (UCS) Test

Uniaxial Compressive Strength (UCS) tests were conducted on 111 core specimens from S1, S2, S3, SC, SE, SF, SG and 15 cube specimens from SD. The tests were conducted according to ASTM D7012-14. UCS tests were conducted on both saturated (sat.) and dry specimens. As prescribed by ASTM (2014), the core specimens were cut to recommended lengths and the ends were flattened with a diamond-cutting blade. UCS is useful in determining the strength of intact rock. An image of some of the specimens prepared for the UCS test is presented in Figure 4.10. UCS tests could not be conducted for SA and SB due to their weathered nature and the presence of multiple joints.

Figure 4.10 Specimens prepared for UCS test

The specimens were placed in a loading chamber and subjected to confining pressure. The load at failure was recorded for each specimen. A correction factor was used to correct the UCS values of specimens which could not meet the required diameter to length ratio of 1:2. This factor is given below.

$$\sigma c' = \frac{\sigma c}{\frac{b}{h}*0.24+0.88} \tag{4.1}$$

Where b= specimen diameter and h=specimen length.
σc' = corrected uniaxial compressive strength

An image of one of the specimens in a loading chamber is presented in Figure 4.11 while an image of some of the specimens at failure is presented in Figure 4.12. The calculated UCS values are presented in Table 4.4.
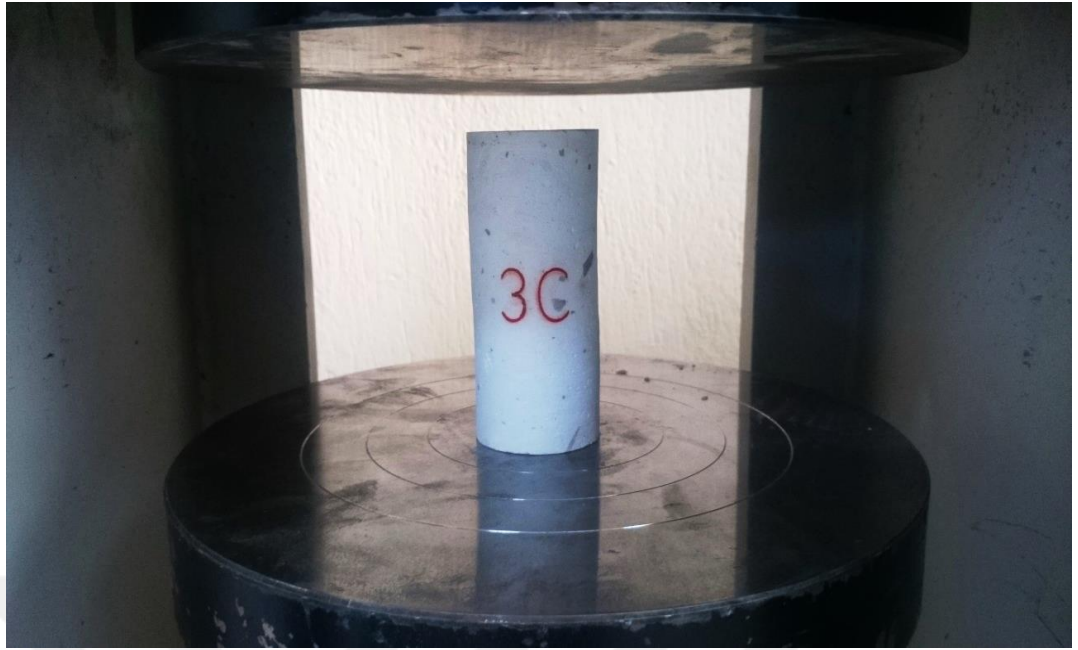
Figure 4.11 Core specimen in a loading chamber
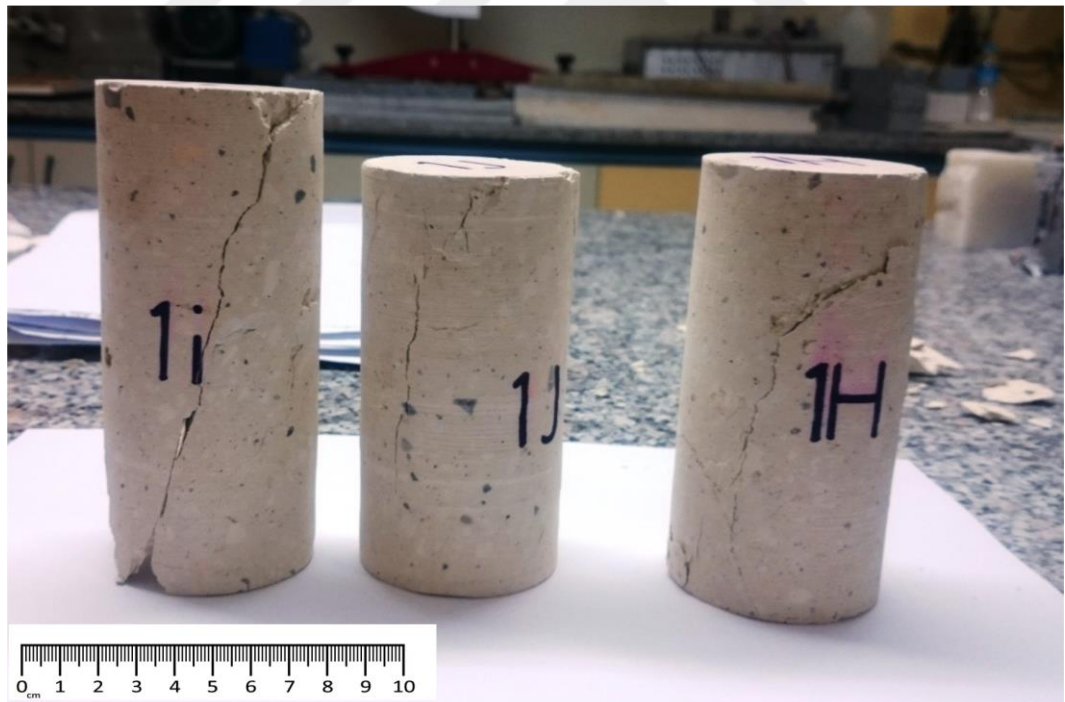
Figure 4.12 Core specimens at failure

Table 4.4 Table of UCS values

Specimen No.	Length (mm)	Diameter (mm)	n (%)	Failure Load (kN)	Area (mm²)	UCS MPa	UCS Corrected MPa	State
1Bi	111.1	51.7	16.5	56.6	2095.5	27.01	27.24	dry
1Di	110.8	51.6	16.0	52.0	2089.0	24.89	25.10	dry
1Fi	109.0	52.2	19.6	44.8	2143.6	20.90	21.00	dry
1Gi	108.8	52.1	18.8	46.5	2133.0	21.80	21.91	dry
1Hi	107.3	52.2	17.7	53.2	2140.4	24.86	24.94	dry
1Ii	119.9	52.0	16.3	50.8	2122.4	23.94	24.32	dry
1L	119.0	53.2	20.5	42.5	2223.2	19.12	19.36	dry
1Ji	104.1	51.9	16.3	58.1	2119.1	27.41	27.41	dry
						X	23.91	
						SD	2.91	
1NF	96.4	53.3	17.0	38.1	2229.8	17.09	16.87	sat.
1NN	76.9	53.6	18.3	29.7	2252.5	13.19	12.59	sat.
1NX	85.5	53.2	18.7	25.4	2224.8	11.42	11.09	sat.
1NY	90.6	53.3	18.5	28.0	2230.7	12.55	12.29	sat.
1NM	88.1	53.3	18.1	32.9	2234.0	14.72	14.35	sat.
1NB	87.0	53.3	19.9	25.2	2228.2	11.31	11.01	sat.
1NZ	94.6	53.4	18.9	25.0	2235.7	11.18	11.01	sat.
						X	12.75	
						SD	2.18	
2B	114.9	52.6	10.5	54.9	2174.9	25.24	25.50	dry
2K	119.0	53.1	8.6	90.2	2217.3	40.68	41.21	dry
21F	118.4	53.0	7.7	100.4	2208.1	45.47	46.05	dry
2C	117.8	52.7	10.8	39.1	2179.9	17.94	18.17	dry
2H	85.2	52.7	9.7	70.0	2184.0	32.05	31.16	dry
2L	119.2	52.6	9.1	52.0	2170.0	23.96	24.31	dry
21J	119.5	53.0	8.6	61.0	2207.3	27.64	28.02	dry
2F	77.0	52.9	9.4	53.0	2198.2	24.11	23.07	dry
21E	119.5	52.7	6.6	98.0	2180.7	44.94	45.58	dry
2Di	72.2	52.8	6.3	120.0	2185.7	54.90	52.02	dry
2Ei	74.4	52.7	7.4	89.2	2179.9	40.92	38.97	dry
						X	34.01	
						SD	11.23	
2NO	103.2	54.3	9.9	42.9	2311.8	18.56	18.44	sat.
2NI	103.4	53.8	10.1	39.8	2275.3	17.49	17.41	sat.

Table 4.4 Table of UCS values (cont.)

Specimen No.	Length (mm)	Diameter (mm)	n (%)	Failure Load (KN)	Area (mm²)	UCS MPa	UCS Corrected MPa	State
2ND	97.4	53.4	5.5	63.7	2239.1	28.45	28.12	sat.
2NP	98.8	53.3	8.0	46.9	2234.0	20.99	20.79	sat.
2NS	82.7	53.2	6.5	66.4	2223.2	29.87	28.88	sat.
2NJ	90.4	53.3	7.8	51.3	2231.5	22.99	22.50	sat.
2NR	68.2	53.5	8.6	50.0	2245.8	22.26	20.84	sat.
2NP	98.8	53.3	7.1	50.7	2234.0	22.69	22.48	sat.
						X	22.43	
						SD	4.15	
3Bi	112.4	52.8	21.2	59.4	2187.6	27.15	27.35	dry
3Ci	117.1	52.4	19.6	59.5	2156.0	27.60	27.95	dry
3Di	115.0	52.7	22.5	45.5	2182.0	20.85	21.06	dry
3Hi	92.6	52.1	17.8	72.0	2128.9	33.82	33.32	dry
3E	119.2	53.0	22.3	56.5	2203.1	25.65	25.99	dry
3F	89.7	53.2	22.6	52.1	2223.2	23.44	22.92	dry
3C	96.3	53.1	19.7	64.4	2212.3	29.11	28.76	dry
3D	119.5	53.1	23.2	37.3	2214.0	16.85	17.08	dry
31L	119.0	53.2	20.5	51.5	2223.2	23.17	23.46	dry
						X	25.32	
						SD	4.78	
3NJ	96.1	53.3	21.8	22.3	2229.8	10.00	9.87	sat.
3NC	96.3	53.3	19.0	43.1	2234.9	19.29	19.04	sat.
3NK	90.7	53.8	20.7	27.8	2272.7	12.23	11.96	sat.
3NB	94.3	53.7	18.0	41.9	2261.8	18.53	18.22	sat.
3NE	95.2	53.3	17.8	35.4	2229.0	15.88	15.66	sat.
3NF	100.9	53.2	19.2	36.3	2225.7	16.31	16.20	sat.
3NL	106.5	53.4	19.6	28.7	2237.4	12.83	12.82	sat.
3ND	100.5	53.3	20.3	30.0	2229.0	13.46	13.36	sat.
						X	14.64	
						SD	3.17	
SC 2A	100.9	53.7	8.3	104.0	2265.1	45.91	45.56	dry
SC4A	97.8	54.3	10.0	89.6	2315.2	38.70	38.19	dry
SC5A	86.8	54.0	9.8	97.2	2290.5	42.44	41.23	dry
SC7A	109.9	54.0	9.0	102.7	2291.4	44.82	44.91	dry
SC9A	98.7	53.7	9.3	99.8	2262.6	44.11	43.65	dry
SC11A	90.5	54.2	10.6	79.5	2309.2	34.43	33.63	dry

Table 4.4 Table of UCS values (cont.)

Specimen No.	Length (mm)	Diameter (mm)	n (%)	Failure Load (kN)	Area (mm²)	UCS MPa	UCS Corrected MPa	State
SC12A	88.7	53.7	10.6	82.0	2265.1	36.20	35.30	dry
SC14A	96.2	53.6	9.3	98.0	2256.7	43.43	42.84	dry
						X	**40.66**	
						SD	**4.48**	
SC15A	89.6	53.8	7.2	90.0	2273.6	39.59	38.65	sat.
SC16A	78.7	53.9	10.8	67.0	2282.0	29.36	28.11	sat.
SC13A	96.1	53.5	8.2	77.6	2251.7	34.46	34.00	sat.
SC6A	90.1	53.6	8.8	79.2	2258.4	35.07	34.28	sat.
SC8A	96.9	54.4	8.7	74.0	2324.6	31.83	31.37	sat.
SC10A	98.4	54.0	7.8	79.6	2288.8	34.78	34.38	sat.
SC3A	106.4	54.7	9.7	68.7	2350.3	29.23	29.13	sat.
						X	**32.85**	
						SD	**3.60**	
SD1A	70.6	70.6	25.7	43.7	3911.9	11.17	11.17	dry
SD2A	70.5	70.8	23.2	47.8	3937.4	12.14	12.14	dry
SD3A	70.1	70.1	15.4	57.9	3861.1	15.00	15.00	dry
SD4A	70.9	70.4	27.0	38.8	3894.2	9.96	9.96	dry
SD5A	70.3	70.1	18.8	50.1	3860.0	12.98	12.98	dry
SD7A	70.8	70.6	15.4	56.1	3911.9	14.34	14.34	dry
SD8A	70.8	70.5	16.1	59.8	3908.6	15.30	15.30	dry
SD9A	70.7	70.6	17.4	59.1	3910.8	15.11	15.11	dry
						X	**13.25**	
						SD	**2.01**	
SD10A	71.0	70.0	14.1	39.1	3845.7	10.17	10.17	sat.
SD11A	70.6	70.4	26.0	30.7	3897.5	7.88	7.88	sat.
SD12A	70.8	70.1	23.6	28.7	3860.0	7.44	7.44	sat.
SD13A	70.7	70.3	22.4	30.9	3879.8	7.95	7.95	sat.
SD15A	70.6	70.5	18.4	36.6	3901.9	9.39	9.39	sat.
SD16A	70.6	69.5	28.7	21.7	3792.0	5.73	5.73	sat.
SD17A	70.2	70.1	26.0	25.9	3860.0	6.71	6.71	sat.
						X	**7.89**	
						SD	**1.51**	
SE1A	78.0	53.5	18.6	36.1	2248.3	16.06	15.37	dry
SE2A	111.5	53.3	13.5	47.0	2230.7	21.07	21.18	dry
SE3A	100.4	53.6	17.6	36.1	2258.4	15.98	15.86	dry
SE4A	70.4	53.1	17.3	35.6	2214.8	16.07	15.15	dry

Table 4.4 Table of UCS values (cont.)

Specimen No.	Length (mm)	Diameter (mm)	n (%)	Failure Load (KN)	Area (mm²)	UCS MPa	UCS Corrected MPa	State
SE5A	85.3	53.4	16.3	42.4	2239.9	18.93	18.37	dry
SE6A	90.1	53.6	20.4	30.1	2256.7	13.34	13.04	dry
SE7A	75.1	53.7	13.8	45.9	2265.1	20.26	19.27	dry
						X	16.89	
						SD	2.81	
SE8A	88.1	53.8	17.7	20.6	2274.4	9.06	8.82	sat.
SE9A	73.0	54.0	15.1	28.7	2288.8	12.54	11.86	sat.
SE10A	83.1	53.5	16.3	25.1	2251.7	11.15	10.77	sat.
SE11A	77.6	53.4	14.0	27.9	2239.9	12.46	11.92	sat.
SE12A	80.6	53.1	16.0	25.2	2215.6	11.37	10.96	sat.
SE13A	82.6	53.1	17.4	22.6	2217.3	10.19	9.85	sat.
SE14A	88.0	53.7	19.2	19.8	2266.8	8.73	8.51	sat.
						X	10.38	
						SD	1.37	
SF1A	83.7	53.7	10.1	59.5	2261.8	26.31	25.44	dry
SF2A	85.1	53.5	9.3	68.5	2244.9	30.51	29.60	dry
SF3A	86.2	53.3	10.0	54.7	2233.2	24.49	23.82	dry
SF4A	81.3	54.1	10.2	54.4	2300.7	23.64	22.74	dry
SF5A	100.5	53.5	9.6	66.7	2245.8	29.70	29.47	dry
SF6A	101.0	53.8	9.6	60.7	2273.6	26.70	26.49	dry
SF7A	95.3	53.5	9.0	78.0	2244.9	34.76	34.26	dry
SF8A	87.9	54.2	10.6	56.4	2310.9	24.41	23.74	dry
						X	26.95	
						SD	3.91	
SF9A	90.9	54.3	8.6	58.9	2313.5	25.46	24.88	sat.
SF10A	80.4	53.6	9.2	49.7	2256.7	22.02	21.18	sat.
SF11A	92.9	53.8	10.3	38.8	2275.3	17.05	16.73	sat.
SF12A	97.7	53.7	9.2	44.6	2266.0	19.68	19.45	sat.
SF13A	75.4	53.9	10.1	43.7	2282.9	19.14	18.20	sat.
SF14A	88.6	53.8	9.3	45.8	2271.9	20.16	19.66	sat.
SF15A	100.7	53.6	9.7	44.0	2257.6	19.49	19.34	sat.
						X	19.92	
						SD	2.58	
SG1	73.9	53.6	7.7	135.7	2255.0	60.18	57.09	dry
SG2	110.1	53.4	9.6	106.6	2238.2	47.63	47.80	dry
SG3	64.2	53.3	9.0	124.2	2232.4	55.64	51.55	dry

Table 4.4 Table of UCS values (cont.)

Specimen No.	Length (mm)	Diameter (mm)	n (%)	Failure Load (KN)	Area (mm²)	UCS MPa	UCS Corrected MPa	State
SG4	72.2	53.3	10.5	106.8	2234.0	47.81	45.22	dry
SG5	66.3	52.8	8.0	125.5	2186.5	57.40	53.60	dry
SG6	70.3	53.2	8.2	125.7	2222.3	56.56	53.28	dry
SG7	66.1	52.7	10.0	108.7	2183.2	49.79	46.47	dry
1SG8	94.9	53.3	9.2	110.2	2230.7	49.40	48.68	dry
						X	**50.46**	
						SD	**4.08**	
SG9	98.0	53.3	9.4	97.2	2233.2	43.53	43.07	sat.
SG10	110.1	53.4	6.5	105.8	2238.2	47.27	47.44	sat.
SG11	92.7	53.3	6.9	105.6	2232.4	47.30	46.47	sat.
SG12	86.7	53.4	7.1	103.9	2236.5	46.46	45.21	sat.
SG13	100.6	53.4	7.1	104.5	2239.9	46.65	46.31	sat.
SG14	100.7	53.4	8.8	97.6	2237.4	43.62	43.31	sat.
SG15	77.8	53.4	10.0	100.1	2237.4	44.74	42.83	sat.
SG16	92.1	53.1	8.0	100.2	2216.5	45.21	44.39	sat.
						X	**44.88**	
						SD	**1.75**	

4.3.3.1 Relations between Uniaxial Compressive Strength and Porosity

Analyses were conducted to determine the relations between UCS and porosity. An inverse linear relation was found to exist between the two index properties in each case. The graphs and regression equations for these relations are presented below.
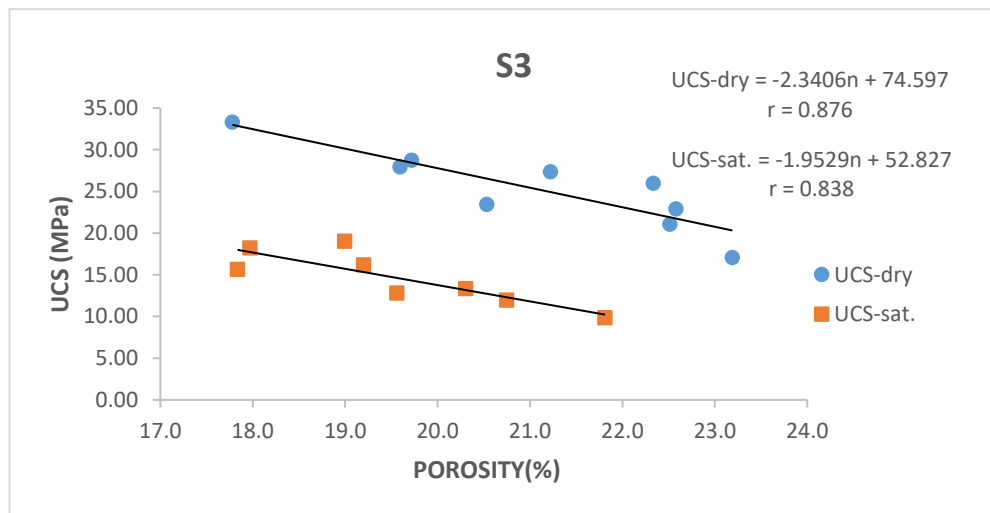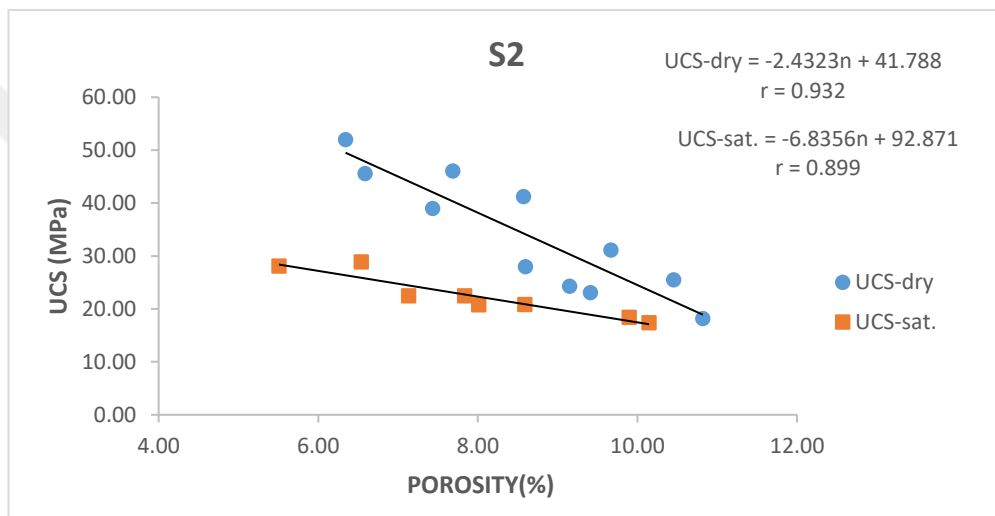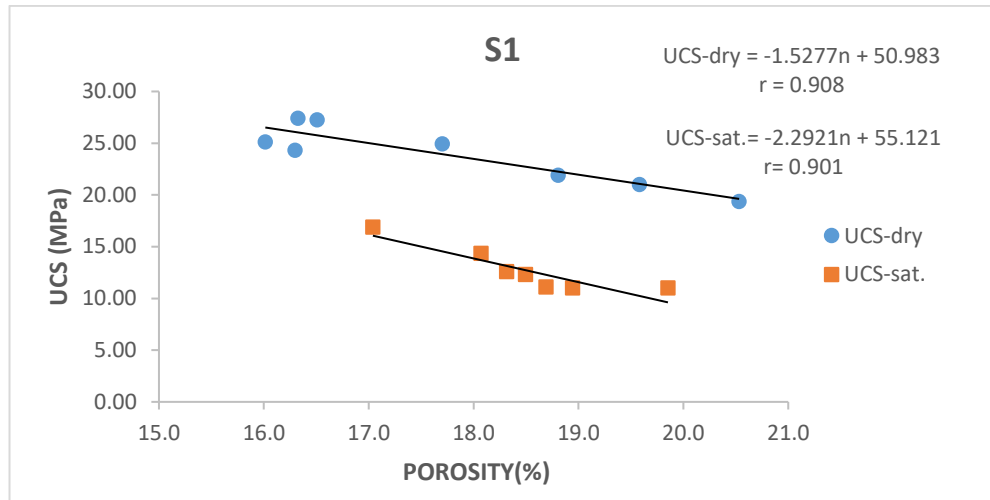
Figure 4.13 Relations between UCS and porosity (S1, S2 and S3)
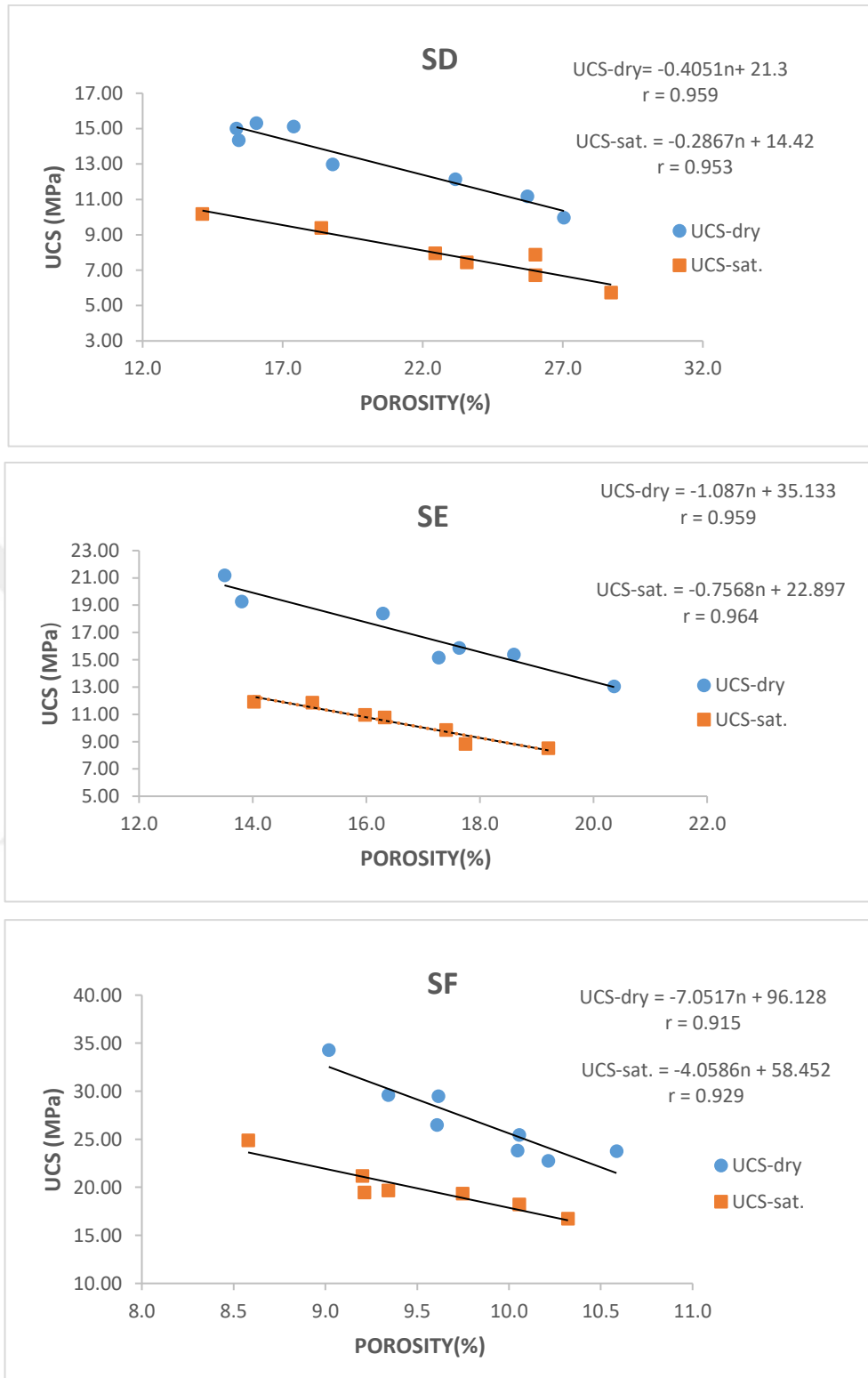
Figure 4.14 Relations between UCS and porosity (SD, SE and SF)
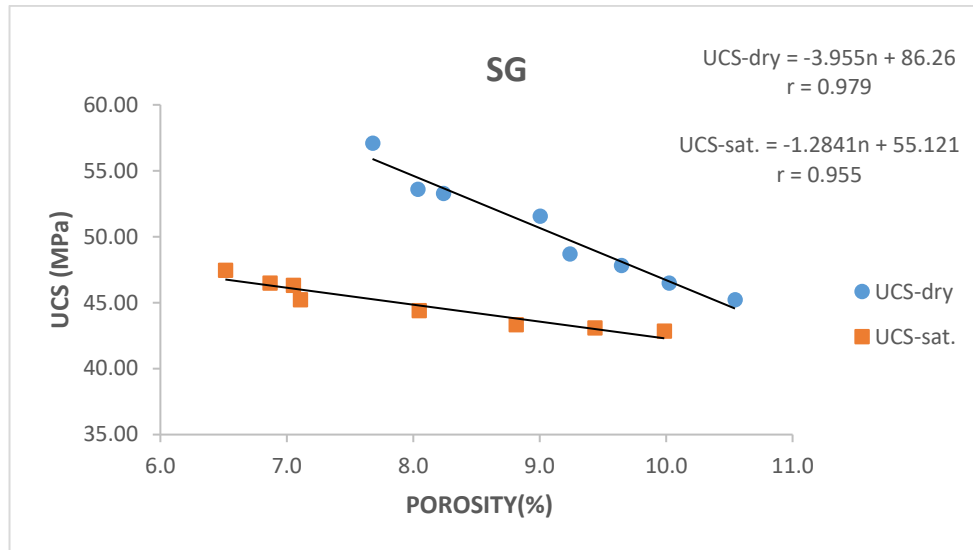
Figure 4.15 Relations between UCS and porosity (SG)

UCS classification after Bieniawski (1989) is presented in Table 4.5.

Table 4.5 Uniaxial Compressive Strength (UCS) Classification (Bieniawski, 1989)

Uniaxial Compressive Strength (MPa)	Designation
> 200	Very high strength
100-200	High strength
50-100	Medium
25-50	Low Strength
<25	Very low strength

4.3.4 Point Load Index Test

Point Load Index Test was conducted on 118 block and core specimens prepared from samples obtained from the field. Specimens were chosen from each of the ten slopes.

The test was conducted according to ASTM D5731-16. According to ASTM (2008), Point Load Index test can be conducted both in the laboratory and in the field on rock cores, blocks or irregular lumps with a diameter between 30-85 mm and is suitable for estimating the uniaxial compressive strength of a rock within a short time interval. An image of a specimen being tested in a loading frame is presented in Figure 4.16.

Figure 4.16. Point Load Test- specimen in a loading frame

A Size Correction Factor (F) was used to correct the obtained Point Load Test values according to ASTM D5731-08. This correction factor is given below.

$$F = (De/50)^{0.45} \tag{4.2}$$

$$Is_{50}(corrected) = Is \times F \tag{4.3}$$

Where F=Size Correction factor

       De = equivalent core diameter

       $Is_{50=}$ Corrected Point load index value

       Is= Uncorrected Point load index value

The data and results of the Point Load Index Tests are presented in Table 4.6 and 4.7

Table 4.6 Table of values for point load index test (S1, S2, S3)

Specimen No.	Diameter (cm)	Length (cm)	De cm	n%	Failure Load (Kg)	Is MPa	Is50-Corrected MPa
1A	5.2	5.3	5.2	17.01	506.0	1.89	1.92
1B	5.4	5.6	5.4	18.11	450.6	1.56	1.61
1E	5.6	5.8	5.6	16.58	574.0	1.83	1.92
1F	5.2	10.9	5.2	18.81	381.3	1.41	1.43
1G	5.4	5.8	5.4	17.70	454.9	1.55	1.61
1N	5.2	4.9	5.2	16.30	481.8	1.77	1.80
1O	5.2	9.5	5.2	17.33	434.5	1.62	1.65
1EE	5.3	8.0	5.3	18.30	399.0	1.42	1.45
						X	1.67
						SD	0.19
2B	5.1	6.1	6.3	10.00	679.4	1.71	1.90
2C	6.3	6.3	7.1	8.04	1048.5	2.07	2.43
2D	5.7	6.3	6.7	6.67	1469.1	3.23	3.70
2E	5.4	5.4	6.1	6.59	1153.3	3.13	3.41

Table 4.6 Table of values for point load index test (S1, S2 and S3) (cont.)

Specimen No.	Diameter (cm)	Length (cm)	De cm	n%	Failure Load (Kg)	Is MPa	Is50-Corrected MPa
2G	5.8	6.4	6.9	8.00	896.2	1.90	2.19
2I	5.8	5.0	6.1	8.60	762.1	2.07	2.26
2CC	7.2	7.1	8.1	8.10	1425.3	2.18	2.70
2EE	5.6	7.2	7.1	9.69	656.5	1.29	1.51
2LL	5.7	8.4	7.8	7.15	1529.1	2.54	3.09
2MM	4.9	9.6	7.7	8.41	1306.7	2.19	2.66
2DD	5.3	8.0	5.3	9.02	474.2	1.68	1.73
						X	2.51
						SD	0.69
3AA	5.3	5.5	6.1	22.52	501.6	1.35	1.48
3BB	5.2	6.3	6.4	20.60	788.7	1.90	2.13
3DD	5.7	6.5	6.9	20.99	692.0	1.46	1.68
3FF	5.8	5.9	6.6	23.30	560.6	1.29	1.46
3GG	5.5	6.8	6.9	20.90	800.8	1.68	1.95
3HH	5.1	6.5	6.5	21.42	698.6	1.67	1.88
3JJ	5.9	6.7	7.1	20.24	839.5	1.66	1.95
3KK	4.9	6.6	6.4	20.81	720.8	1.77	1.98
3LL	5.1	6.5	6.5	21.72	592.5	1.42	1.60
3MM	5.0	5.9	6.1	23.19	419.4	1.13	1.23
3PP	5.5	7.1	7.1	22.34	717.1	1.43	1.68
						X	1.73
						SD	0.27

Table 4.7 Point load index test results (SA, SB, SC, SD, SE, SF and SG)

Specimen No.	Length (mm)	Diameter (mm)	De² mm²	n%	Failure Load (KN)	Is MPa	Is50 Corrected (MPa)
SA1	89.6	76.4	8716.9	31.5	1.7	0.20	0.26
SA2	96.4	53.8	6598.2	29.9	4.0	0.61	0.75
SA3	108.2	79.9	11003.6	28.4	2.6	0.24	0.33
SA4	105.0	40.7	5443.8	28.8	2.0	0.37	0.44
SA5	100.8	73.6	9450.2	31.9	4.2	0.44	0.60
SA9	63.7	46.8	3792.0	34.5	1.3	0.33	0.36
SA11	87.2	71.5	7934.9	34.8	4.3	0.54	0.70
SA12	80.3	62.1	6349.0	32.1	2.1	0.33	0.41
SA13	74.7	43.9	4177.9	29.6	1.9	0.45	0.51
SA14	82.1	50.0	5227.4	27.2	3.0	0.57	0.68
						X	0.50
						SD	0.17
SB3	99.5	50.9	6443.1	9.5	6.0	0.93	1.15
SB7	98.2	70.6	8825.9	9.6	11.0	1.25	1.66
SB8	105.3	57.5	7703.9	7.3	15.0	1.95	2.51
SB9	86.1	57.7	6325.0	8.7	10.0	1.58	1.95
SB11	87.2	67.1	7451.4	8.3	12.5	1.68	2.14
SB14	85.2	65.9	7147.2	9.1	10.0	1.40	1.77
SB18	81.3	56.5	5848.0	8.0	9.5	1.62	1.97
SB19	105.2	65.3	8738.4	8.7	11.0	1.26	1.67
SB24	90.7	67.2	7760.3	8.9	7.5	0.97	1.25
SB31	68.9	62.9	5520.6	9.1	6.0	1.09	1.30
						X	1.74
						SD	0.43
SC1	73.2	41.2	3841.0	7.3	10.0	2.60	2.87
SC2	89.9	50.9	5820.9	10.6	8.5	1.46	1.77
SC3	78.1	50.8	5046.7	9.8	8.0	1.59	1.86
SC5	81.8	44.7	4658.2	9.5	7.5	1.61	1.85
SC8	67.1	42.6	3641.1	7.7	9.5	2.61	2.84
SC9	76.1	53.3	5166.8	6.3	14.5	2.81	3.30
SC12	82.6	70.9	7450.4	7.3	14.5	1.95	2.49
SC13	112.5	51.3	7348.8	7.2	15.5	2.11	2.69
SC14A	72.1	63.7	5845.3	8.2	12.5	2.14	2.59

Table 4.7 Point load index test results (SA, SB, SC, SD, SE, SF and SG) (cont.)

Specimen No.	Length (mm)	Diameter (mm)	De² mm²	n%	Failure Load (KN)	Is MPa	Is$_{50}$ Corrected (MPa)
SC16	92.9	49.3	5829.9	9.8	9.0	1.54	1.87
SC16A	74.4	67.0	6348.0	8.8	11.5	1.81	2.23
SC17	74.3	56.3	5322.3	8.7	9.5	1.78	2.12
SC19	77.4	47.7	4702.5	9.7	7.5	1.59	1.84
SC21	76.5	60.2	5862.5	7.8	12.0	2.05	2.48
SC30	66.9	48.0	4089.7	9.3	6.5	1.59	1.78
SC32	89.1	49.4	5599.7	9.7	10.0	1.79	2.14
						X	2.29
						SD	0.47
SD2	63.3	54.5	4394.8	26.0	4.5	1.02	1.16
SD3	84.3	48.8	5236.3	23.1	5.0	0.95	1.13
SD4	86.6	56.2	6192.3	15.3	7.1	1.15	1.41
SD5	68.1	52.0	4511.7	31.1	4.1	0.91	1.04
SD6	70.2	48.5	4331.8	18.9	5.0	1.15	1.31
SD12	87.7	62.7	7005.8	15.7	8.6	1.23	1.55
SD13	79.9	63.7	6479.3	16.2	7.0	1.08	1.34
SD16	108.3	72.4	9979.3	17.4	11.0	1.10	1.51
SD20	76.2	60.9	5909.7	14.5	8.0	1.35	1.64
SD21	75.4	47.6	4561.9	26.1	5.2	1.14	1.31
SD24	98.0	52.5	6545.0	23.7	6.7	1.02	1.27
SD25	104.5	43.0	5723.1	22.4	6.2	1.08	1.31
SD26	88.7	73.0	8246.3	18.6	9.0	1.09	1.43
SD27	67.0	61.4	5241.2	28.8	5.0	0.95	1.13
						X	1.32
						SD	0.17
SE1	70.6	54.1	4861.6	18.6	4.5	0.93	1.08
SE2	73.4	40.9	3822.4	8.5	11.5	3.01	3.31
SE3	76.5	43.9	4272.8	17.6	5.0	1.17	1.32
SE5	80.0	37.7	3842.1	17.3	5.0	1.30	1.43
SE7	69.1	56.0	4926.3	12.0	11.5	2.33	2.72
SE8	86.6	59.4	6544.3	20.4	7.0	1.07	1.33
SE9	82.3	51.4	5387.1	11.8	8.5	1.58	1.88
SE10	88.6	46.8	5279.3	14.7	9.0	1.70	2.02

Table 4.7 Point load index test results (SA, SB, SC, SD, SE, SF and SG) (cont.)

Specimen No.	Length (mm)	Diameter (mm)	De^2 mm^2	n%	Failure Load (KN)	Is MPa	Is_{50} Corrected (MPa)
SE17	84.0	47.6	5093.0	17.4	5.0	0.98	1.15
SE18	69.3	39.8	3509.7	19.2	5.2	1.48	1.60
SE19	89.9	46.4	5312.1	14.1	7.5	1.41	1.67
SE20	78.0	43.9	4359.4	15.7	5.0	1.15	1.30
SE22	62.3	57.6	4571.4	20.0	5.4	1.18	1.35
						X	1.70
						SD	0.65
SF1	88.2	50.7	5687.2	10.3	7.4	1.30	1.57
SF5	73.2	68.9	6412.6	8.0	11.3	1.76	2.18
SF7	66.9	61.3	5223.4	10.3	6.7	1.28	1.51
SF8	92.1	65.4	7663.8	8.6	11.6	1.51	1.95
SF11	96.7	53.5	6584.0	8.8	9.4	1.43	1.78
SF13	57.3	67.3	4909.0	10.6	6.7	1.36	1.59
SF15	81.3	64.1	6626.2	9.0	10.6	1.60	1.99
SF16	95.0	59.0	7135.0	9.2	9.9	1.39	1.76
SF18	80.9	59.4	6116.6	11.3	7.0	1.14	1.40
SF20	81.3	52.8	5461.1	9.4	9.2	1.68	2.01
						X	1.77
						SD	0.25
SG2	80.0	54.2	5518.3	7.9	18.1	3.28	3.92
SG5	69.9	48.9	4352.3	9.1	12.0	2.76	3.12
SG6	64.2	45.6	3727.3	10.7	11.0	2.95	3.23
SG12	68.5	48.6	4239.1	13.4	11.0	2.59	2.92
SG14	70.3	54.5	4872.8	10.2	12.6	2.59	3.00
SG16	71.5	51.6	4699.8	9.4	12.0	2.55	2.94
SG21	66.7	61.4	5214.6	5.9	17.3	3.32	3.91
SG24	62.1	53.2	4211.1	4.1	18.0	4.27	4.81
SG25	68.4	60.3	5248.8	6.7	17.9	3.41	4.03
SG26	68.1	60.2	5217.0	8.8	16.0	3.07	3.62
SG28	65.0	61.5	5086.7	11.0	12.0	2.36	2.77
SG29	77.4	57.0	5612.7	10.5	13.0	2.32	2.78
SG30	65.4	57.2	4763.0	7.7	16.0	3.36	3.88
SG34	65.1	53.2	4411.7	10.5	12.0	2.72	3.09
SG37	72.3	58.9	5417.7	4.2	19.0	3.51	4.17
						X	3.48
						SD	0.61

4.3.4.1 Relations between Point Load Index, and Porosity

Analyses were conducted to determine the relation between Point Load Index, and Porosity. An inverse linear relation was found to exist between the two properties in all the ten specimen groups. The graphs and regression equations for these relations are presented below.
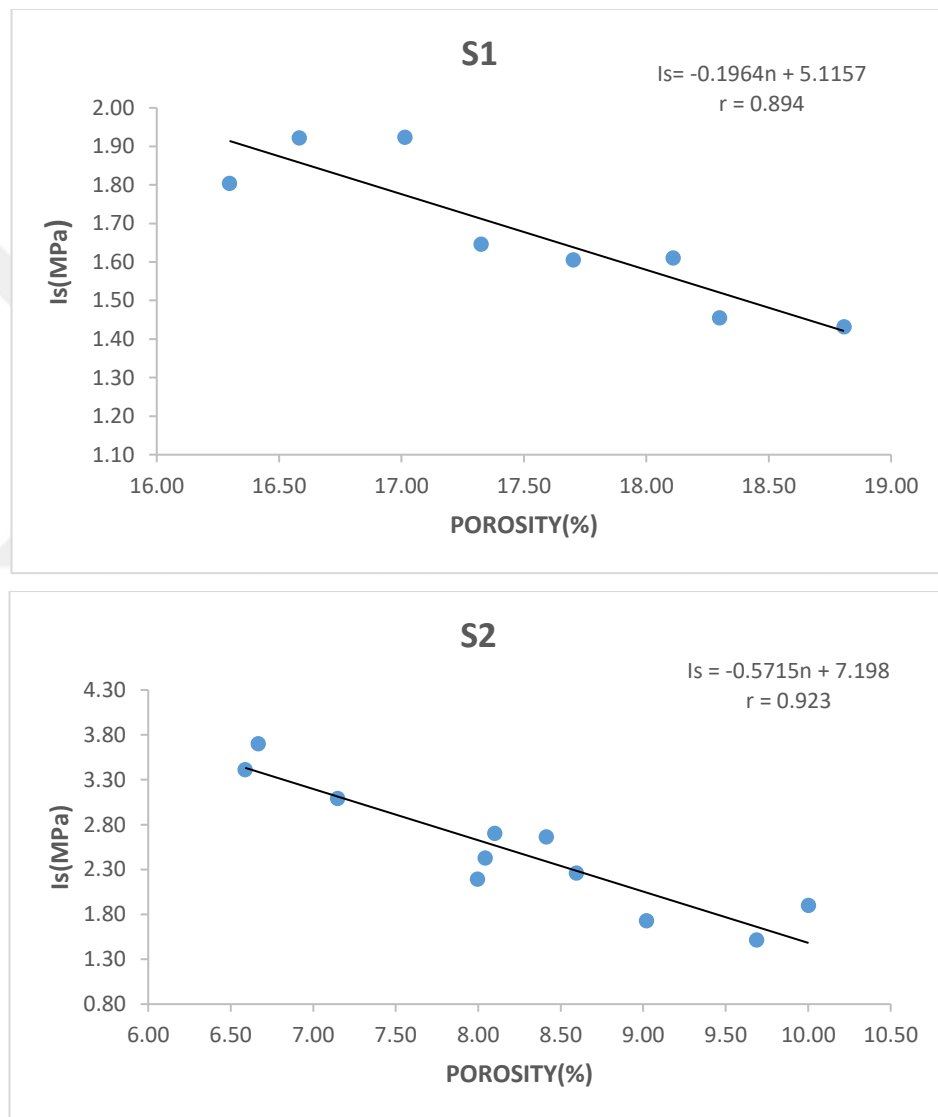

Figure 4.17 Relations between point load index and porosity (S1 and S2)
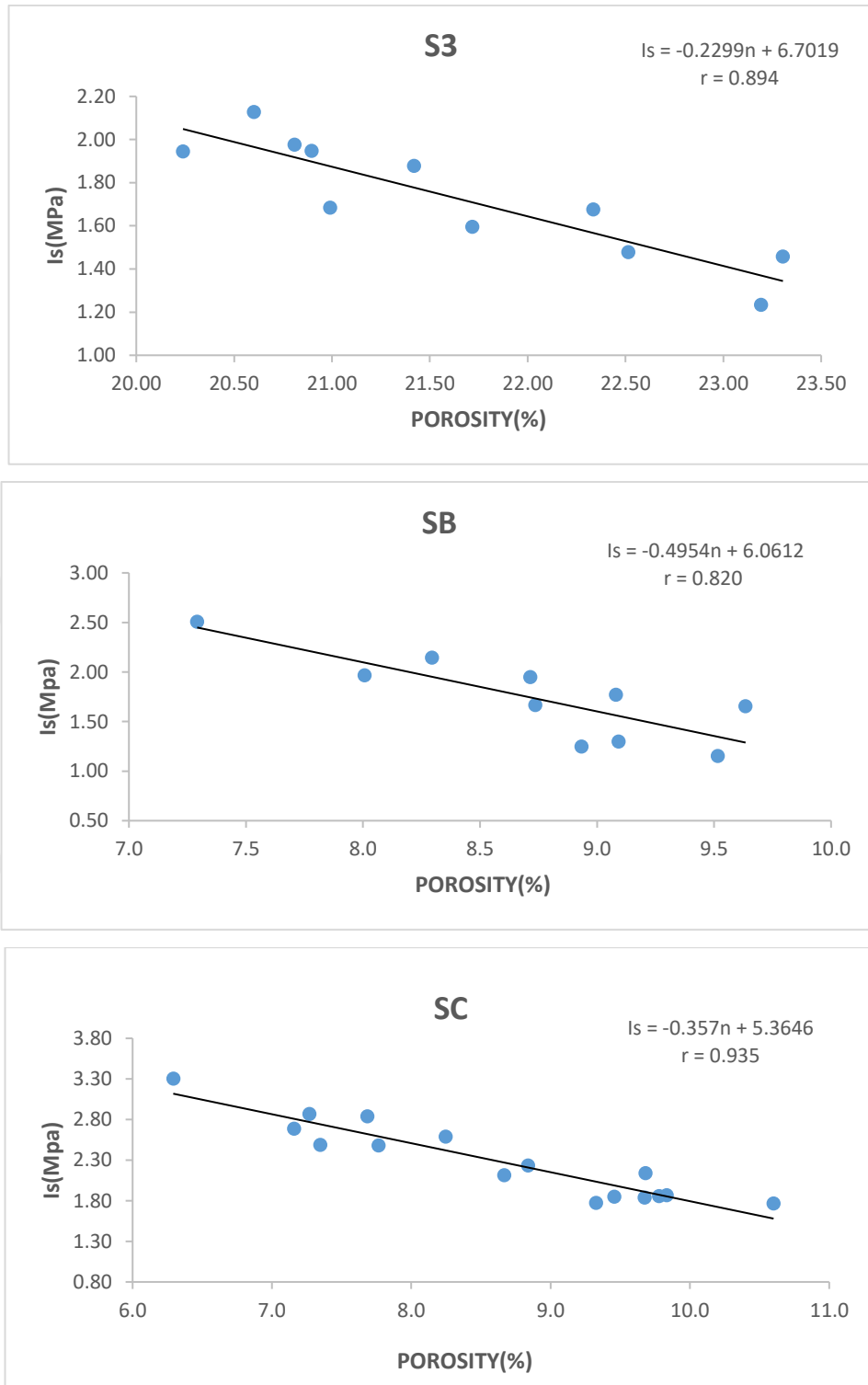
Figure 4.18 Relations between point load index and porosity (S3, SB and SC)
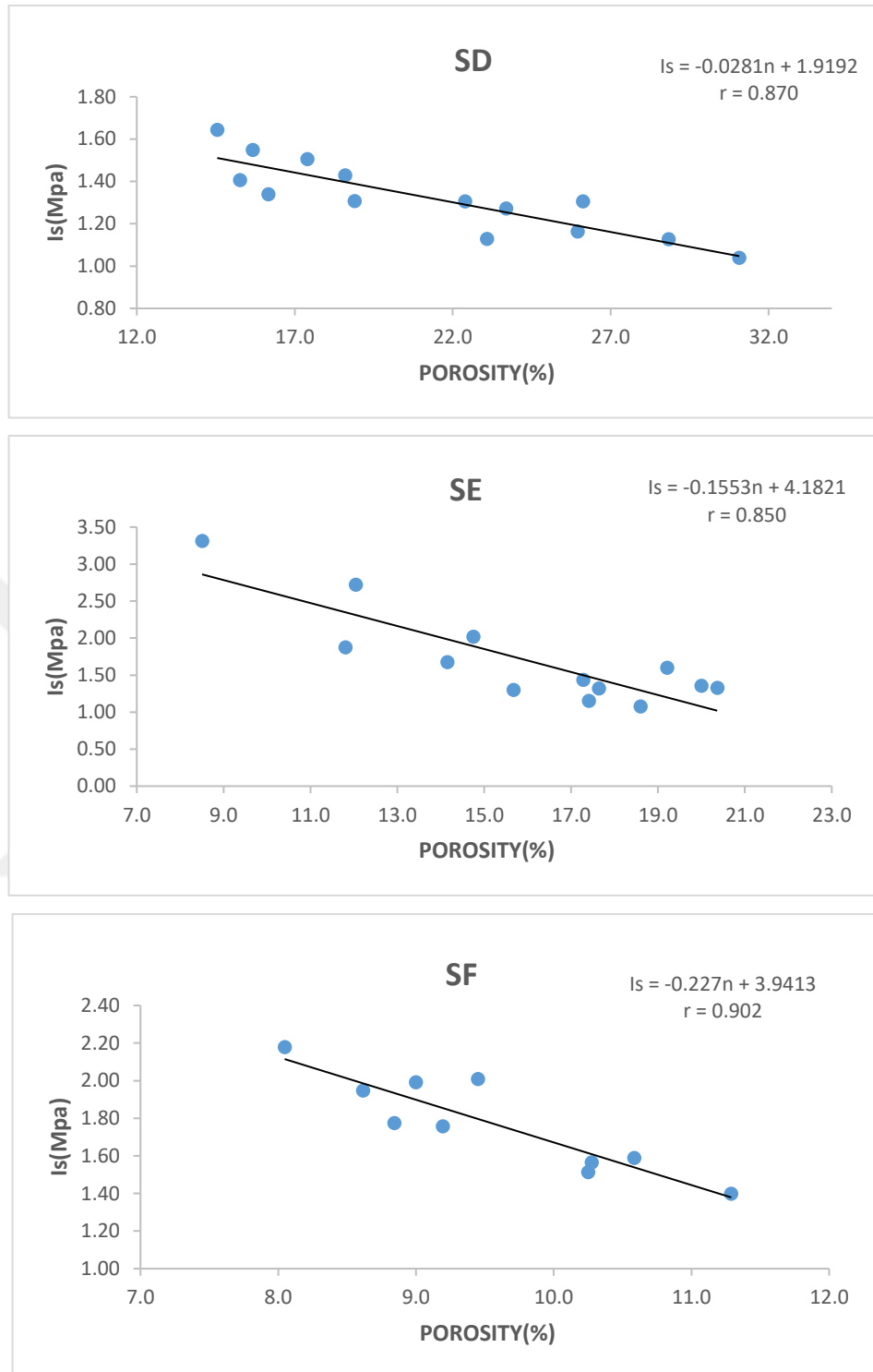
Figure 4.19 Relations between point load index and porosity (SD and SE and SF)
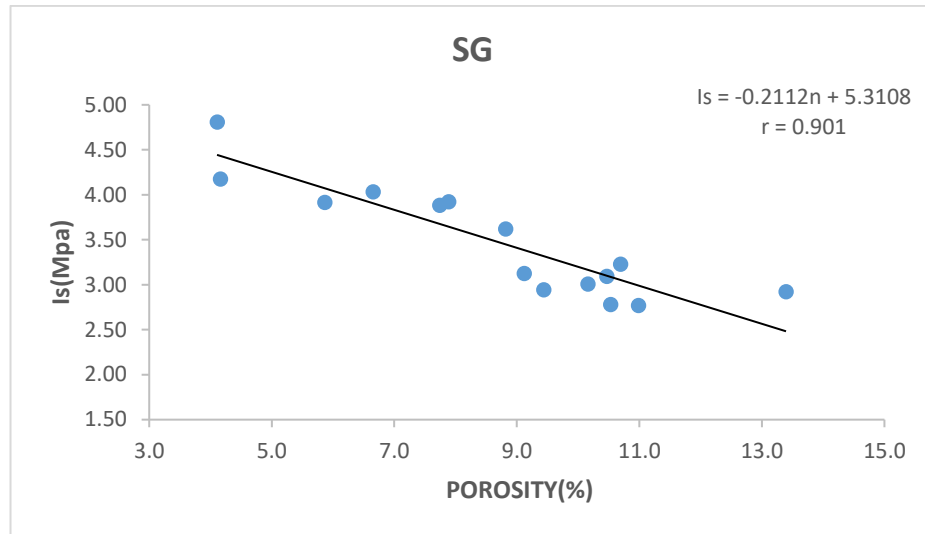
Figure 4.20 Relations between point load index and porosity (SG)

4.3.5 Splitting Tensile Strength (Brazilian Method)

Splitting Tensile Strength tests (Brazilian Indirect Tensile Strength tests) were conducted on 63 core disks. The core disks were made up of 29 specimens from S1, S2, S3 and 34 specimens from SC, SD, SE, SF and SG. These discs were prepared from rock samples obtained from the field and had an average thickness to diameter ratio of 0.5. The tests were conducted according to ASTM D3967-16.

An image of a specimen being loaded between two platens during Brazilian test is presented in Figure 4.21. An Image of some of the prepared specimens is presented in Figure 4.22. The data and results of the Brazilian test are presented in Table 4.8. The test was not conducted for SA and SB due to their weathered nature, which made sample preparation not to be possible.
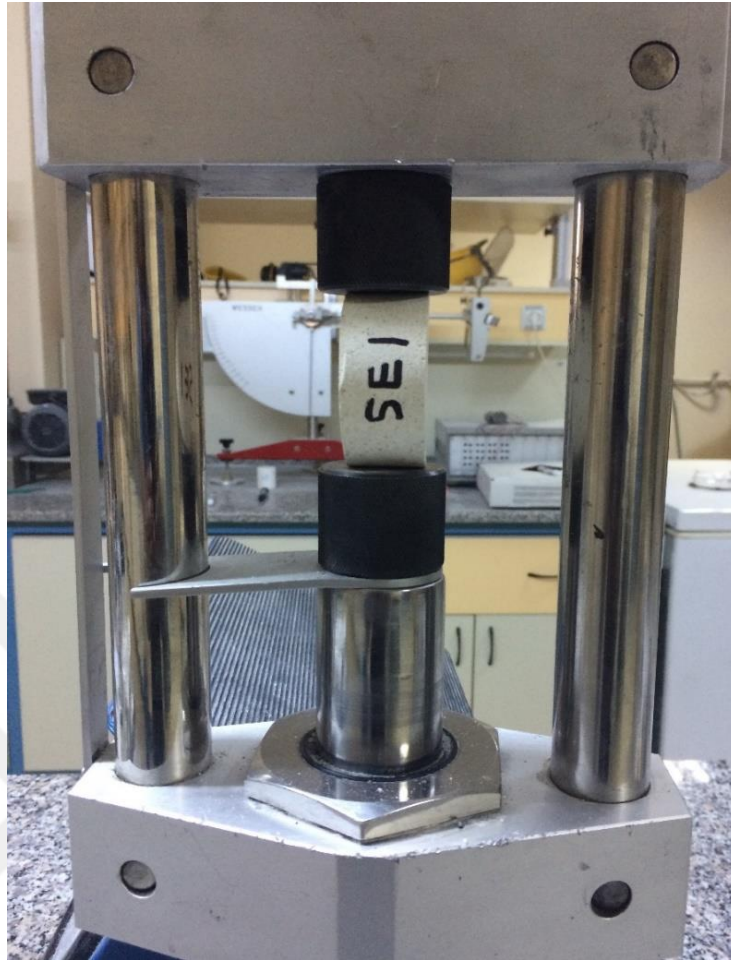
Figure 4.21 Specimen loaded between two platens during Brazilian test
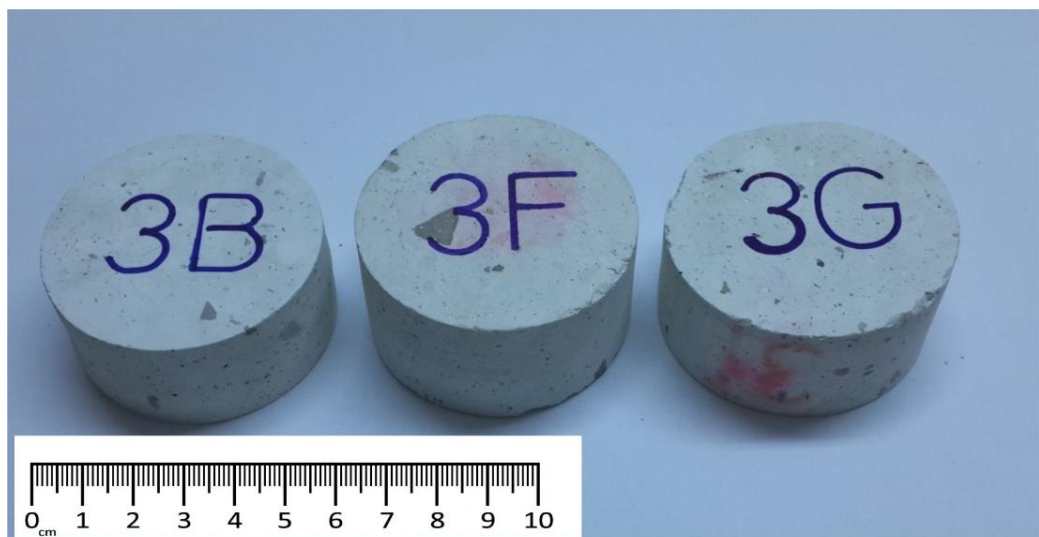
Figure 4.22 Brazilian test specimens

Table 4.8 Data and results of Brazilian indirect tensile strength test

Specimen No.	Diameter (D)	Thickness (T) mm	Failure Load (Kgf/mm^2)	σt (MPa)
1A	51.9	25.34	437.70	2.08
1B	52.0	25.42	239.90	1.13
1C	52.1	26.76	445.20	1.99
1D	52.2	24.39	361.40	1.77
1E	52.0	23.62	433.10	2.20
1F	52.1	25.17	218.60	1.04
1G	52.0	24.69	403.30	1.96
1H	52.0	23.86	816.20	4.10
1I	52.0	25.01	814.50	3.91
			X	2.24
			SD	1.08
2A	52.1	27.38	1327.50	5.80
2B	52.2	26.92	568.20	2.52
2C	52.0	23.63	323.40	1.64
2D	52.1	24.40	819.80	4.02
2E	51.9	23.72	1055.10	5.35
2F	51.8	24.72	810.80	3.95
2G	52.2	28.33	976.50	4.12
2H	52.3	26.21	296.60	1.35
2J	52.0	27.06	1613.20	7.15
2K	52.0	24.90	817.00	3.94
			X	3.98
			SD	1.82
3A	52.1	26.70	1129.90	5.07
3B	52.2	24.91	879.30	4.22
3C	52.0	23.32	203.40	1.05
3D	51.6	26.27	1129.90	5.20
3E	52.0	25.80	816.90	3.80
3F	52.3	27.39	842.90	3.67
3G	52.1	26.35	418.60	1.90
3H	52.2	26.91	968.50	4.30
3I	52.1	22.99	455.60	2.37
3K	52.0	22.01	651.80	3.55
			X	3.51
			SD	1.35
SC1	54.01	30.1	15.0	9.2
SC2	54.02	32.74	10.0	5.7
SC3	53.99	31.77	9.0	5.2
SC4	54	30	10.0	6.2
SC5	54.44	26.21	13.0	9.1

Table 4.8 Data and results of Brazilian indirect tensile strength test (cont.)

Specimen No.	Diameter (D)	Thickness (T) mm	Failure Load (Kgf/mm^2)	σt (MPa)
SC6	54.04	27.53	10.0	6.7
SC7	53.98	30.2	8.0	4.9
			X	6.7
			SD	1.8
SD1	53.8	32.28	5.0	2.9
SD2	53.77	31.05	4.0	2.4
SD3	54	30.8	5.0	3.0
SD4	53.44	33.27	6.0	3.4
SD5	54.01	32.9	5.0	2.8
			X	2.9
			SD	0.4
SE1	53.56	30.88	10.0	6.0
SE2	53.34	26.95	5.0	3.5
SE3	53.71	27.42	5.0	3.4
SE4	53.45	27.47	5.0	3.4
SE5	53.56	28	10.0	6.7
SE6	53.54	28.31	9.0	5.9
SE7	53.94	24.59	5.0	3.8
SE8	53.44	24.56	8.0	6.1
			X	4.8
			SD	1.5
SF1	53.52	28.33	16.0	10.6
SF2	53.96	28.5	9.0	5.9
SF3	53.69	29	5.5	3.5
SF4	53.7	30.75	13.0	7.9
SF5	54.04	29.9	8.0	5.0
SF6	53.67	28.9	9.0	5.8
SF7	53.69	27.95	7.0	4.7
			X	6.2
			SD	2.3
SG1	53.29	29.54	12.0	7.6
SG2	53.47	28.74	15.0	9.8
SG3	53.69	30.61	12.0	7.3
SG4	53.56	29.14	11.0	7.0
SG5	53.84	28.27	12.0	7.9
SG6	53.74	30.17	13.0	8.0
SG7	53.89	28.61	13.0	8.4
			X	8.0
			SD	0.9

4.3.6 Slake Durability Index Test

Slake Durability (Id) index provides useful information about the degree of weathering of rocks due to the effect of water. Weathering weakens rocks and reduces their strength (Wyllie & Mah, 2004). Rock weathering also puts slopes at risk of failure (Forti & Parise, 2008). Id tests are therefore important in characterizing weathering grade.

Id Index tests were conducted according to ASTM standard (D4644-16). The tests were conducted on ten samples from the ten different locations (S1, S2, S3, SA, SB, SC, SD, SE, SF, and SG) with different weathering grades (SW-HW). The samples were oven-dried prior to conducting the test. Ten (10) spherical rock samples of 40-60 g each, with a total mass of 450-550 g were prepared. For each cycle, a rotation speed of 20 rpm was used for 10 minutes. The samples were dried for 12 hours at 105 °C after each cycle. The tests were conducted for five cycles (Id_5) per each sample group. An image of the slake durability index testing device is presented in Figure 4.23.

Figure 4.23 Slake Durability Index test device

A summary of the test results is presented in Table 4.9. Detailed test data and computations are presented in Appendix 3. An image of differential weathering (contact between HW vitric tuff and SW lithic tuff) observed in the field is presented in Figure 4.24.

Table 4.9 Slake durability index values of the slopes

Slope	$Id_1\%$	$Id_2\%$	$Id_3\%$	$Id_4\%$	$Id_5\%$	Weathering degree
S1	91.20	85.82	80.14	75.13	69.16	HW
S2	97.42	95.24	94.04	92.46	90.67	SW
S3	93.59	88.07	82.74	77.04	71.16	HW
SA	91.65	83.66	75.61	67.57	60.34	HW
SB	95.97	91.12	87.02	82.63	79.92	MW
SC	98.58	97.40	96.19	94.99	93.73	SW
SD	91.06	81.15	72.09	64.02	54.55	HW
SE	95.97	92.50	89.13	85.52	81.90	MW
SF	97.11	94.29	91.32	88.55	86.04	MW
SG	98.41	96.73	94.67	93.05	91.49	SW
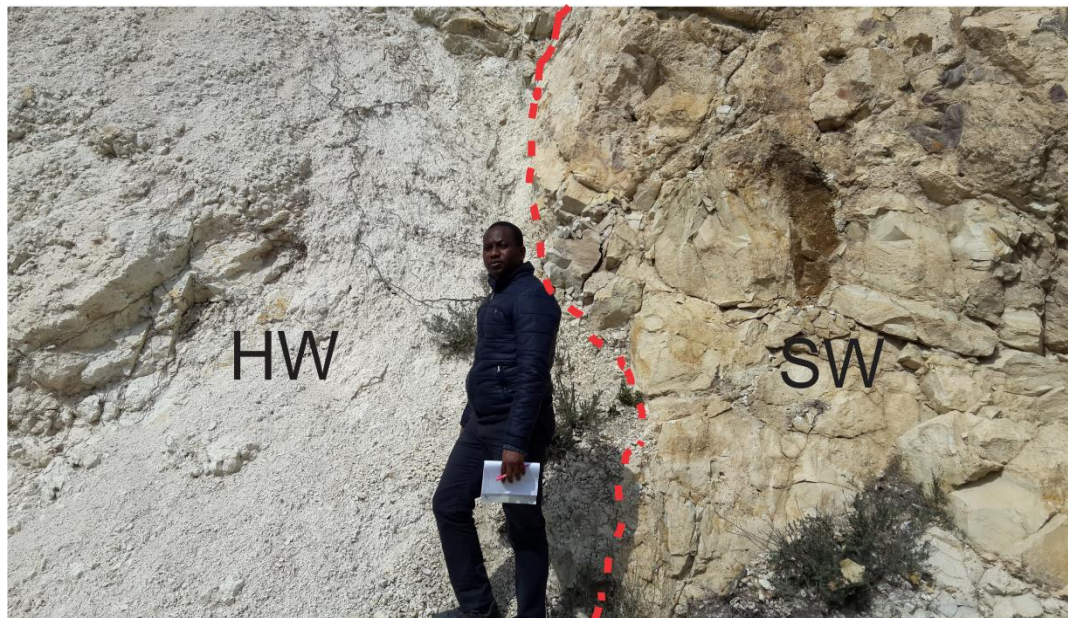
Figure 4.24 Differential weathering observed in the field

4.3.7 Direct Shear Strength Test

Direct shear strength tests were performed to determine the shear strength parameters of the discontinuities. The tests were performed according to ASTM D5607-16. The discontinuity surfaces were slightly altered with no infilling. Prior to conducting the test, the specimens were encapsulated using a gypsum based encapsulating compound. Proper alignment of the shear surfaces was ensured during sample preparation.

The specimens were mounted in the shear box (Figure 4.25) and an increasing external shear force was applied along the shear plane under a constant normal force. Normal loads of 0.36, 0.72 and 1.07 kN were used for the test. The normal and shear displacements were recorded. The test data sheets and results are presented in Appendix 4. Peak friction angles obtained were 33.52 ° and 29.59 °. There was no cohesion between the joints.

Figure 4.25 Specimen in shear box device

4.3.8 Triaxial Compressive Strength Test

Triaxial Compressive strength tests were conducted on 15 (SW-HW) Vitric Tuffs (VT) and Lithic Tuffs (LT). The tests were conducted according to ASTM D7012-14. The specimens had an average length to diameter ratio of 2:1. The specimens were placed in a flexible membrane within a confining chamber. The specimens were then subjected to lateral fluid pressure (3, 4, 6 and 9 MPa) and axial loading (Figure 4.26).

Figure 4.26 Triaxial compression test

An image of specimens at failure is presented in Figure 4.27. Test data and results are presented in Table 4.10. Mohr-coulomb parameters -friction angle (Φ) and cohesion values (C) - were calculated using the lateral stress (σ_3) and axial stress (σ_1) values. The parameters were calculated with the aid of Roclab software, by Rocscience (Figure 4.28). The calculated values are presented in Table 4.11.

Figure 4.27 Specimens at failure

Table 4.10 Triaxial compressive strength test data and results

Specimen number	Length (cm)	Diameter (cm)	Area (cm²)	σ_3 MPa	Vertical load (Kgf)	σ_1 MPa	Description	Weathering degree
1NB	11.7	5.3	62.5	3.0	11450	18.3	VT	HW
1NA	11.5	5.4	61.7	6.0	13740	22.3	VT	HW
1ND	11.5	5.3	61.0	9.0	15860	26.0	VT	HW
2NB	11.4	5.4	61.2	3.0	14210	23.2	LT	SW
2NH	11.1	5.3	59.0	6.0	16300	27.6	LT	SW
2NA	11.1	5.3	59.2	9.0	19400	32.8	LT	SW
SF4	11.3	5.4	60.7	4.0	11230	18.5	VT	MW
SF5	11.1	5.3	59.4	6.0	14360	24.2	VT	MW
SF6	11.2	5.3	60.0	9.0	16760	28.0	VT	MW
SE2	11.2	5.3	59.8	3.0	14000	23.4	VT	MW
SE1	11.2	5.3	59.8	6.0	14910	25.0	VT	MW
SE3	11.9	5.3	63.7	9.0	17500	27.5	VT	MW
3NF	11.7	5.3	61.9	3.0	12030	19.4	VT	HW
3ND	11.3	5.3	60.1	6.0	13720	22.8	VT	HW
3NE	11.1	5.4	59.7	9.0	16030	26.9	VT	HW

Table 4.11 Friction angle (Φ) and cohesion values (C)

Specimen	Friction angle (Φ)degrees	Cohesion (C)MPa
1A,1B, 1C	29.76	1.071
2NB, 2NH, 2NA	32.46	1.81
SF4,SF5, SF6	32	1.43
SE1,SE2, SE3	30.96	0.83
3NE,3NF, 3ND	31.86	1.3
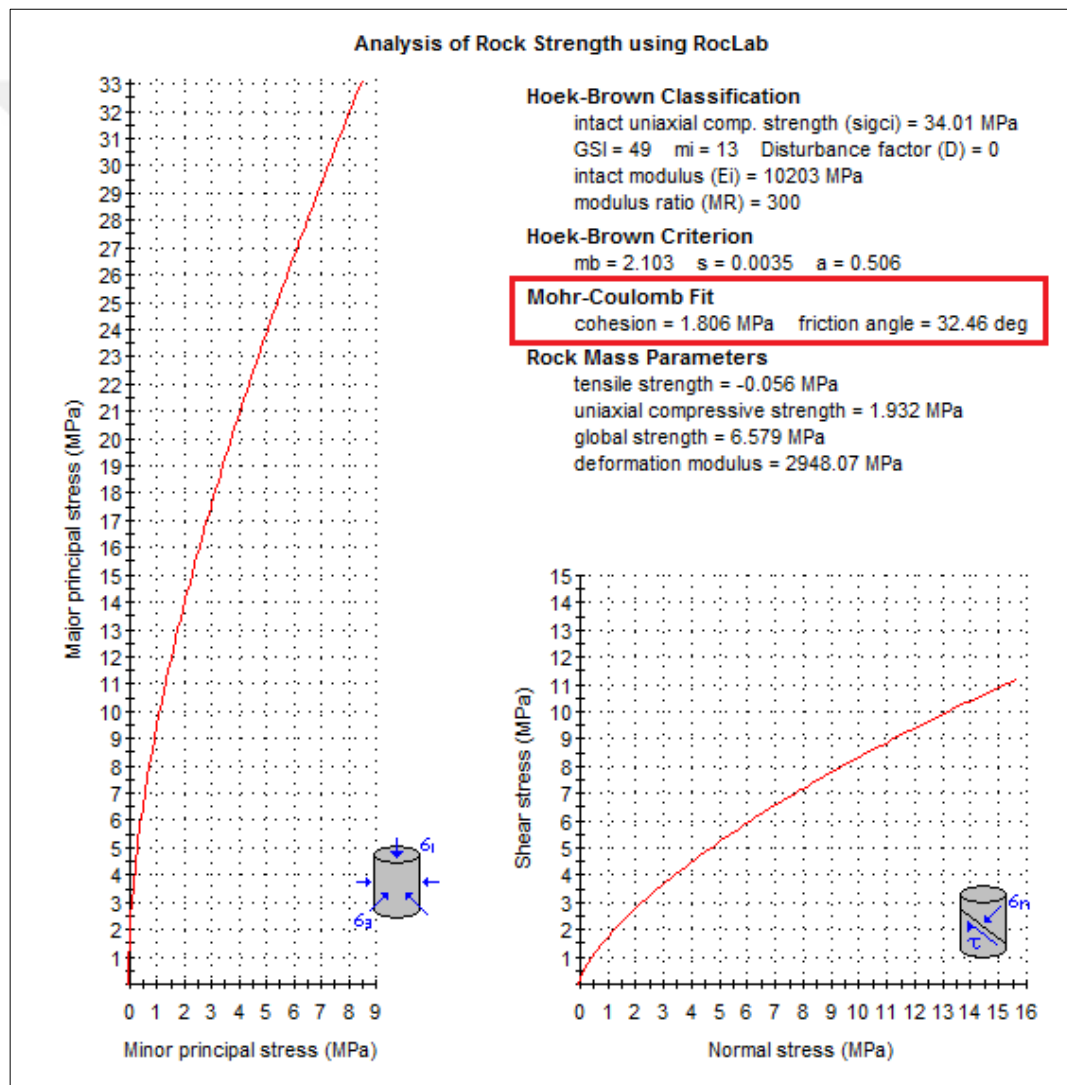
Figure 4.28 Shear strength parameter calculation with Roclab

4.4 Discontinuity Data Collection (Scanline Mapping of discontinuities)

Discontinuity data is important in making engineering geological assessments of a rock mass or rock slope. Scanline mapping (Figure 4.29) is a common and effective method of discontinuity data collection on rock slopes. It involves stretching a measuring tape horizontally across the face of the slope and making detailed recording of all discontinuities that intersect the scanline.
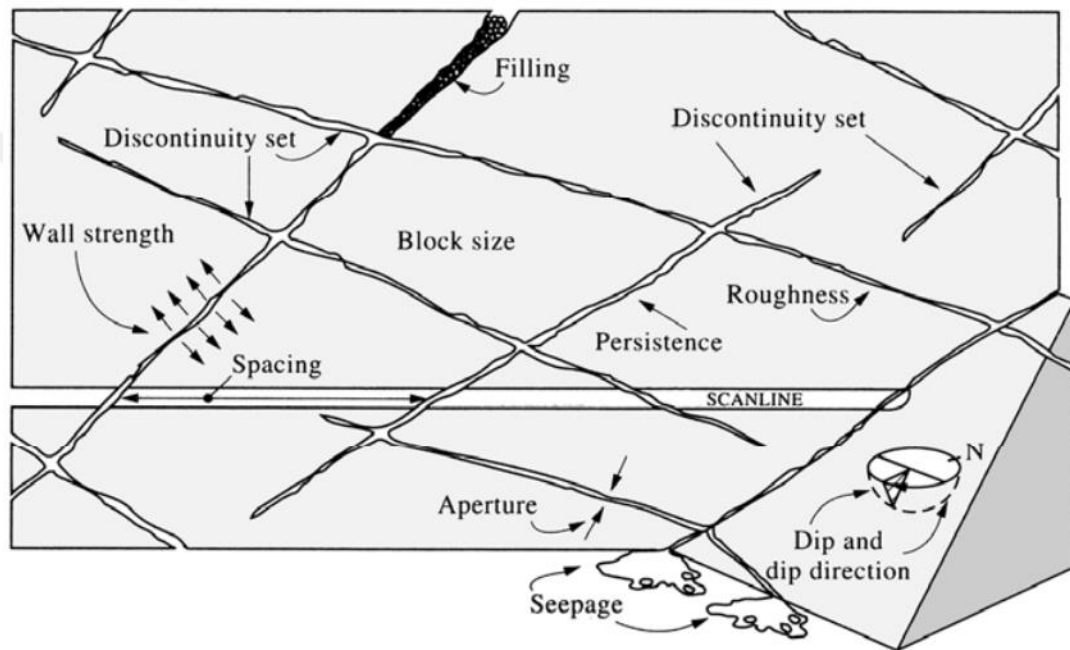
Figure 4.29 Scanline mapping (after Hudson and Harrison, 1997)

Scanline mapping was performed on the Bagarasi-Foca (Izmir) State Highway slopes. Discontinuity data obtained include dip and dip direction, spacing, persistence, filling and roughness. Scanline mapping was not done for slopes with high degree of weathering or presence of multiple closely spaced discontinuities. Images of the scanline mapping are presented in Figure 4.30. Scanline mapping data is presented in Appendix 5.
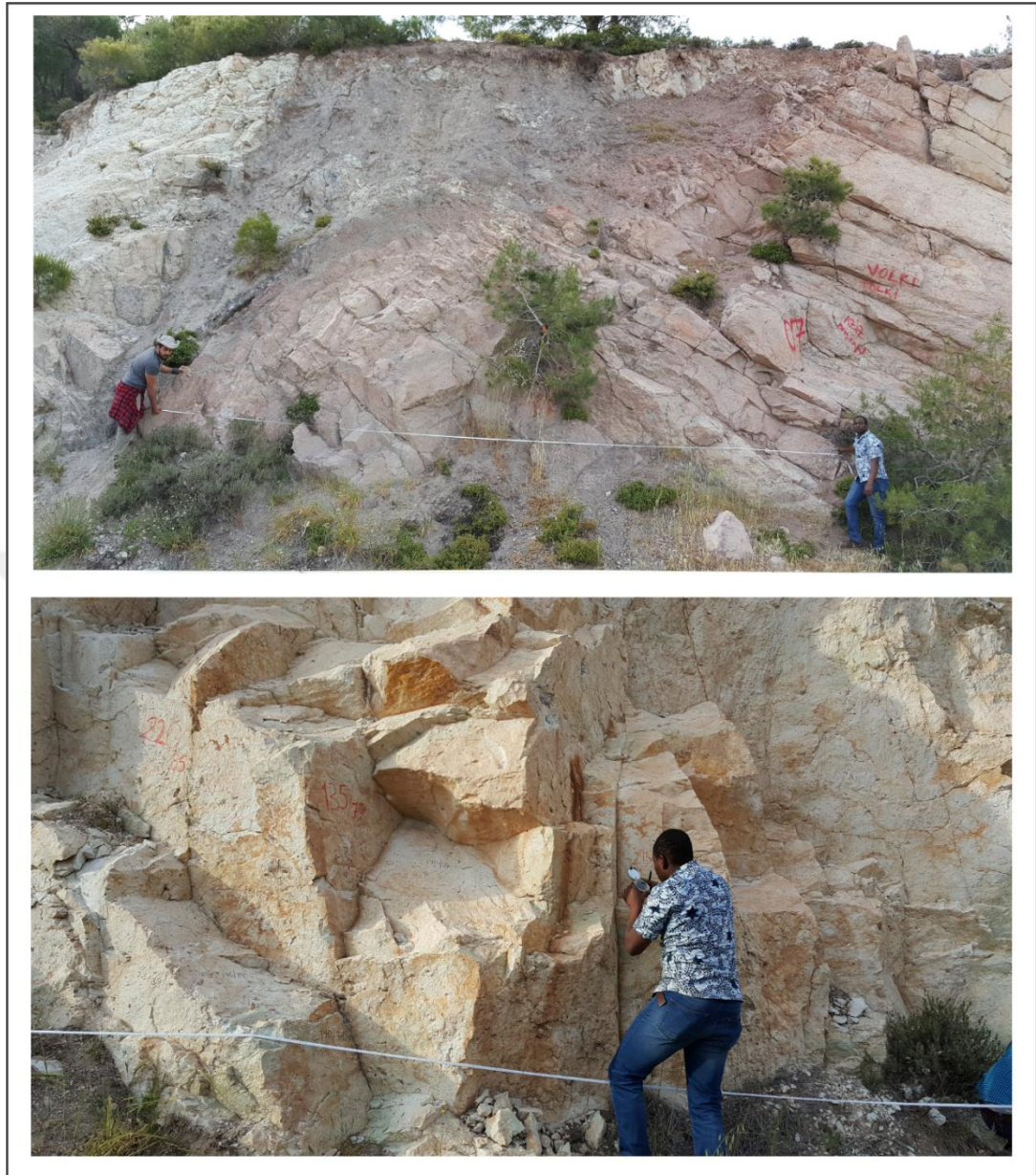
Figure 4.30 Images from the scanline mapping

4.5 Slope Stability-Kinematic Analysis

Kinematic analysis involves analyzing discontinuity orientation data to identify potential modes of slope failure such as planar, wedge and toppling failures. Discontinuity data obtained from the field was plotted on stereonets (lower hemisphere projection) using Dips 5.1. Discontinuity sets were then defined based on Schmidt concentrations of the poles plotted. The sets were defined by clicking on 'Sets' and selecting 'Add Set Window' in the drop down menu.

Kinematic analyses was conducted on the plotted discontinuities for toppling, wedge and plane failures. The mean orientation data (dip direction and dip amount) of the slopes and their discontinuity sets are presented in Table 4.12. Failure zones are highlighted in the stereoplots.

Table 4.12 Mean orientation data of slopes and discontinuity sets

Slope	Main orientation of Discontinuity sets (Dip direction/dip angle)	Discontinuity Set Orientations With highest Schmidt concentrations (>10%).	Slope Orientation (Dip direction/dip angle).	Number of Poles
S2	316/47, 234/78, 34/80	316/47, 234/78	138/62	57
S3	122/78, 11/74, 221/87, 173/83, 191/39, 147/59	221/87, 191/39	217/75	84
SC	225/21, 139/63, 261/63, 104/28	225/21, 139/63	138/74	49
SD	156/58, 255/81, 201/59, 9/60, 273/60, 220/75	156/58, 255/81,	152/74	48
SE	153/64, 242/43, 73/40	153/64, 242/43, 73/40	153/72	45
SF	166/74, 168/41, 131/26, 79/29	166/74, 131/26	145/75	40
SG	107/77, 4/72, 128/61, 136/43	107/77, 4/72	165/73	59

4.5.1 Plane Failure Analysis

Plane failure analysis was performed on the stereonet using the slope orientation, 'Daylight envelope' and 'friction cone'. The slope orientation was plotted on the stereonet by clicking on 'Select' and choosing 'Add Plane' in the draw down menu. In the dialog box that opens, the dip and dip direction values of the slope were entered and the 'daylight envelope' check box was ticked to add the 'daylight envelope' to the slope. The friction cone was added to the stereonet by clicking on 'Tools' and selecting 'Add cone' in the draw down menu. The friction angle was then entered together with the 'trend' and 'plunge' values in the dialog box that opens.

The new zone whose boundary is defined by the daylight envelope and the friction cone is the planar failure region. Stereoplots of the planar failure analyses are presented in Figure 4.31 and 4.32.
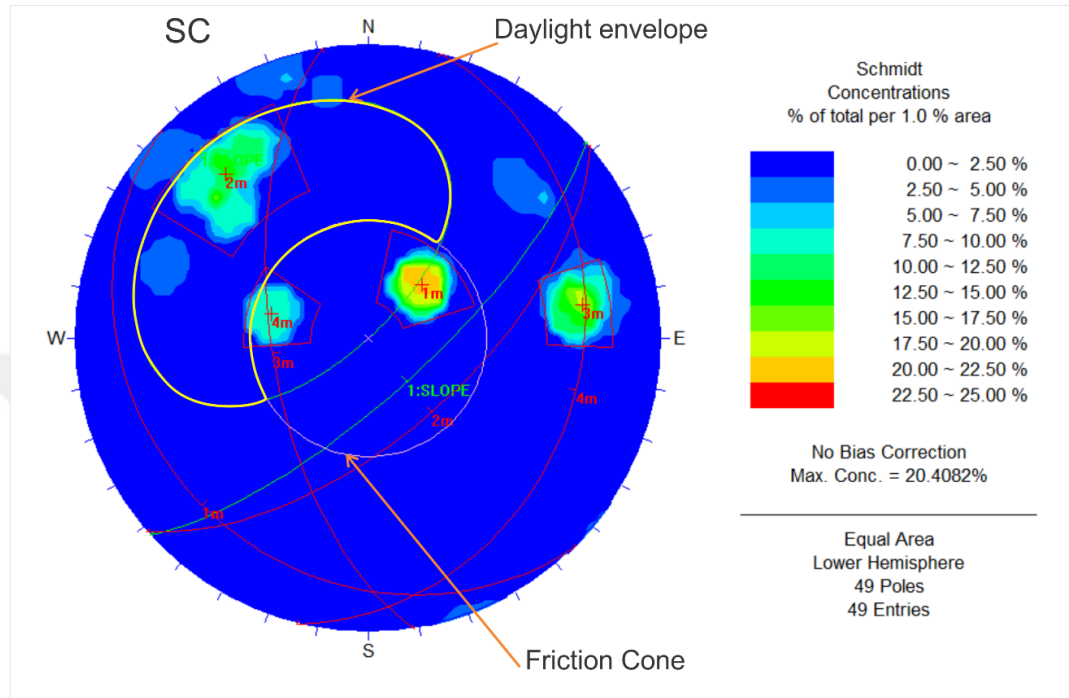
Figure 4.31 Plane failure analysis (SC)
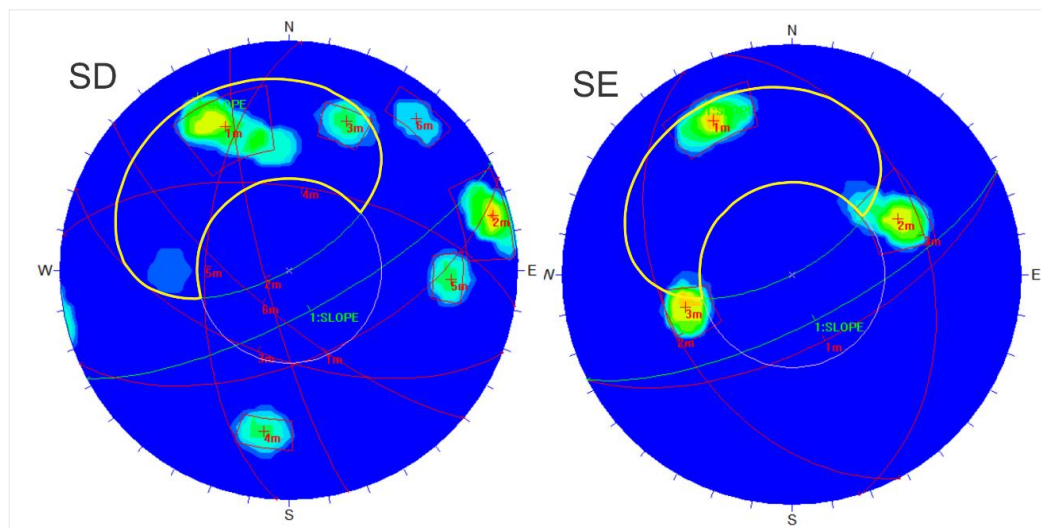
Figure 4.32 Plane failure analyses (SD and SE)

4.5.2 Toppling Failure Analysis

Toppling failure was performed on the stereonet using the slope orientation, 'Slip Limit' and a '60-degree variability cone'. The 'slip limit' was added in a similar way as the slope orientation by choosing 'Select'and then 'Add Plane'. The dip direction of the slip limit is always the same as that of the slope. The dip amount of the slip limit is obtained by subtracting the friction angle from the dip amount of the slope. The variability cone was added to the stereonet by selecting 'Tools' and subsequently 'Add Cone'. The 60-degree variability cone suggested by Goodman (1980) placed kinematic bounds on the stereoplot with respect to the dip direction of the slope face. Stereoplots of the toppling failure analyses are presented in Figure 4.33.
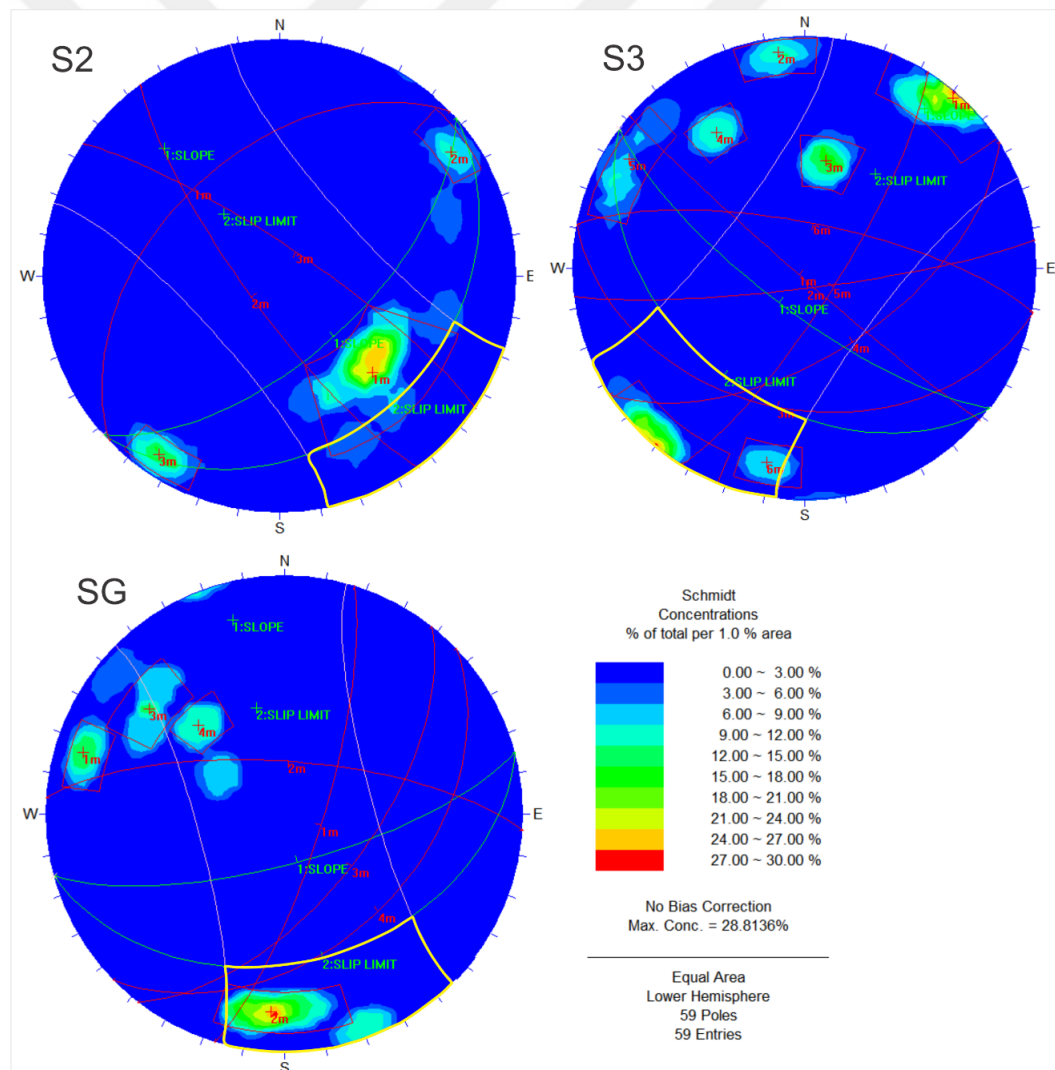
Figure 4.33 Toppling failure analyses (S2, S3 and SG)

4.5.3 Wedge Failure Analysis

Wedge failure analysis was performed on the stereonet using the slope orientation and 'friction cone'. The friction cone and slope orientation were added to the stereonet as described in the plane failure analysis but in this case the friction angle is measured from the equator. Poles whose planes intersect in the wedge failure region stand a potential risk of failure. Stereoplots of the wedge failure analyses are presented in Figure 4.34.
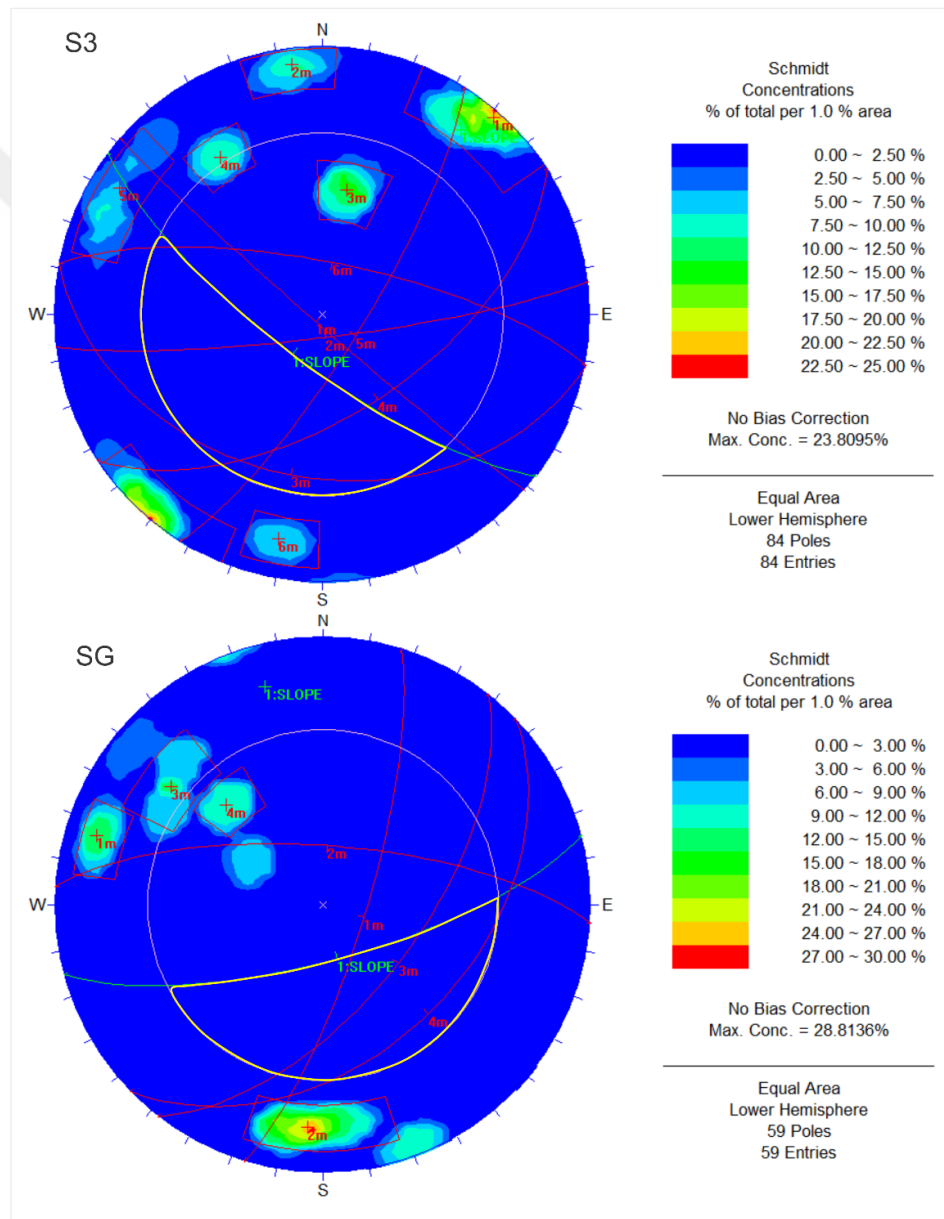
Figure 4.34 Wedge failure analyses (S3 and SG)

4.6 Slope Stability-Finite Element Analysis

Finite element analyses (FEM) were conducted on the slopes using Phase^2 software. Prior to conducting the analyses, accurate models of the slopes incorporating the slope geometry (slope angle and height) were drawn on graph sheets. The models were then drawn using Phase^2 software. Strength Reduction Factors (SRF) were computed for the various slopes.

Definition of rock mass conditions is important in choosing an analytical method. The rock masses in the study area were generally heavily jointed. For this reason, Finite element analysis was chosen for conducting the slope stability analysis. Various rock mass conditions and appropriate analytical methods to use are presented in Table 4.13.

Table 4.13 Rock mass conditions and appropriate analytical methods

Rock Mass Condition	Rock Material	
	Elastic	**Elasto-plastic**
Massive rock	Boundary Element	Finite element Finite Difference
Sparsely jointed rock	Boundary Element Finite Element	Finite element Finite Difference
Closely jointed rock	Distinct Element	Distinct Element
Heavily jointed rock		Finite element Finite Difference

To evaluate the stability of a slope using FEM-Shear Strength Reduction Analysis, first, 'analysis' is selected on the menu bar (Figure 4.35). In the dialog box that opens, 'project settings' is selected and the various units, analyses methods and strength reduction settings are done.
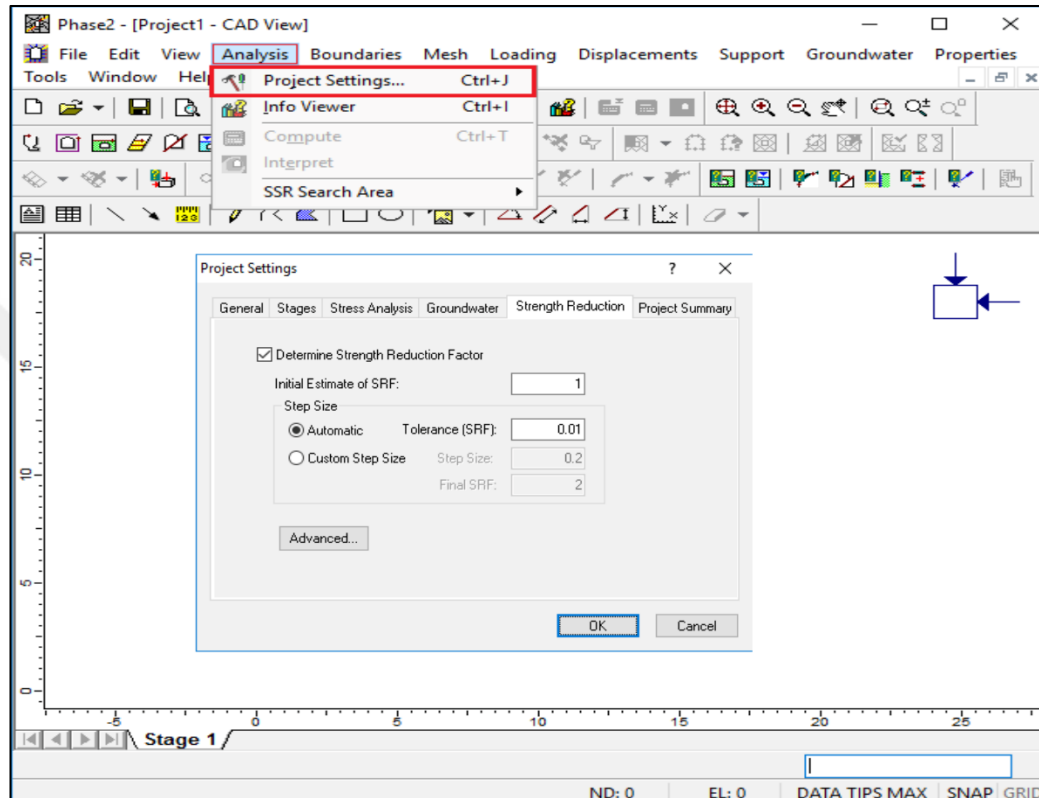
Figure 4.35 Project settings in Phase[2]

After 'project settings' is completed, the geometry of the slope is drawn. To do this, 'Boundaries' is selected on the menu bar after which 'Add External' is chosen. The coordinates of the slope geometry are now entered one pair at a time at the lower right section of the application (Figure 4.36).
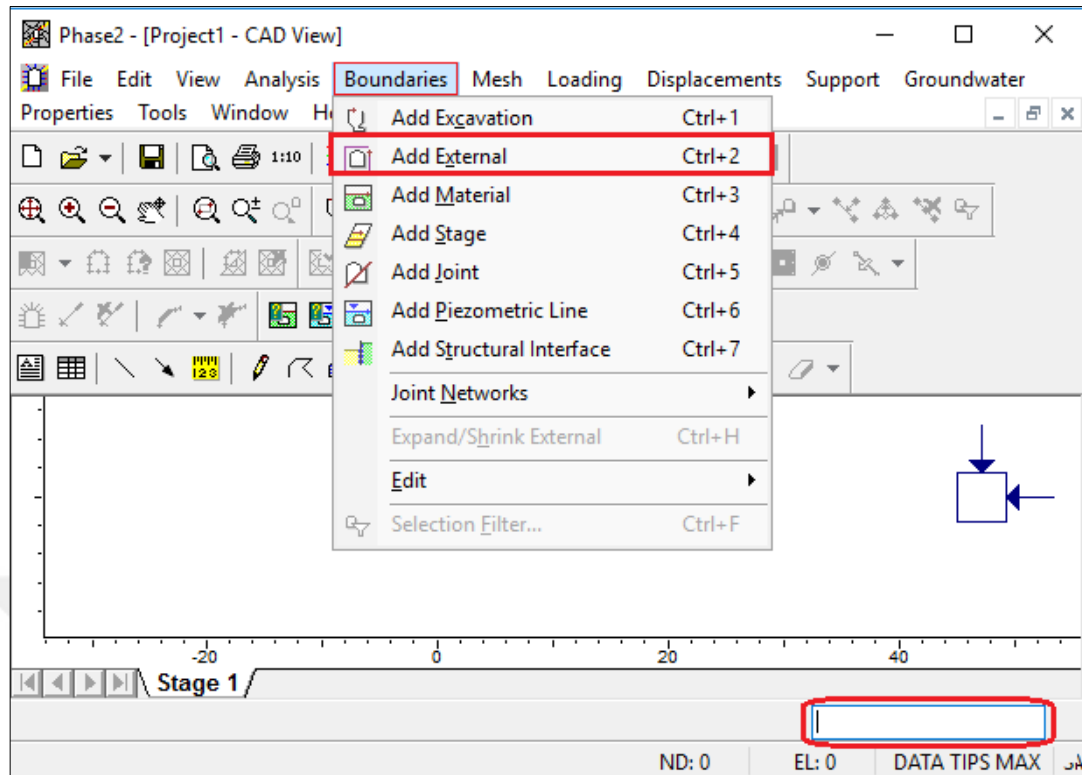
Figure 4.36 Drawing slope geometry in Phase^2

By using the commands 'Boundaries-Joint Networks-Add Joint Network', joints are added to the model (Figure 4.37). Joint properties such as dip/dip direction, spacing and joint end conditions are entered in the 'Edit Joint Network' menu. Next, 'mesh and discretization' settings are done using 'Mesh-Mesh Setup' commands (Figure 4.38). 'Discretize' and then 'Mesh' are selected to complete the process. If needed, Piezometric lines are added to the model using 'Boundaries-Add Piezometric Line'.
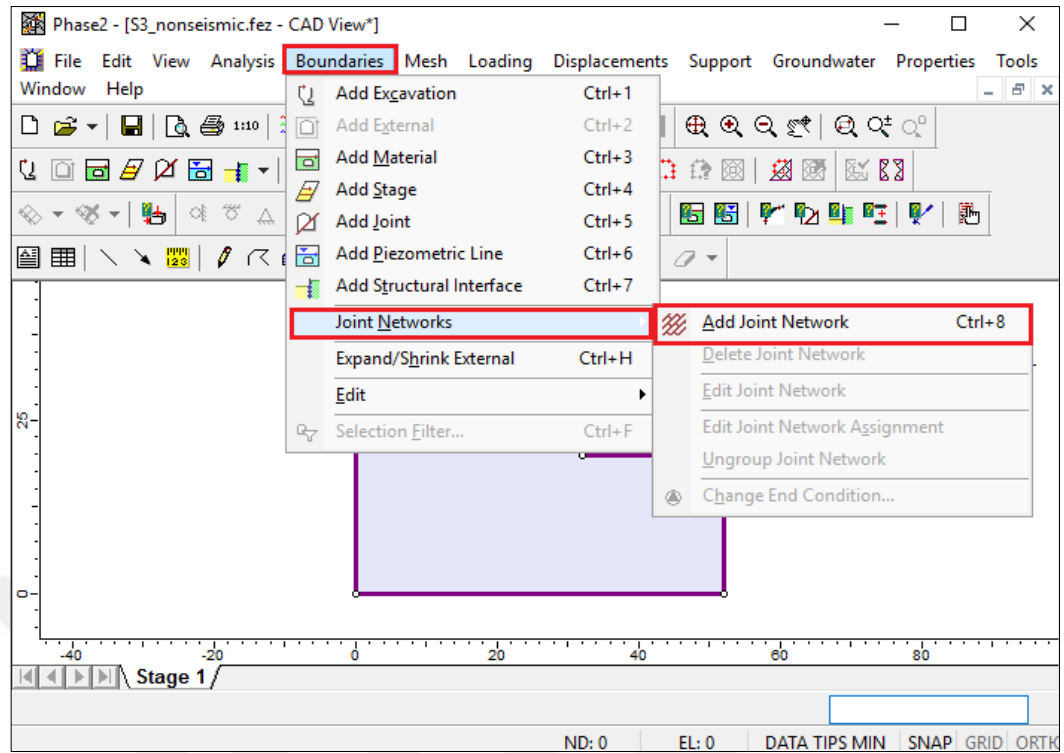
Figure 4.37 Joint network addition in Phase^2
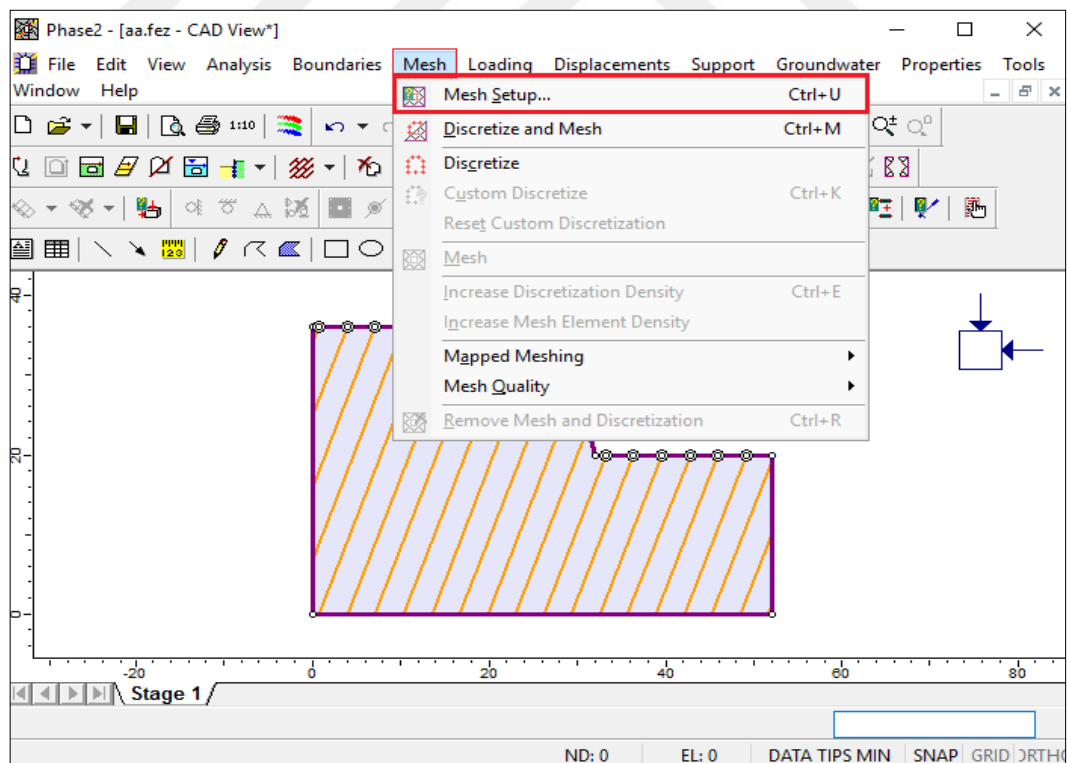
Figure 4.38 Mesh and discretization setup in Phase^2

Movement is permitted along the face of the slope by clicking on the boundary of the slope model and selecting 'Free Restraint'. The top right and top left apexes of the slope are restrained from moving by selecting 'Restrain XY'. The 'Loading' menu is used to specify the type of field stress and seismic loading to be considered. 'Gravity' was used as field stress type in this study and 'use actual ground surface' was selected.

Rock material properties and strength parameters (cohesion and friction angle) are specified using 'Properties-Define Materials' (Figure 4.39). Failure criterion is also specified. Mohr-Coulomb criterion was used in this study. Joint properties are specified using 'Properties-Define joints'. After material and joint properties have been specified, the SRF is computed by selecting 'Analysis-Compute'. The computed critical SRF is accessed by selecting 'Analysis-Interpret'.
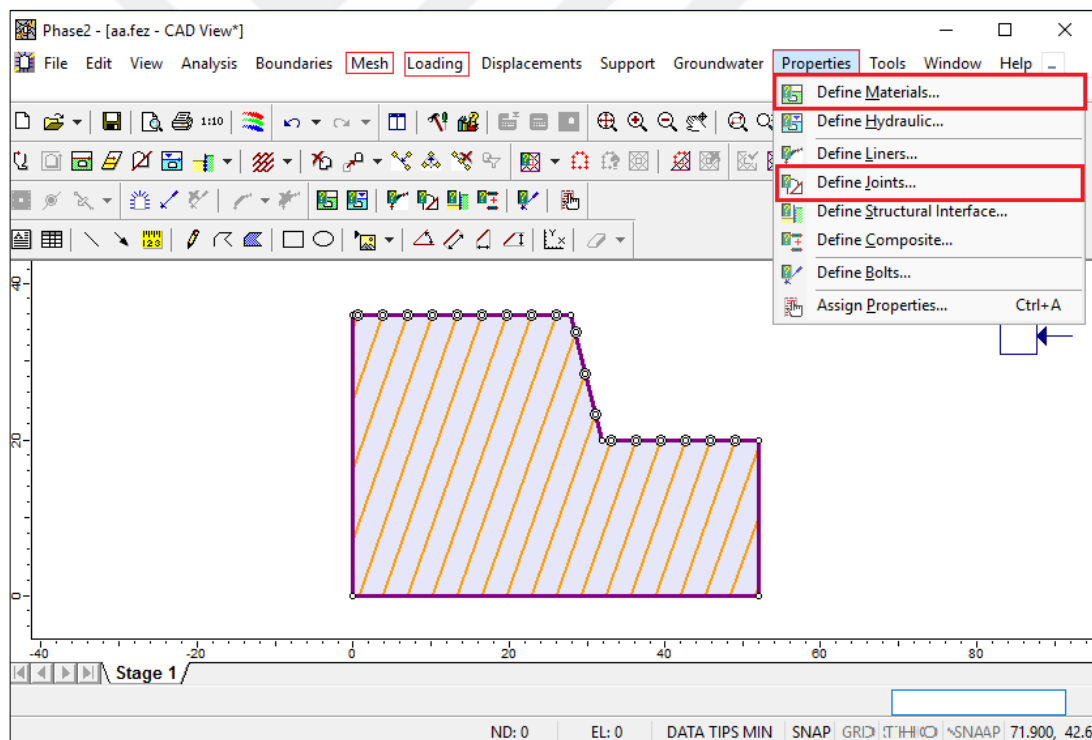
Figure 4.39 Defining rock materials and joint properties in Phase[2]

The stability of the slopes were analysed under seismic (positive to right direction of seismic waves) and non-seismic conditions and under saturated and dry situations. The results of the analyses are presented below.

Slope 3 (S3)
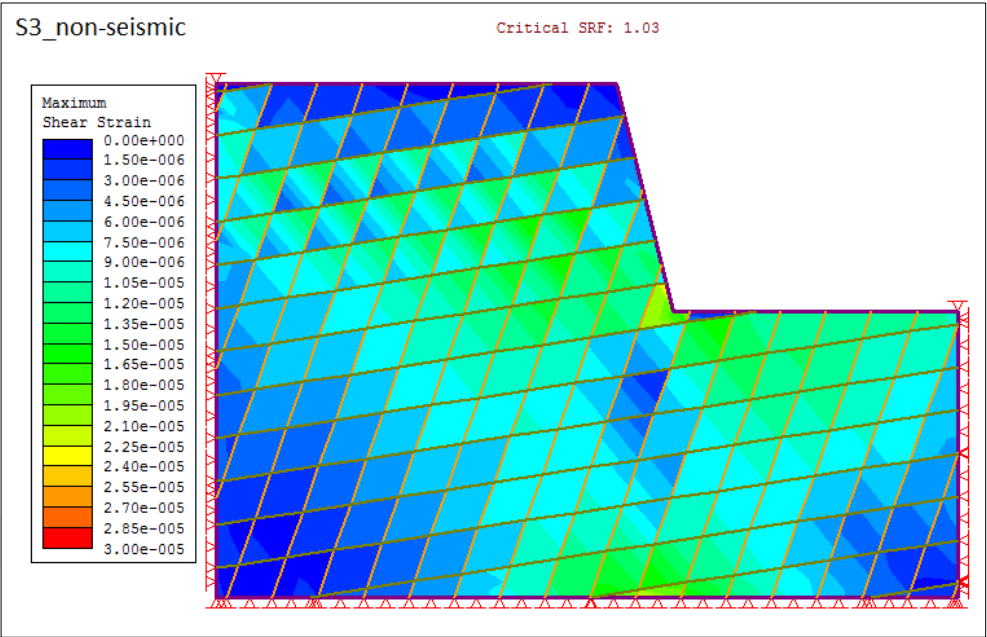
Figure 4.40 SRF-dry condition (S3)
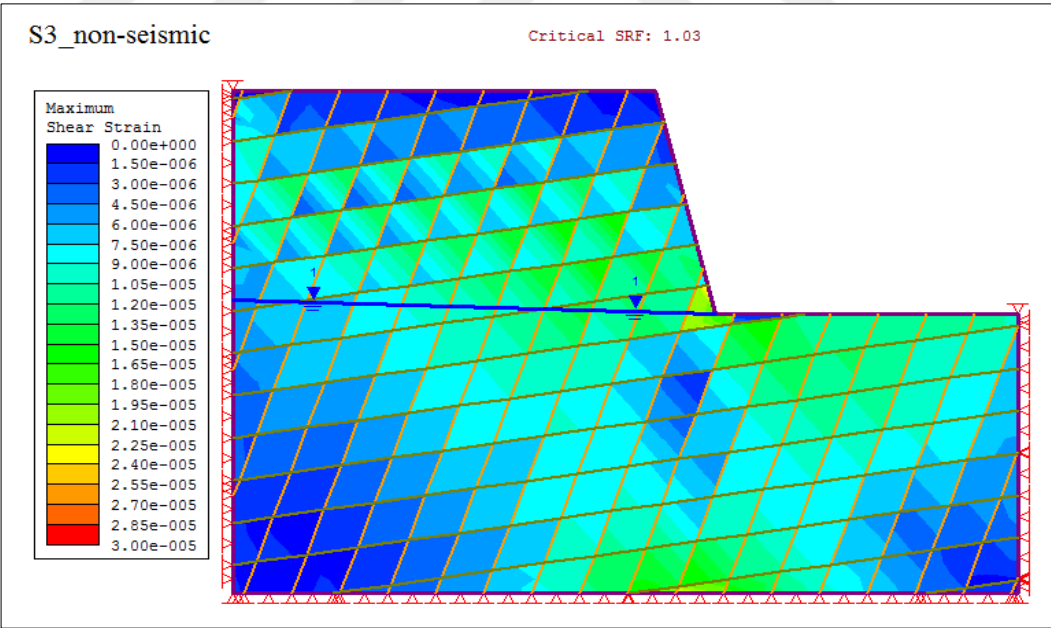
Figure 4.41 SRF-Piezometric line at toe of slope (S3)
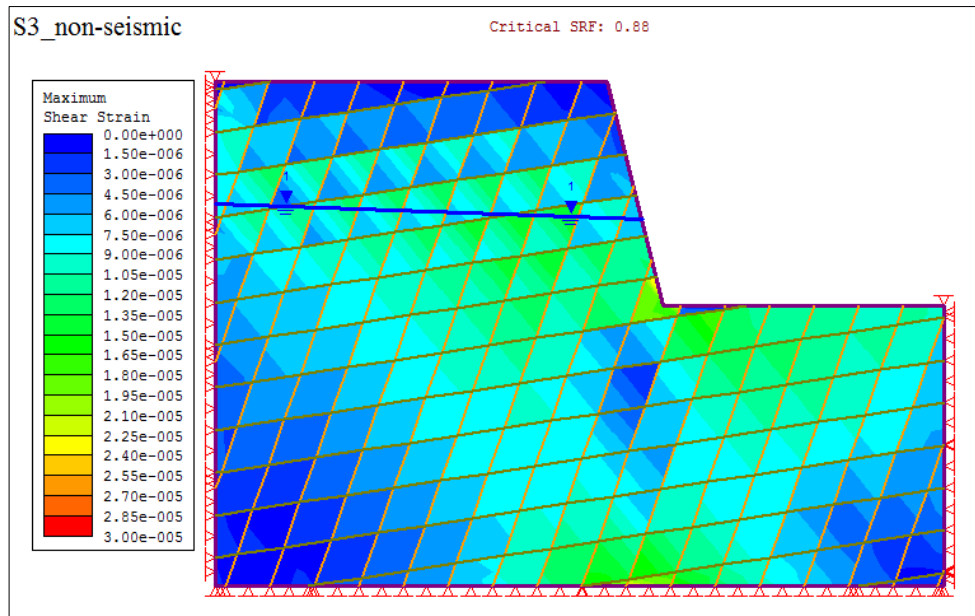
Figure 4.42 SRF-Piezometric line at middle of slope (S3)

Table 4.14 Slope stability analysis -S3

Slope S3- Height:15.8 m	
Condition (Non-seismic)	**SRF**
Dry	1.03
Piezometric line at toe of slope	1.03
Piezometric line at middle of slope	0.88
Piezometric line at top of slope	0.79
Condition (Seismic)- Dry	**SRF**
0.1g	0.91
0.2g	0.76

Slope C (SC)
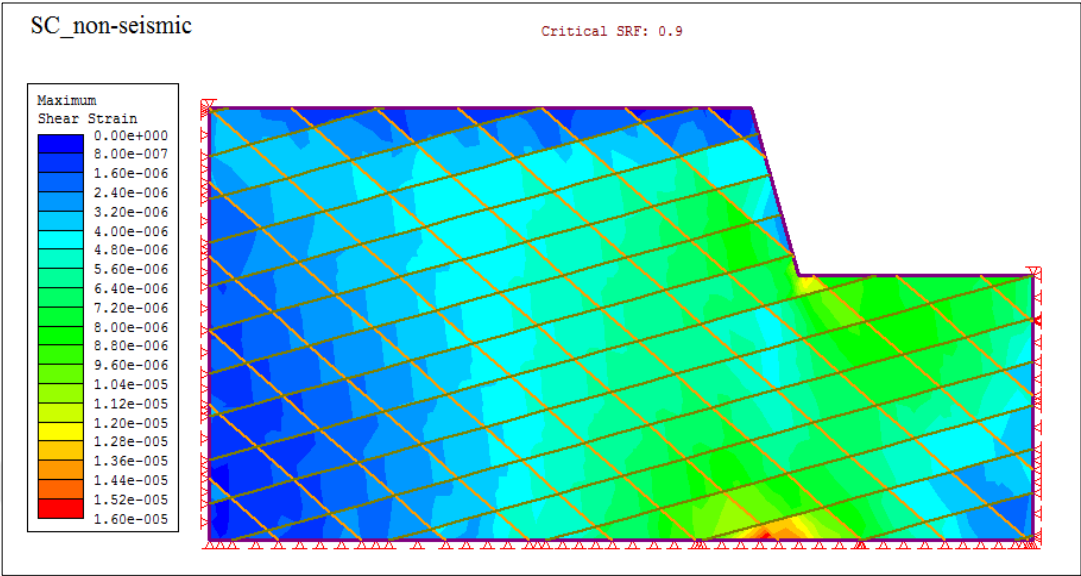
Figure 4.43 SRF-dry condition (SC)
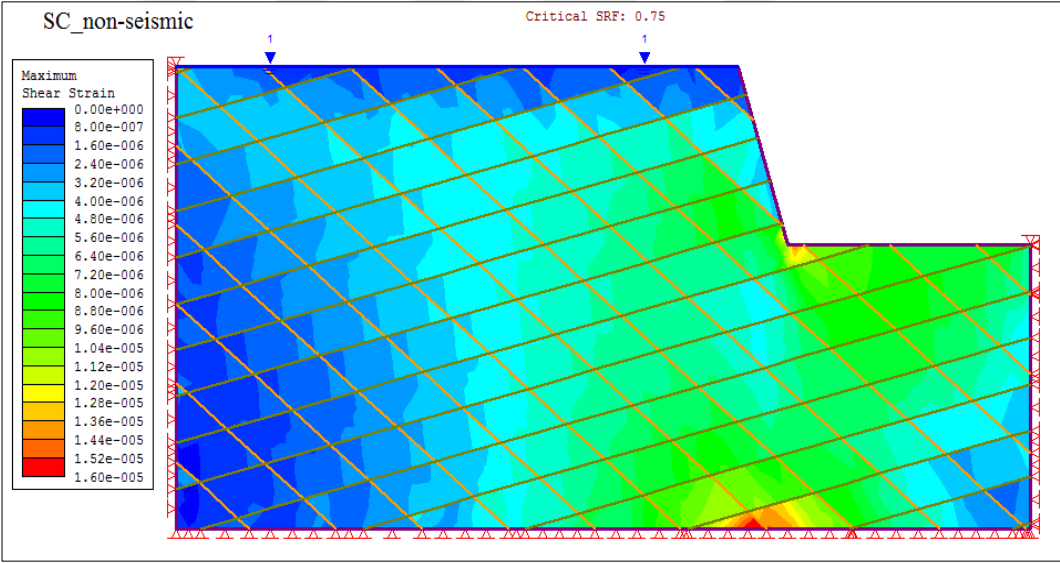
Figure 4.44 SRF-Piezometric line at top of slope (SC)

Table 4.15 Slope stability analysis -SC

Slope SC- Height:12 m	
Condition (Non-seismic)	**SRF**
Dry	0.9
Piezometric line at toe of slope	0.9
Piezometric line at middle of slope	0.84
Piezometric line at top of slope	0.75
Condition (Seismic)- Dry	**SRF**
0.1g	0.74
0.2g	0.61

Slope D (SD)
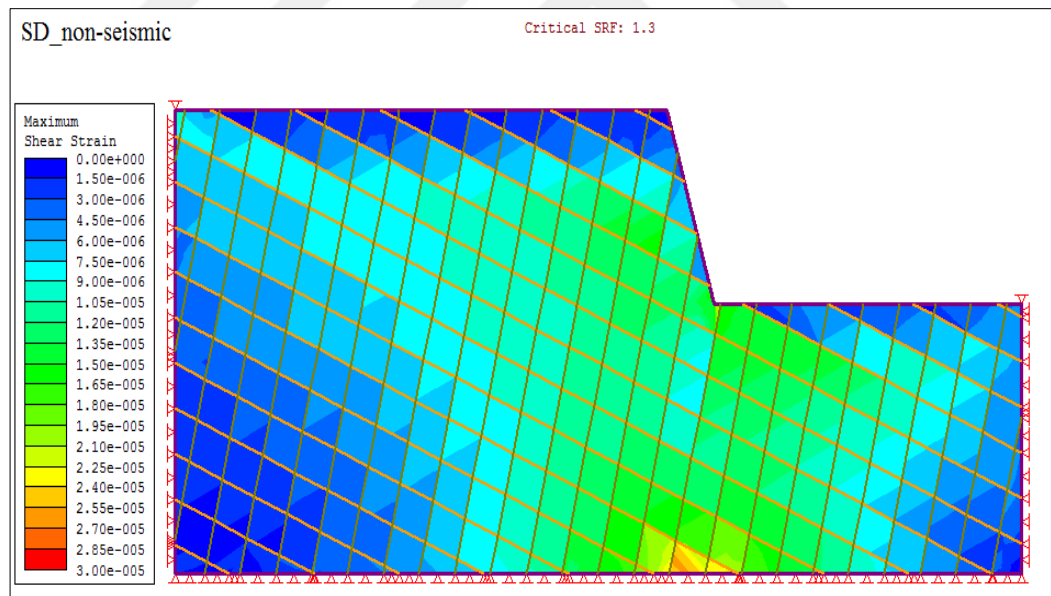
Figure 4.45 SRF-dry condition (SD)
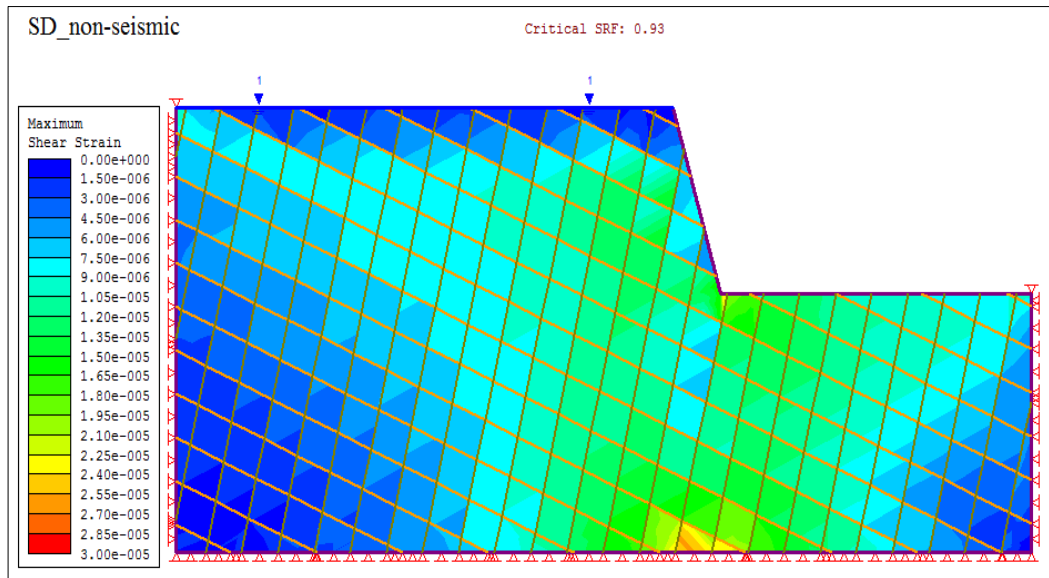
Figure 4.46 SRF-Piezometric line at top of slope (SD)

Table 4.16 Slope stability analysis -SD

Slope SD- Height:9.3 m	
Condition (Non-seismic)	**SRF**
Dry	1.3
Piezometric line at toe of slope	1.3
Piezometric line at middle of slope	1.2
Piezometric line at top of slope	0.93
Condition (Seismic)- Dry	**SRF**
0.1g	1.01
0.2g	0.82

Slope E (SE)
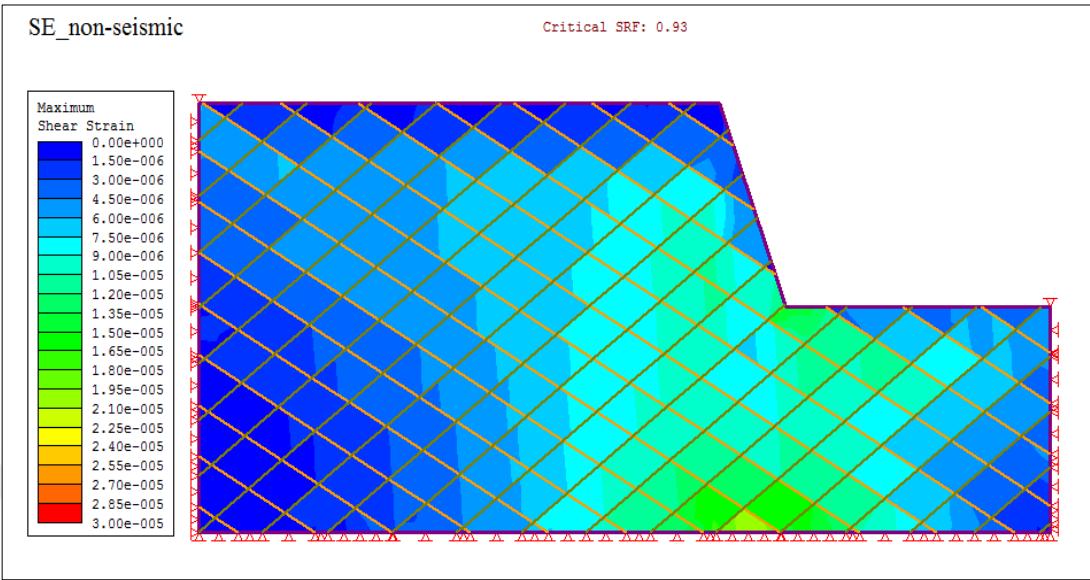
Figure 4.47 SRF-dry condition (SE)
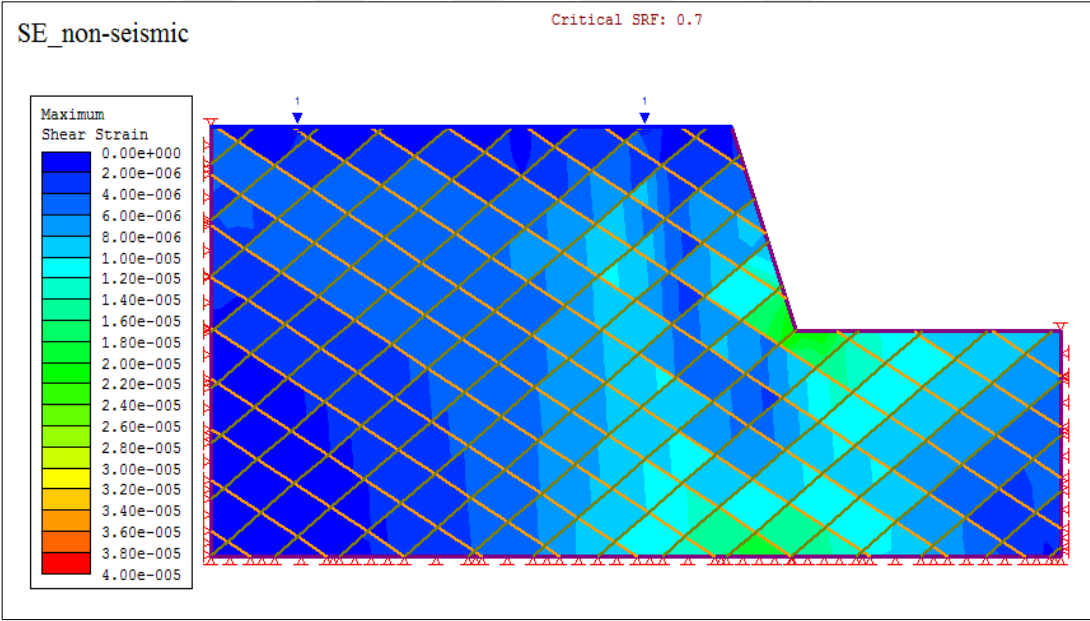
Figure 4.48 SRF-Piezometric line at top of slope (SE)

Table 4.17 Slope stability analysis -SE

Slope SE- Height:9.5 m	
Condition (Non-seismic)	**SRF**
Dry	0.93
Piezometric line at toe of slope	0.93
Piezometric line at middle of slope	0.84
Piezometric line at top of slope	0.7
Condition (Seismic)- Dry	**SRF**
0.1g	0.76
0.2g	0.62

Slope F (SF)
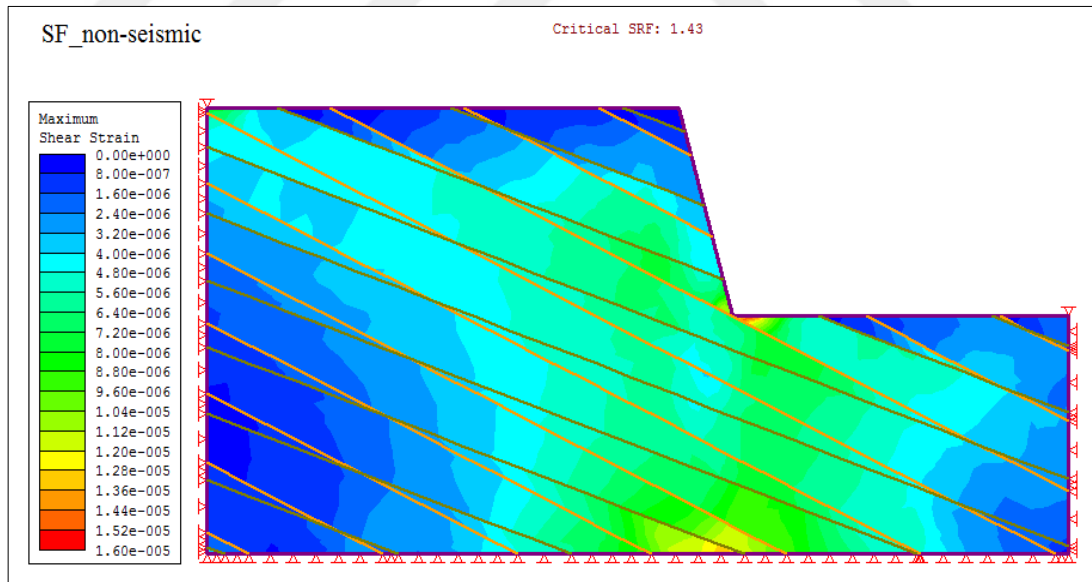
Figure 4.49 SRF-dry condition (SF)

110
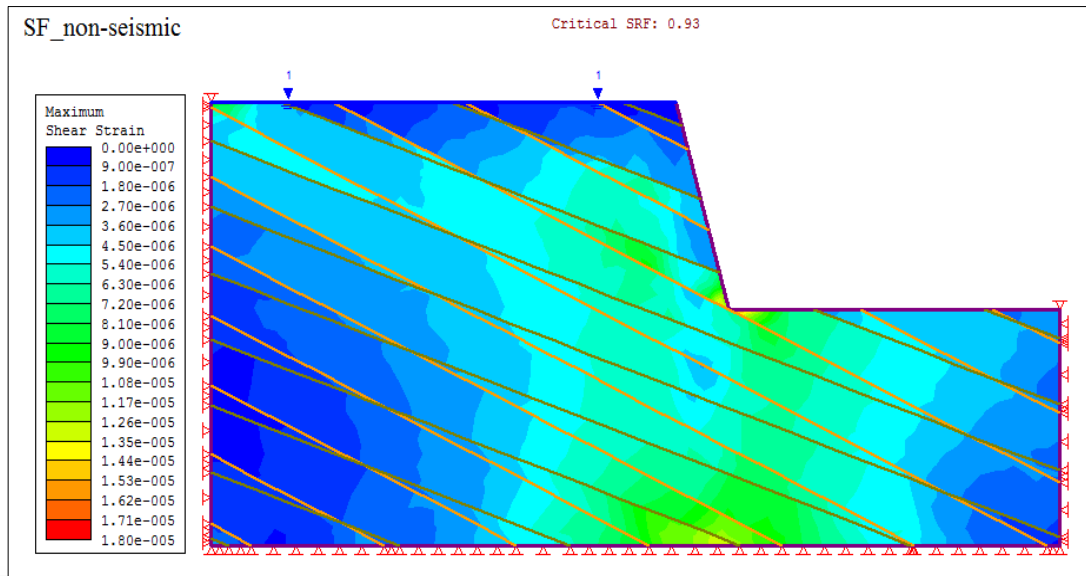
Figure 4.50 SRF-Piezometric line at top of slope (SF)

Table 4.18 Slope stability analysis -SF

Slope SF- Height:8.4 m	
Condition (Non-seismic)	**SRF**
Dry	1.43
Piezometric line at toe of slope	1.43
Piezometric line at middle of slope	1.28
Piezometric line at top of slope	0.93
Condition (Seismic)- Dry	**SRF**
0.1g	1.14
0.2g	0.93

Slope G (SG)
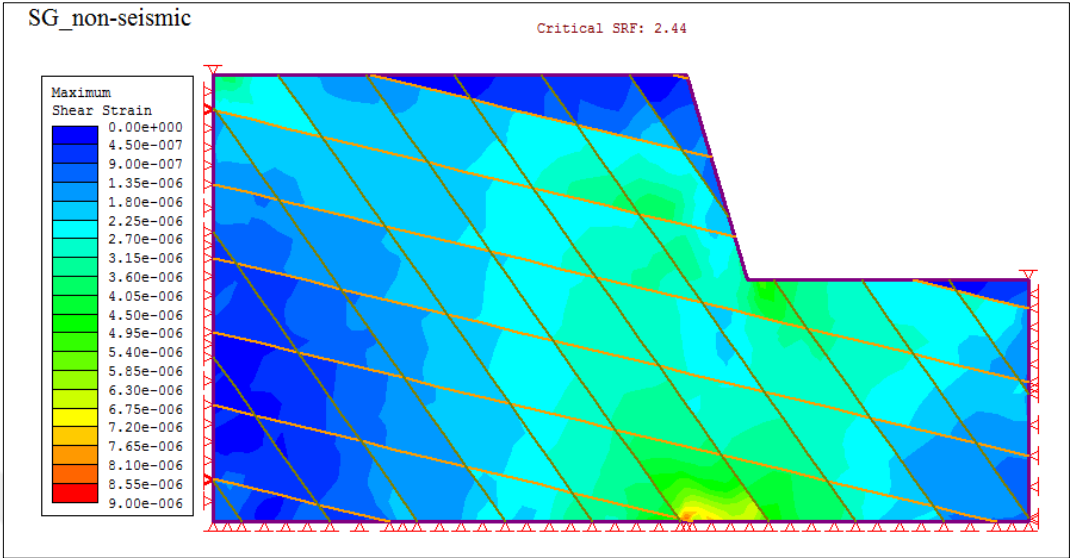
Figure 4.51 SRF-dry condition (SG)
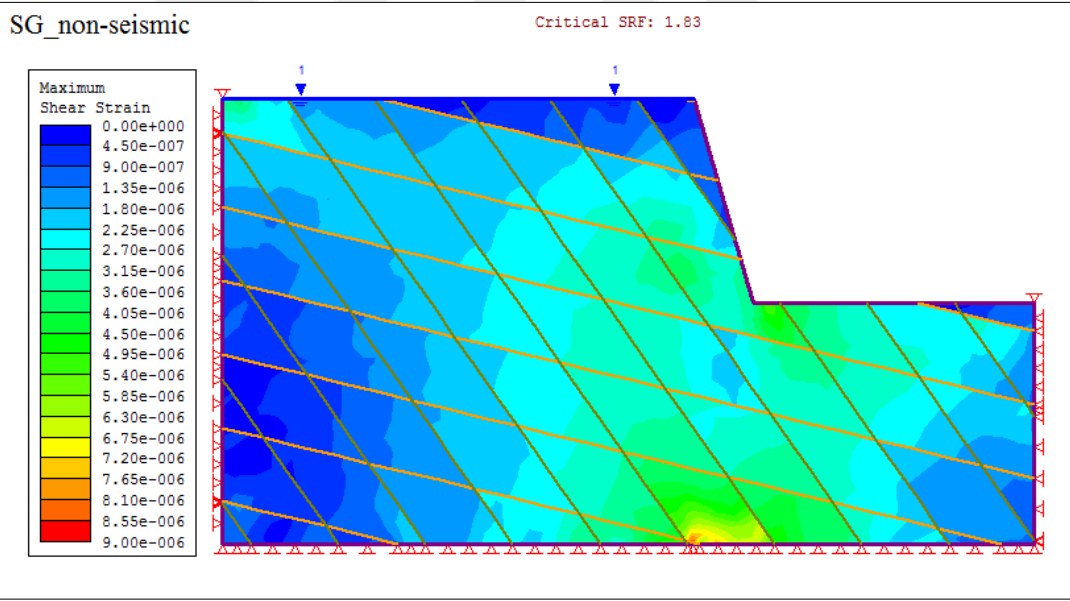
Figure 4.52 SRF-Piezometric line at top of slope (SG)

Table 4.19 Slope stability analysis -SG

Slope SG- Height:7.3 m	
Condition (Non-seismic)	**SRF**
Dry	2.44
Piezometric line at toe of slope	2.44
Piezometric line at middle of slope	2.00
Piezometric line at top of slope	1.83
Condition (Seismic)- Dry	**SRF**
0.1g	2.05
0.2g	1.80

CHAPTER FIVE

DISCUSSIONS, CONCLUSIONS AND RECOMMENDATIONS

5.1 Discussions

5.1.1 Mineralogy, Geochemistry and Physico-Mechanical Properties

Dry unit weight values ranged between 1.63-1.78 g/cm^3 in the highly weathered (HW) tuffs, 1.87-2.09 g/cm^3 in the moderately weathered (MW) tuffs and 2.05-2.08 g/cm^3 in the slightly weathered (SW) tuffs. Saturated unit weight values ranged between 1.94-1.99 g/cm^3 in the highly weathered tuffs, 2.03-2.18 g/cm^3 in the moderately weathered tuffs and 2.13-2.16 g/cm^3 in the slightly weathered tuffs. The rhyolite unit had dry and saturated unit weights of 2.27 g/cm^3 and 2.35 g/cm^3 respectively.

Porosity values ranged between 17.39-30.85 % in the highly weathered tuffs, 9.54-15.73 % in the moderately weathered tuffs and 8.41-8.49 % in the slightly weathered tuffs. The rhyolite unit had a porosity of 8.80 %. Inverse linear relations were established between porosity and unit weight (both saturated and dry). As porosity values increase, unit weight values decrease.

P-wave velocity (Vp) values recorded for dry and saturated specimens were between 2777.1-3385.7 m/s and 2606.2—3080.2 m/s respectively in the highly weathered tuffs, 3204.7-3497.9 m/s and 2874.6 m/s-3614.7 m/s respectively in the moderately weathered tuffs and 4189.7-4268.7 m/s and 3801.5- 4086.4 m/s in the slightly weathered tuffs. Vp values of the rhyolite unit were 4328.3 m/s and 4239.4 m/s for dry and saturated specimens respectively. Inverse linear relations were established between Vp and porosity. Vp values of the lithic tuffs were observed to be higher than the Vp values of the vitric tuffs. This observation could be due to the fact that vitric tuffs easily weather to form clay minerals. Based on IAEG (1979) Vp classification, the tuffs were classified as 'Low-Moderate' while the rhyolite was classified as 'High'.

Permeability in rock masses is dependent on two factors. These are a) rock blocks and b) discontinuities. In the sonic tests conducted in the laboratory, it was observed that Vp-dry values were higher than Vp-sat. values in some of the vitric tuffs while in other vitric tuffs, Vp-sat. values were higher than Vp-dry values. Generally, as weathering degree increases, the ratio of the clay minerals also increases and consequently, permeability increases up to a certain level. The increased permeability causes water to fill the pore spaces, crystal rims and microfractures in the rock material, which results in higher Vp-sat values than Vp-dry values as observed in Slope F (SF) for example.

At advanced stages of weathering, however, very high ratios of clay minerals occur in the microfractures in the rock material. The clay minerals fill the pore spaces and block the free flows of water thereby reducing permeability considerably. In this case, Vp-dry values are higher than Vp-sat. values.

Uniaxial Compressive Strength (UCS) values for dry and saturated(sat.) specimens ranged between 13.25- 25.32 MPa and 7.89-14.64 MPa respectively in the highly weathered tuffs, 16.89-26.95 MPa and 10.38-19.92 MPa respectively in the moderately weathered tuffs and between 34.01-40.66 MPa and 22.43-32.85 MPa respectively in the slightly weathered tuffs. The rhyolite unit had UCS values of 50.46 MPa and 44.88 MPa for dry and saturated specimens respectively.

UCS-saturated/UCS-dry ratios were calculated for the volcanic tuffs and the rhyolite (Table 5.1). Generally, UCS-sat. /UCS-dry ratios were observed to decrease with increasing degree of weathering. The average values obtained were 0.57 for HW tuff, 0.68 for MW tuff, and 0.73 for SW tuff. The rhyolite unit had a UCS-sat. /UCS-dry ratio of 0.89.

Based on Bieniawski (1989) UCS classification, the tuffs were classified as 'Very low-Low strength' while the rhyolite was classified as 'Medium strength'. Inverse linear relations were found between UCS and porosity and between Point Load Index and porosity.

Table 5.1 Vp and UCS-dry/UCS-sat. ratios

Slope	Lithology	Vp-dry (m/s)	Vp-sat (m/s)	UCS-dry (MPa)	UCS-(sat.) (MPa)	UCS-sat/UCS-dry	Weathering Degree
S1	Vitric Tuff	2777.1	2606.2	23.91	12.75	0.53	HW
S2	Lithic Tuff	4189.7	3801.5	34.01	22.43	0.66	SW
S3	Vitric Tuff	3385.7	3080.2	25.32	14.64	0.58	HW
SC	Lithic Tuff	4268.7	4086.4	40.66	32.85	0.81	SW
SD	Vitric Tuff	2909.5	2724.5	13.25	7.89	0.60	HW
SE	Vitric Tuff	3204.7	2874.6	16.89	10.38	0.61	MW
SF	Vitric Tuff	3497.9	3614.7	26.95	19.92	0.74	MW
SG	Rhyolite	4328.3	4239.4	50.46	44.88	0.89	SW

Weathering grade was successfully determined based on field observations, and physico-mechanical laboratory tests. Low unit weight and UCS values were observed in the HW tuff. The HW tuffs also had high porosity values compared to the MW and SW tuffs. It was observed that as weathering degree increases unit weight and UCS values decrease. Slake durability (Id) index values were also useful in weathering degree determination. During the Id-index test, the highest losses in dry mass were recorded in the HW tuffs while the least losses in dry mass were recorded in the SW tuffs and rhyolite. Generally, higher degrees of weathering were observed in the vitric tuffs compared to the lithic tuffs.

XRD analyses indicated that the discontinuity infill material was mainly smectite derived from weathered volcanic tuff. The occurrence of smectite in high quantities in the discontinuities puts the stability of the slope at risk due to its great swell potential.

5.1.2 Slope Stability

The potential of planar, wedge and toppling failures occurring were identified in the kinematic analysis conducted. SC, SD and SE have planar failure potentials. S3 and SG have toppling and wedge failure potentials.

Finite element analysis, which was conducted using phase[2] under various conditions of saturation and seismic activity, provide detailed information about how the slopes will behave in different situations. SRF calculated under dry conditions indicate that S3, SC and SE are unsafe (SRF<1.2). The others have SRF greater than 1.2 under this condition. SRF calculated with the piezometric line at the toe of the slope was the same as the SRF calculated under dry conditions. This indicates that the slopes are not affected when the piezometric surface is at the toe of the slope.

Reductions in SRF occurred in all the slopes when SRF was calculated with the piezometric line at the middle of the slope. SRF values reduced from 1.03 to 0.88 in S3, 0.9 to 0.84 in SC, from 1.3 to 1.2 in SD, from 0.93 to 0.84 in SE, from 1.43 to 1.28 in SF and from 2.44 to 2.0 in SG.

Significant reductions in SRF were recorded in all the slopes when SRF was calculated with the piezometric line at the top of the slope. All the slopes in the exception of SG had SRF values less than 1 under this condition. The slopes are therefore likely to fail should the piezometric surface rise to this level.

SRF values calculated under seismic conditions (0.1g and 0.2g) indicate a great effect of seismic activity on the slopes. Significant reductions in SRF were recorded with peak ground accelerations of 0.1 and 0.2g in all the slopes. All the slopes, except SG had SRF values less than 1 under 0.2g.

5.2 Conclusions

Based on the field, laboratory and software analyses conducted, the following conclusions were drawn:

a. The rocks which form the Bağarası-Foça (Izmir) State Highway slopes are vitric tuffs (andesitic and rhyolitic), lithic tuffs (andesitic and rhyolitic) and rhyolite. Main mineralogical components of the tuffs are plagioclase, pumice, sanidine and quartz.

b. The tuffs are classified as 'Very low-Low strength' while the rhyolite is classified as 'Medium strength' based on Bieniawski (1989) UCS classification. UCS values of the tuffs are generally less than 40 MPa. Generally, UCS-saturated/UCS-dry ratios decrease with increasing degree of weathering. The lithic tuff have higher UCS and p-wave velocity values than the vitric tuff.

c. As porosity values increase, unit weight, point load index and UCS values decrease. As unit weight values increase, p-wave velocity values increase.

d. The vitric tuffs easily undergo weathering and slaking compared to the lithic tuff. As such, the lithic tuff has better engineering properties than the vitric tuff.

e. Kinematic analyses show that the state highway has potential planar, wedge and toppling failure risks. Finite element analysis with phase^2 software indicates that some parts of the Bağarası-Foça (Izmir) State Highway have a high risk of failure. The analyses also showed that pore pressure and seismic activities could negatively affect the stability of the slopes.

5.3 Recommendations

a. Modifications should be made to the slope angle/height of the State highway slopes especially in areas where this study has shown that failure could occur. In plane and wedge failure risk zones, the slope angles should be reduced such that the discontinuities would not daylight. In zones of toppling failure risk, the slope height should be reduced where possible by the construction of berms or catch-benches. Gabions should also be constructed to prevent falling blocks from causing danger to traffic.

b. Effective and regular monitoring of the State Highway slopes should be done to quickly identify failing zones.

REFERENCES

Abramson, L. W., Lee, T. S., Sharma, S., & Boyce, G. M. (2002). *Slope stability and stabilization methods (2nd ed.)*, John Wiley & Sons, New York, USA, 712 pp.

Agostini, S., Tokçaer, M., & Savaşçin, M. (2010). Volcanic rocks from Foça-Karaburun and Ayvalık-Lesvos Grabens (Western Anatolia) and their Petrogenic-geodynamic significance. *Turkish Journal of Earth Sciences (Turkish J. Earth Sci.)* 19, 157–184.

Akay, E. (2000). *Magmatic and tectonic evolution of the Yuntdağ volcanic complex (Western Anatolia)*. PhD Thesis, Dokuz Eylül University, İzmir [unpublished].

Akay, E., & Erdoğan, B., (2001). Formation of Subaqueous Felsic Dome and Accompanying Pyroclastic Deposits on the Foça Peninsula (Izmir). *International Geology Review,* 43, 7, 661-674.

Akay, E., & Erdoğan, B. (2004). Evolution of neogene calc-alkaline to alkaline volcanism in the Aliağa-Foça region (Western Anatolia, Turkey). *Journal of Asian Earth Sciences* 24(3): 367-387.

Altunkaynak, Ş. & Yilmaz, Y. (2000). Foça yöresinin jeolojisi ve aktif tektoniği, Batı Anadolu [Geology and active tectonics of Foça region, Western Anatolioa]. *Batı Anadolu'nun Depremselliği Sempozyumu (BADSEM 2000)*, Abstracts Book, 160–165.

American Society for Testing and Materials (2014). *Standard test methods for compressive strength and elastic moduli of intact rock core specimens under varying states of stress and temperatures (D7012 – 14)*, ASTM International, West Conshohocken, PA.

American Society for Testing and Materials (2016). *Standard test method for splitting tensile strength of intact rock core specimens (D3967-16).* ASTM International, West Conshohocken, PA.

American Society for Testing and Materials (2016). *Standard test method for performing laboratory direct shear strength tests of rock specimens under constant normal force (D5607-16).*ASTM International, West Conshohocken, PA.

American Society for Testing and Materials (2016). *Standard test method for determination of the point load strength index of rock and application to rock strength classifications (ASTM D5731-16).*ASTM International, West Conshohocken, PA.

Andreis, R. R., Zalba, P. E. & Morosi, M.E. (2007). Composition and diagenetic processes of sandstone and tuff deposits of the Cenomanian Cardiel Formation, Cardiel Lake Area, Province Of Santa Cruz. *Revista de la Asociación Geológica Argentina* 62, (2), 257- 266.

Baron, I.**,** Cilek V., Krejci O., Melichar R. & Hubatka F. (2004). Natural hazards and earth system sciences structure and dynamics of deep-seated slope failures in the Magura Flysch Nappe, outer Western Carpathians (Czech Republic)**.** *Natural Hazards and Earth System Sciences* 4: 549–562.

Bieniawski, Z.T. (1973). Engineering classification of jointed rock masses. *Trans South African Insitute of Civil Engineering* 15(12):335–344.

Bieniawski, Z. K. (1989). *Engineering rock mass classification*. USA. John Wiley and Sons.

Canal, A. & Akin, M. (2016). Assessment of rock slope stability by probabilistic-based slope stability probability classification method along highway cut slopes in Adilcevaz-Bitlis (Turkey). *Journal of Mountain Science,* 13(11), 1893-1909.

Demirbasa, N. (2005). *Engineering Properties of Tuffs in Çeşme (Izmir)*. M.Sc. Thesis, Dokuz Eylül University. Izmir.

Dilek, Y., Altunkaynak S. & Oner Z. (2009). Syn-extensional granitoids in the Menderes Core Complex and the Late Cenozoic Extensional tectonics of the Aegean Province. *Geological Society, London, Special Publications*, 321, 197–223.

Dora, O., Savaşçin, M.Y., Kun, N. & Candan, O. (1987). Post metamorphic plutons in the menderes masif. *Hacettepe University Earth Science Journal* 14, 79–89.

Environmental Systems Research Institute (ESRI). (2009). ArcGIS Release 9.3. Redlands, CA.

Futalan, K.M., Biscaro, J.R.D., Saturay, R.M., Catane S.G., Amora M.S. & Villaflor E.L. (2010). Assessment of Potential Slope Failure Sites at Mt. Can-Abag, Guinsaugon, Philippines, Based On Stratigraphy and Rock Strength. *Bulletin of Engineering Geology and the Environ*ment, 69,517–521.

Forti, P. & Parise, M. (2008). The role of weathering in favouring instability processes in natural karst caves. In *Weathering as predisposing factor to slope movements*. Edited by D. Calcaterra , D. Campbell & M. Parise . Geolological   Society of London, Engineering Series special publication.

Ghosh, S., Kumar, A. & Bora, A. (2014). Analyzing the stability of a failing rock slope for suggesting suitable mitigation measure: a case study from the Theng Rockslide, Sikkim Himalayas, India. *Bulletin of Engineering Geology and the Environment.* 73(4):931-945.

Goodman, R. E. (1980). *Introduction to Rock Mechanics* (Chapter 8). USA. John Wiley, Toronto.

Hack, R. (2002). An evaluation of slope stability classification. *Proceedings of the Eurock, Funchal, Madeira, Portugal*, 3-22.

Hack, H.R.G.K (1998). *Slope Stability Probability Classification*, *SSPC*. (2nd Edition) The Netherlands: ITC, Enschede.

Hatzor, Y.H. & Levin M. (1997). The Shear Strength of Clay-Filled Bedding Planes in Limestones - Backanalysis of A Slope Failure in A Phosphate Mine, Israel. *Geotechnical and Geological Engineering,* 15, 263-282.

Hoek, E., & Bray J.W. (1981). *Rock slope engineering.* London: Institution of Mining and Metallurgy.

Hoek, E., Read J., Karzulovic, A. & Chen, Z.Y. (2000). Rock slopes in civil and mining engineering. *Proceedings of the International Conference on Geotechnical and Geological Engineering*. GeoEng2000, Melbourne.

Hosseinitoudeshki, V. (2014). Stability analysis of rock slopes (case study: rock slopes in the Taham Road). *Global Journal of Multidisciplinary and Applied Sciences (GJMAS) Journal* 86-91.

Hudson, J.A & Harrison, J.P. (1997). *Engineering rock mechanics-an introduction to the principles*. Oxford. Elsevier Science.

Hunt, R. E. (2005). *Geotechnical engineering investigations handbook.* (Second Edition). UK. CRC Press.

Hunt, R. E. (2007). *Geologic hazards: a field guide for geotechnical engineers.* USA. Taylor & Francis Group.

IAEG (1979). Classification of rocks and soils for engineering geological mapping. Part 1—Rock and soil materials. *Bulletin of the International Association of Engineering Geol*ogists, 19:364-71.

ISRM. (2007).*The Complete ISRM Suggested Methods for Rock Characterization, Testing and Monitoring: 1974-2006*, (Ulusay, R. and Hudson, J.A., Editors). Ankara. Kozan Ofset Matbaacılık.

Irigaray, C., El Hamdouni, R., Jiménez-Perálvarez, J. D. Fernández, P., & Chacón. J. (2012). Spatial stability of slope cuts in rock massifs using GIS technology and probabilistic analysis. *Bulletin of Engineering Geology and the Environment. 71*,569–578.

Kaşmer, O., Ulusay R. & Geniş M. (2013). Assessments on the stability of natural slopes prone to toe erosion, and man-made historical semi-underground openings carved in soft tuffs at Zelve open-air museum (Cappadocia, Turkey). *Engineering Geology, 158*, Pages 135–158.

Kaya, A., Akgün, A., Karaman, K., & Bulut, F. (2016). Understanding the mechanism of slope failure on a nearby highway tunnel route by different slope stability analysis methods: a case from NE Turkey. *Bulletin of Engineering Geology and the Environment 75* (3), 945-958.

Kaya, O. (1981). Miocene reference section for the coastal part of west Anatolia. *Newsletters of Stratigraphy*, *10*, 164–191.

Kaya, O. (1978). Orta Doğu Ege' nin neojen stratigrafisi ve tektoniği [Neogene stratigraphy and tectonics of the Middle East Aegian Region]. *JK Bülteni Cilt 22*, 1, 35-38.

Kentli, B. & Topal T. (2004). Assessment of rock slope stability for a segment of the Ankara-Pozanti Motorway, Turkey. *Engineering Geology 74*(1-2), 73-90.

Khanlari, G.R. & Mohammadi S.D. (2005). Instability assessment of slopes in heavily jointed limestone rock. *Bulletin of Engineering Geology and the Environment, 64*(3), 293-299.

Kincal, C. (2014). Application of two new stereographic projection techniques to slope stability problems. *International Journal of Rock Mechanics & Mining Sciences, 66*,136-150.

Kincal, C., Akgun A. & Koca M.Y. (2009). Landslide susceptibility assessment in the Izmir (West Anatolia, Turkey) city center and its near vicinity by the Logistic Regression Method. *Environmental Earth Science. 59*, 745–756.

Kliche, C.A. (1999). *Rock* slope *stability*. Colorado, Society for Mining, Metallurgy, and Exploration.USA.

Koca, M.Y., & Kıncal C., (2004). Abandoned stone quarries in and around the Izmir city centre and their geo-environmental impacts—Turkey. *Engineering Geology 75*, 49–67.

Le Bas, M.J. & Streckeisen, A. L. (1991). The IUGS systematics of igneous rocks. *Journal* of *the Geological Society, London 148*, 825-833.

Li, X.Z. & Xu Q. (2016). Application of the SSPC method in the stability assessment of highway rock slopes in the Yunnan Province of China. *Bulletin of Engineering Geology and the Environment*, *75* (2): 551-562.

Lips, A.L.W., Cassard, D., Sözbilir, H., Yilmaz, H. & Wijbrans, J. (2001). Multistage Exhumation of the Menderes Massif, Western Anatolia (Turkey). *International Journal of Earth Sciences 89*, 781–792.

Maleki, M.R. (2011). Study of the engineering geological problems of the Havasan dam, with emphasis on clay-filled joints in the right abutment. *Rock Mechanics Eng*. 44:695–710.

Miscevic, P. & Vlastelica G. (2014). Impact of weathering on slope stability in soft rock mass. *Journal of Rock Mechanics and Geotechnical Engineering,* 6:240‑250.

Muti, I. (2009). *Engineering Geology of the Foça Tuffs.* M.Sc. Thesis, Dokuz Eylül University, Izmir.

Nakipoğlu, G. (1994). *Yenibağarası Köyü Çevresinin Genel Jeolojisi [General geology of Yenibağarası and its surrounding areas]*, Final year project. Dokuz Eylül University, Izmir.

Oztekin, B., Topal T. & Kolat C. (2006). Assessment of degradation and stability of a cut slope in limestone, Ankara-Turkey. *Engineering Geology,* 84(1-2), 12-30.

Pantelidis, L. (2011). A critical review of highway slope instability risk assessment systems. *Bulletin of Engineering Geology and the Environment 70*, (3), 395-400.

Panthi, K.P. & Nilsen B. (2006). Numerical analysis of stresses and displacements for the Tafjord slide, Norway. *Bulletin of Engineering Geology and the Environment*, *65*(1), 57-63.

Park, H., West, T.R. & Woo, I. (2005). Probabilistic analysis of rock slope stability and random properties of discontinuity parameters, interstate highway 40, Western North Carolina, USA. *Engineering Geology*, *79*, 230-250.

Pettijohn, F.J., Potter, P.E., & Siever, R. (1987). *Sand and sandstone (Second Edition).* New York .Springer-Verlag.

Piteau, D.R., & Martin D.C. (1982). Mechanics of rock slope failure. In *Stability in Surface Mining, Vol. 3*. Edited by C.O. Brawner. New York: Society of Mining Engineers of the American Institute of Mining, Metallurgical, and Petroleum Engineers.

Qi, C., Wu J., Liu J., & Kanungo, D.P. (2016). Assessment of complex rock slope stability at Xiari, Southwestern China. *Bulletin of Engineering Geology and the Environment, 75* (2), 537-550.

Regmi, A.D., Yoshida K., Dhital M.R. & Devkota, K. (2012). Effect of rock weathering, clay mineralogy, and geological structures in the formation of large landslide, a case study from Dumre Besei Landslide, Lesser Himalaya Nepal. *Landslides, 10*, 1–13.

Rocscience (2002). *Dips user's guide*. Canada: Rocscience Inc.

Rocscience (1999). *Dips 5.0-Graphical and statistical analysis of orientation data*. Rocscience. Canada.

Rocscience (2001). *RocPlane Version 2.0 - Planar sliding stability analysis for rock slopes.Toronto*, Ontario, Canada.

Rocscience, (2006). *Phase2: Finite element analysis for excavations and slopes. Rocscience*. Canada.

Rocscience (2006). *Swedge Version 5.0 - 3D Surface wedge analysis for slopes. Toronto, Ontario*, Canada

RocLab (2012). *Rock mass strength analysis using the generalized hoek–brown failure criterion, version 1.0*. Rocscience. Canada.

Romana, M. (1985). New Adjustment Rating for Application of the Bieniawski Classification to Slopes. *Proceedings of the International Symposium on Rock Mechanics and Mining and Civil Works, ISRM, Zacatecas, Mexico*, 59–63.

Romana, M. (1988). Practice of SMR Classification for Slope Appraisal. *Proceedings of the 5th international symposium on landslides, Rotterdam*, 2:1227–1233.

Savaşçin, M.Y. (1978). *Foça-Urla neojen Volkanitlerinin mineralojik jeokimyasal incelenmesi ve kökensel yorumu [Mineralogy geochemistry and interpretation of foça-urla neogene volcanics]*. Dissertation Thesis, Dokuz Eylül University [unpublished, in Turkish with English abstract].

Schmidt, A., Li A., Lim K., & Nepal K. (2016). *Slope stability analysis using Phase^2, In Geo-China 2016 GSP 267*, American Society of Civil Engineers.

Şengör, A.M.C. & Yilmaz, Y. (1981). Tethyan evolution of Turkey: A plate tectonic approach. *Tectonophysics 75*, 181–241.

Shaban., A., Khawlie M. R. & Kheir R. B. (2001). Assessment of road instability along a typical mountainous road using GIS and aerial photos, Lebanon - Eastern Mediterranean. *Bulletin of Engineering Geology and the Environment 60*(2), 93-101.

Sharma, R. K., Mehta B.S. & Jamwal C.S. (2012). Cut slope stability evaluation of NH-21 along Nalayan-Gambhrola Section, Bilaspur District, Himachal Pradesh, India. *Natural Hazards, 66*, 249–270.

Shuib, M.K., Taib, S.H. & Abdullah, M. (2006). Discontinuity controlled cut-slope failures on weathered low grade metamorphic rocks along the East-West Highway, Grik to Jeli. *Geological Society of Malaysia Bulletin, 52,* 43-53.

Singh, R., Umrao, R.K. & Singh, T.N. (2014). Stability evaluation of road-cut slopes in the Lesser Himalaya of Uttarakhand, India: Conventional and Numerical Approaches. *Bulletin of Engineering Geology and the Environment 73*(3):845-857.

Transportation Research Board (1978). *Landslides Analysis and Control*. Special Report 176, R. L. Schuster, and R. J. Krizek (Eds.), National Academy of Science, Washington, D.C., p. 234.

Ulusay, R. (2013). Harmonizing Engineering Geology With Rock Engineering On Stability of Rock Slopes. In X. Feng, J.A. Hudson & F. Tan (eds). *Rock Characterisation, Modelling and Engineering Design Methods, 11-13*. Proceedings of the 3rd ISRM Sinorock Symposium, Tongji University, Shanghai, China. UK: Taylor & Francis Group.

Varnes, D. J. (1978). Slope movement types and processes. In R.I. Schuster & R.J. Krizek (eds.), *Landslide Analysis and Control*, National Academy of Sciences, National Research Council, Highway Research Board Special Report 176, 11–33.

Wyllie, D. C., & Mah C. W. (2004). *Rock slope engineering (civil and mining) (4th Edition).* London. Taylor & Francis Group.

Yagiz, S. (2011). P-Wave velocity test for assessment of geotechnical properties of some rock materials. *Bulletin of Material Science, 34*(4):947–953.

Yilmaz I, Marschalko M, Yildirim M, Dereli E, & Bednarik M. (2012). GIS-based kinematic slope instability and slope mass rating (SMR) maps: application to a railway route in Sivas (Turkey). *Bulletin of Engineering Geology and the Environment 71*, 351–357.

Zhang, F., Liu G., Chen W., Han W. & Bai S. (2010). Engineering geology and stability of the Jishixia Landslide, Yellow River, China. *Bulletin of Engineering Geology and the Environment*, *69*(1), 99–103.

APPENDICES

A.1: Geological map of the study area

The geological map of the study area is presented in the back pocket.

A.2: Table of values -Physical properties of the rocks

Specimen no.	Sub. weight in water (g)	Sat. Weight in air (g)	Dry weight (g)	Bulk volume (cm³)	Pore volume (cm³)	Dry unit weight (g/cm³)	n%	Sat. unit weight (g/cm³)
1Ai	161.92	335.98	305.47	174.06	30.51	1.75	17.53	1.93
1Bi	226.25	459.76	421.21	233.51	38.55	1.80	16.51	1.97
1Ci	177.91	364.69	331.82	186.78	32.87	1.78	17.60	1.95
1Di	214.90	447.13	409.94	232.23	37.19	1.77	16.01	1.93
1Ei	199.94	415.18	376.20	215.24	38.98	1.75	18.11	1.93
1Fi	214.27	443.36	398.50	229.09	44.86	1.74	19.58	1.94
1Gi	212.50	441.93	398.78	229.43	43.15	1.74	18.81	1.93
1Hi	205.56	431.24	391.29	225.68	39.95	1.73	17.70	1.91
1Ii	245.90	497.84	456.78	251.94	41.06	1.81	16.30	1.98
1Ji	204.12	423.41	387.61	219.29	35.80	1.77	16.33	1.93
1Ki	194.14	404.75	366.21	210.61	38.54	1.74	18.30	1.92
1Li	212.75	442.89	404.13	230.14	38.76	1.76	16.84	1.92
1Mi	183.44	381.23	345.35	197.79	35.88	1.75	18.14	1.93
1Ni	208.60	429.10	389.49	220.50	39.61	1.77	17.96	1.95
1Oi	185.01	385.59	351.72	200.58	33.87	1.75	16.89	1.92
1Pi	188.14	390.35	355.64	202.21	34.71	1.76	17.17	1.93
1Ri	152.38	308.94	278.23	156.56	30.71	1.78	19.62	1.97
1Si	173.24	348.70	321.24	175.46	27.46	1.83	15.65	1.99
1Ti	213.94	428.75	395.83	214.81	32.92	1.84	15.33	2.00
2B	283.12	532.08	506.05	248.96	26.03	2.03	10.46	2.14
2C	294.05	545.80	518.56	251.75	27.24	2.06	10.82	2.17
2K	310.95	586.46	564.30	275.51	22.16	2.05	8.04	2.13
2H	217.98	401.60	383.85	183.62	17.75	2.09	9.67	2.19
2B	283.12	532.08	506.05	248.96	26.03	2.03	10.46	2.14
21E	351.42	612.05	594.88	260.63	17.17	2.28	6.59	2.35
23K	163.86	279.49	272.96	115.63	6.53	2.36	5.65	2.42
21J	333.15	592.92	570.59	259.77	22.33	2.20	8.60	2.28
2I	194.66	362.04	348.48	167.38	13.56	2.08	8.10	2.16
21F	334.90	594.77	574.79	259.87	19.98	2.21	7.69	2.29
2L	274.30	530.62	507.17	256.32	23.45	1.98	9.15	2.07
2F	177.98	345.51	329.74	167.53	15.77	1.97	9.41	2.06
2Ai	419.56	806.23	771.35	386.67	34.88	1.99	9.02	2.09
2Bi	419.50	796.85	761.01	377.35	35.84	2.02	9.50	2.11
2Di	396.01	758.64	735.64	362.63	23.00	2.03	6.34	2.09
2Ei	452.70	852.82	823.08	400.12	29.74	2.06	7.43	2.13
2Fi	409.86	768.76	739.25	358.90	29.51	2.06	8.22	2.14

131

A.2: Table of values -Physical properties (cont.)

Specimen no.	Sub. weight in water (g)	Sat. Weight in air (g)	Dry weight (g)	Bulk volume (cm³)	Pore volume (cm³)	Dry unit weight (g/cm³)	n%	Sat. unit weight (g/cm³)
2Gi	350.51	669.49	639.80	318.98	29.69	2.01	9.31	2.10
2Hi	331.00	636.74	614.88	305.74	21.86	2.01	7.15	2.08
2Ii	357.71	676.48	648.74	318.77	27.74	2.04	8.70	2.12
3Ai	245.54	493.50	447.10	247.96	46.40	1.80	18.71	1.99
3Bi	235.47	477.70	426.29	242.23	51.41	1.76	21.22	1.97
3Ci	234.62	483.30	434.57	248.68	48.73	1.75	19.60	1.94
3Di	238.78	487.68	431.64	248.90	56.04	1.73	22.52	1.96
3Ei	232.78	471.98	422.70	239.20	49.28	1.77	20.60	1.97
3Fi	222.28	452.93	406.32	230.65	46.61	1.76	20.21	1.96
3Gi	205.58	423.52	372.73	217.94	50.79	1.71	23.30	1.94
3Hi	189.22	383.38	348.86	194.16	34.52	1.80	17.78	1.97
3Ii	174.82	355.67	317.88	180.85	37.79	1.76	20.90	1.97
3Ji	160.82	328.08	290.58	167.26	37.50	1.74	22.42	1.96
3A	247.72	506.04	446.01	258.32	60.03	1.73	23.24	1.96
3B	243.13	497.16	438.49	254.03	58.67	1.73	23.10	1.96
3C	208.63	418.54	377.15	209.91	41.39	1.80	19.72	1.99
3D	248.36	507.44	447.35	259.08	60.09	1.73	23.19	1.96
3E	248.18	507.36	449.47	259.18	57.89	1.73	22.34	1.96
3F	188.07	383.17	339.12	195.10	44.05	1.74	22.58	1.96
3G	173.81	353.88	312.80	180.07	41.08	1.74	22.81	1.97
3H	155.08	315.81	279.70	160.73	36.11	1.74	22.47	1.96
3I	96.83	197.85	173.09	101.02	24.76	1.71	24.51	1.96
3J	119.19	231.20	215.70	112.01	15.50	1.93	13.84	2.06
31L	270.54	533.21	479.28	262.67	53.93	1.82	20.53	2.03
SA1	221.51	458.95	384.21	237.44	74.74	1.62	31.48	1.93
SA2	316.43	650.11	550.36	333.68	99.75	1.65	29.89	1.95
SA3	380.08	778.25	665.24	398.17	113.01	1.67	28.38	1.95
SA4	159.10	328.34	279.63	169.24	48.71	1.65	28.78	1.94
SA5	368.55	764.23	638.10	395.68	126.13	1.61	31.88	1.93
SA9	100.98	210.36	172.67	109.38	37.69	1.58	34.46	1.92
SA11	241.59	500.48	410.44	258.89	90.04	1.59	34.78	1.93
SA12	128.40	264.86	221.05	136.46	43.81	1.62	32.10	1.94
SA13	89.15	184.32	156.19	95.17	28.13	1.64	29.56	1.94
SA14	132.48	272.24	234.23	139.76	38.01	1.68	27.20	1.95
SB1	278.70	538.52	504.40	259.82	34.12	1.94	13.13	2.07
SB3	351.69	651.60	623.06	299.91	28.54	2.08	9.52	2.17
SB7	451.03	867.34	827.23	416.31	40.11	1.99	9.63	2.08

A.2: Table of values -Physical properties (cont.)

Specimen no.	Sub. weight in water (g)	Sat. Weight in air (g)	Dry weight (g)	Bulk volume (cm³)	Pore volume (cm³)	Dry unit weight (g/cm³)	n%	Sat. unit weight (g/cm³)
SB8	394.35	740.09	714.88	345.74	25.21	2.07	7.29	2.14
SB9	256.69	474.59	455.60	217.90	18.99	2.09	8.72	2.18
SB11	306.85	584.60	561.56	277.75	23.04	2.02	8.30	2.10
SB13	395.52	744.51	711.42	348.99	33.09	2.04	9.48	2.13
SB14	249.59	480.84	459.84	231.25	21.00	1.99	9.08	2.08
SB16	228.14	420.73	403.97	192.59	16.76	2.10	8.70	2.18
SB18	353.22	668.21	642.99	314.99	25.22	2.04	8.01	2.12
SB19	421.82	807.45	773.76	385.63	33.69	2.01	8.74	2.09
SB20	326.07	647.12	598.58	321.05	48.54	1.86	15.12	2.02
SB21	405.07	778.31	737.64	373.24	40.67	1.98	10.90	2.09
SB22	252.59	501.02	467.20	248.43	33.82	1.88	13.61	2.02
SB23	215.80	422.63	396.41	206.83	26.22	1.92	12.68	2.04
SB24	337.08	625.07	599.34	287.99	25.73	2.08	8.93	2.17
SB27	260.54	482.02	465.30	221.48	16.72	2.10	7.55	2.18
SB31	232.03	431.10	413.00	199.07	18.10	2.07	9.09	2.17
SB32	202.79	385.32	365.70	182.53	19.62	2.00	10.75	2.11
SC1	185.31	344.91	333.31	159.60	11.60	2.09	7.27	2.16
SC2	221.13	428.48	406.50	207.35	21.98	1.96	10.60	2.07
SC3	245.61	466.09	444.53	220.48	21.56	2.02	9.78	2.11
SC5	182.27	345.12	329.27	162.85	15.85	2.02	9.73	2.12
SC8	173.30	325.18	313.51	151.88	11.67	2.06	7.68	2.14
SC9	224.11	417.38	405.22	193.27	12.16	2.10	6.29	2.16
SC10	229.02	430.01	415.19	200.99	14.82	2.07	7.37	2.14
SC12	322.93	612.42	591.15	289.49	21.27	2.04	7.35	2.12
SC13	219.53	389.42	377.26	169.89	12.16	2.22	7.16	2.29
SC13A	274.05	524.33	497.18	250.28	27.15	1.99	10.85	2.09
SC14A	210.13	398.83	383.27	188.70	15.56	2.03	8.25	2.11
SC16A	319.13	604.06	578.88	284.93	25.18	2.03	8.84	2.12
SC17	249.92	473.30	453.94	223.38	19.36	2.03	8.67	2.12
SC21	245.75	460.42	443.75	214.67	16.67	2.07	7.77	2.14
SC32	179.80	346.93	330.75	167.13	16.18	1.98	9.68	2.08
SD2	114.78	230.37	200.37	115.59	30.00	1.73	25.95	1.99
SD3	192.12	387.85	342.68	195.73	45.17	1.75	23.08	1.98
SD4	268.52	533.74	493.26	265.22	40.48	1.86	15.26	2.01
SD5	200.87	411.51	346.06	210.64	65.45	1.64	31.07	1.95

A.2: Table of values -Physical properties (cont.)

Specimen no.	Sub. weight in water (g)	Sat. Weight in air (g)	Dry weight (g)	Bulk volume (cm³)	Pore volume (cm³)	Dry unit weight (g/cm³)	n%	Sat. unit weight (g/cm³)
SD6	177.57	359.68	325.27	182.11	34.41	1.79	18.90	1.98
SD12	242.78	481.48	444.08	238.70	37.40	1.86	15.67	2.02
SD13	263.67	518.12	477.00	254.45	41.12	1.87	16.16	2.04
SD16	318.56	634.14	579.23	315.58	54.91	1.84	17.40	2.01
SD20	248.35	494.25	458.48	245.90	35.77	1.86	14.55	2.01
SD21	147.75	300.55	260.63	152.80	39.92	1.71	26.13	1.97
SD24	240.20	486.63	428.24	246.43	58.39	1.74	23.69	1.97
SD25	247.27	494.55	439.19	247.28	55.36	1.78	22.39	2.00
SD6	177.57	359.68	325.27	182.11	34.41	1.79	18.90	1.98
SD12	242.78	481.48	444.08	238.70	37.40	1.86	15.67	2.02
SD13	263.67	518.12	477.00	254.45	41.12	1.87	16.16	2.04
SD16	318.56	634.14	579.23	315.58	54.91	1.84	17.40	2.01
SD20	248.35	494.25	458.48	245.90	35.77	1.86	14.55	2.01
SD21	147.75	300.55	260.63	152.80	39.92	1.71	26.13	1.97
SD24	240.20	486.63	428.24	246.43	58.39	1.74	23.69	1.97
SD25	247.27	494.55	439.19	247.28	55.36	1.78	22.39	2.00
SD6	177.57	359.68	325.27	182.11	34.41	1.79	18.90	1.98
SD12	242.78	481.48	444.08	238.70	37.40	1.86	15.67	2.02
SD13	263.67	518.12	477.00	254.45	41.12	1.87	16.16	2.04
SD26	240.33	482.32	437.32	241.99	45.00	1.81	18.60	1.99
SD27	195.80	403.71	343.77	207.91	59.94	1.65	28.83	1.94
SE1	207.10	412.98	374.69	205.88	38.29	1.82	18.60	2.01
SE2	164.23	322.39	308.94	158.16	13.45	1.95	8.50	2.04
SE3	189.25	383.51	349.25	194.26	34.26	1.80	17.64	1.97
SE5	146.65	288.65	264.12	142.00	24.53	1.86	17.27	2.03
SE6	179.52	354.99	326.40	175.47	28.59	1.86	16.29	2.02
SE8	211.38	430.21	385.65	218.83	44.56	1.76	20.36	1.97
SE9	252.33	483.52	456.23	231.19	27.29	1.97	11.80	2.09
SE10	210.65	417.49	386.99	206.84	30.50	1.87	14.75	2.02
SE11	250.13	497.47	459.10	247.34	38.37	1.86	15.51	2.01

A.2: Table of values -Physical properties (cont.)

Specimen no.	Sub. weight in water (g)	Sat. Weight in air (g)	Dry weight (g)	Bulk volume (cm³)	Pore volume (cm³)	Dry unit weight (g/cm³)	n%	Sat. unit weight (g/cm³)
SE14	266.88	516.22	483.00	249.34	33.22	1.94	13.32	2.07
SE15	274.22	531.30	499.37	257.08	31.93	1.94	12.42	2.07
SE16	194.00	375.47	351.92	181.47	23.55	1.94	12.98	2.07
SE17	185.48	364.50	333.34	179.02	31.16	1.86	17.41	2.04
SE18	147.27	292.12	264.30	144.85	27.82	1.82	19.21	2.02
SE21	162.12	321.64	296.64	159.52	25.00	1.86	15.67	2.02
SE22	143.55	285.73	257.30	142.18	28.43	1.81	20.00	2.01
SF1	265.12	490.48	467.32	225.36	23.16	2.07	10.28	2.18
SF2	227.19	421.32	403.05	194.13	18.27	2.08	9.41	2.17
SF5	257.99	472.73	455.45	214.74	17.28	2.12	8.05	2.20
SF7	213.48	396.78	377.99	183.30	18.79	2.06	10.25	2.16
SF8	320.73	588.14	565.10	267.41	23.04	2.11	8.62	2.20
SF9	207.68	381.22	364.72	173.54	16.50	2.10	9.51	2.20
SF11	274.48	505.37	484.95	230.89	20.42	2.10	8.84	2.19
SF13	228.46	422.50	401.96	194.04	20.54	2.07	10.59	2.18
SF15	211.67	391.90	375.68	180.23	16.22	2.08	9.00	2.17
SF16	284.08	521.61	499.77	237.53	21.84	2.10	9.19	2.20
SF18	269.81	507.30	480.49	237.49	26.81	2.02	11.29	2.14
SF20	262.15	480.47	459.84	218.32	20.63	2.11	9.45	2.20
SG2	298.80	519.19	501.81	220.39	17.38	2.28	7.89	2.36
SG4	258.25	450.58	432.16	192.33	18.42	2.25	9.58	2.34
SG5	250.95	439.48	422.29	188.53	17.19	2.24	9.12	2.33
SG6	227.27	398.34	380.05	171.07	18.29	2.22	10.69	2.33
SG8	278.37	489.52	468.33	211.15	21.19	2.22	10.04	2.32
SG12	259.28	463.93	436.52	204.65	27.41	2.13	13.39	2.27
SG14	261.44	456.61	436.78	195.17	19.83	2.24	10.16	2.34
SG15	233.20	403.88	388.11	170.68	15.77	2.27	9.24	2.37
SG16	273.49	475.46	456.40	201.97	19.06	2.26	9.44	2.35
SG20	386.48	658.05	644.09	271.57	13.96	2.37	5.14	2.42

A.2: Table of values -Physical properties (cont.)

Specimen no.	Sub. weight in water (g)	Sat. Weight in air (g)	Dry weight (g)	Bulk volume (cm³)	Pore volume (cm³)	Dry unit weight (g/cm³)	n%	Sat. unit weight (g/cm³)
SG21	317.25	540.05	526.98	222.80	13.07	2.37	5.87	2.42
SG24	262.13	445.99	438.44	183.86	7.55	2.38	4.11	2.43
SG25	317.47	547.81	532.49	230.34	15.32	2.31	6.65	2.38
SG26	316.62	549.57	529.04	232.95	20.53	2.27	8.81	2.36
SG27	322.08	577.06	546.50	254.98	30.56	2.14	11.99	2.26
SG28	276.45	481.01	458.54	204.56	22.47	2.24	10.98	2.35
SG29	278.69	491.78	469.34	213.09	22.44	2.20	10.53	2.31
SG30	254.94	440.51	426.15	185.57	14.36	2.30	7.74	2.37
SG34	234.53	408.38	390.18	173.85	18.20	2.24	10.47	2.35
SG37	342.60	585.25	575.15	242.65	10.10	2.37	4.16	2.41

A.3: Slake durability index test results

Sample Number	Weight of Sample + Drum (A)(g)	Weight of sample + Drum (after first cycle)(B)(g)	Weight of sample + Drum (after second cycle)(C)(g)	Weight of sample + Drum (after third cycle)(D)(g)	Weight of sample + Drum (after fourth cycle)(E)(g)	Weight of sample + Drum (after fifth cycle)(F)(g)	Weight of drum(G)(g)	Id1	Id2	Id3	Id4	Id5
S1	2291.1	2247.5	2220.8	2192.7	2167.8	2138.2	1795.3	91.2	85.8	80.1	75.1	69.2
S2	2277.1	2264.1	2253.1	2247.1	2239.1	2230.1	1773.4	97.4	95.2	94.0	92.5	90.7
S3	2317.3	2282.4	2252.4	2223.4	2192.4	2160.4	1773.4	93.6	88.1	82.7	77.0	71.2
SA	2254.2	2215.9	2179.2	2142.3	2105.4	2072.2	1795.3	91.7	83.7	75.6	67.6	60.3
SB	2225.9	2207.7	2185.7	2167.1	2147.3	2135.0	1773.4	96.0	91.1	87.0	82.6	79.9
SC	2224.9	2218.5	2213.2	2207.7	2202.3	2196.6	1773.4	98.6	97.4	96.2	95.0	93.7
SD	2245.6	2205.3	2160.7	2119.9	2083.6	2040.9	1795.3	91.1	81.2	72.1	64.0	54.6
SE	2224.0	2205.9	2190.2	2175.1	2158.8	2142.5	1773.4	96.0	92.5	89.1	85.5	81.9
SF	2238.3	2224.8	2211.7	2197.9	2185.0	2173.4	1773.4	97.1	94.3	91.3	88.5	86.0
SG	2253.5	2246.2	2238.5	2229.1	2221.6	2214.5	1795.3	98.4	96.7	94.7	93.1	91.5

A.4: Shear box test results

DOKUZ EYLUL UNIVERSITESI MUHENDISLIK FAKULTESI
MADEN MÜHENDISLİĞİ BÖLÜMÜ
KAYA VE ZEMİN MEKANİĞİ LABORATUVARI

SABIT DUŞEY YUK ALTINDA KAYAÇ NUMUNELERINDE LABORATUVAR DIREKT KESME DAYANIM DENEYI
Laboratory Direct Shear Strength Tests of Rock Specimens Under Constant Normal Force

Proje						Deneyi Yapan	
Project						*Tested by*	
Kuyu No	**Derinlik**		**Örnek No**	**2**	**Kuyu Çapı**	**54**	**Tarih**	
Bore Hole	*Depth*		*Sample*		*Core Size (mm)*		*Date*	
Kayaç	**Nem**		**Uzun Eksen**	**71.00**	**Kısa Eksen**	**54.00**	**Alan (cm²)**	**30.11**
Rock Descrip.	*Moisture*		*Major Axis (mm)*		*Minor Axis (mm)*		*Area*	

DESCRIPTION OF DISCONTINUITY SURFACE	
Discontinuity Type	Joint
Roughness	Slickensided
Surface Alteration	Slightly
Infilling (gouge)	None
Aperture (mm)	None
Dip of Discontinuity	
Roughness (JRC) (0 - 20)	8-10

TESTING DATA

	Peak	
Normal Yük	**Normal G.**	**Kesme G.**
Normal Load	*Normal Stress*	*Shear Stres*
kN	kPa	kPa
0.36	106.44	203.42
0.72	216.83	274.66
1.07	350.06	342.28
	Residual	
0.36	112.49	194.99
0.72	224.98	259.98
1.07	350.06	342.28

Mohr-Coloumb Strength Parameters		
	Peak	**Residual**
Cohesion c (kPa)	-	-
Friction angle φ (°)	29.59	31.83

138

A.4: Shear box test results (cont.)

DOKUZ EYLUL UNIVERSITESI MUHENDISLIK FAKULTESI
MADEN MÜHENDISLİĞİ BÖLÜMÜ
KAYA VE ZEMİN MEKANİĞİ LABORATUVARI

Form No :KML-SCP–013

SABIT DUŞEY YUK ALTINDA KAYAÇ NUMUNELERINDE LABORATUVAR DIREKT KESME DAYANIM DENEYI
Laboratory Direct Shear Strength Tests of Rock Specimens Under Constant Normal Force

Proje / Project						Deneyi Yapan / Tested by	
Kuyu No / Bore Hole		**Derinlik** / Depth		**Örnek No** / Sample		**Kuyu Çapı** / Core Size (mm) **54**	**Tarih** / Date
Kayaç / Rock Descrip.		**Nem** / Moisture		**Uzun Eksen** / Major Axis (mm) **54.00**	**Kısa Eksen** / Minor Axis (mm) **54.00**	**Alan (cm²)** / Area **22.90**	

DESCRIPTION OF DISCONTINUITY SURFACE	
Discontinuity Type	Joint
Roughness	Slickensided
Surface Alteration	Slightly
Infilling (gouge)	None
Aperture (mm)	None
Dip of Discontinuity	
Roughness (JRC) (0 - 20)	10-12

TESTING DATA		
Peak		
Normal Yük	**Normal G.**	**Kesme G.**
Normal Load	Normal Stress	Shear Stres
kN	kPa	kPa
0.36	106.44	237.33
0.72	216.83	320.43
1.07	350.06	399.32
Residual		
0.36	112.49	227.48
0.72	224.98	303.31
1.07	350.06	399.32

Mohr-Coloumb Strength Parameters		
	Peak	**Residual**
Cohesion c (kPa)	-	-
Friction angle φ (°)	33.52	35.91

139

A.5: Scanline mapping

A.5.1: Slope 3 (S3) scanline mapping

SET I	**SET II**	**SET III**
Scanline Length : 12.2 m	Scanline Length: 12.2 m	Scanline Length: 13,1 m
No. of discontinuities : 41	No. of discontinuities : 24	No. of discontinuities : 17
λ : 3.36 m^{-1}	λ : 1.9 m^{-1}	λ : 1.3 m^{-1}
S : 0.29 m	S : 0.5 m	S : 0.7 m

A.5.2: Slope G (SG) scanline mapping
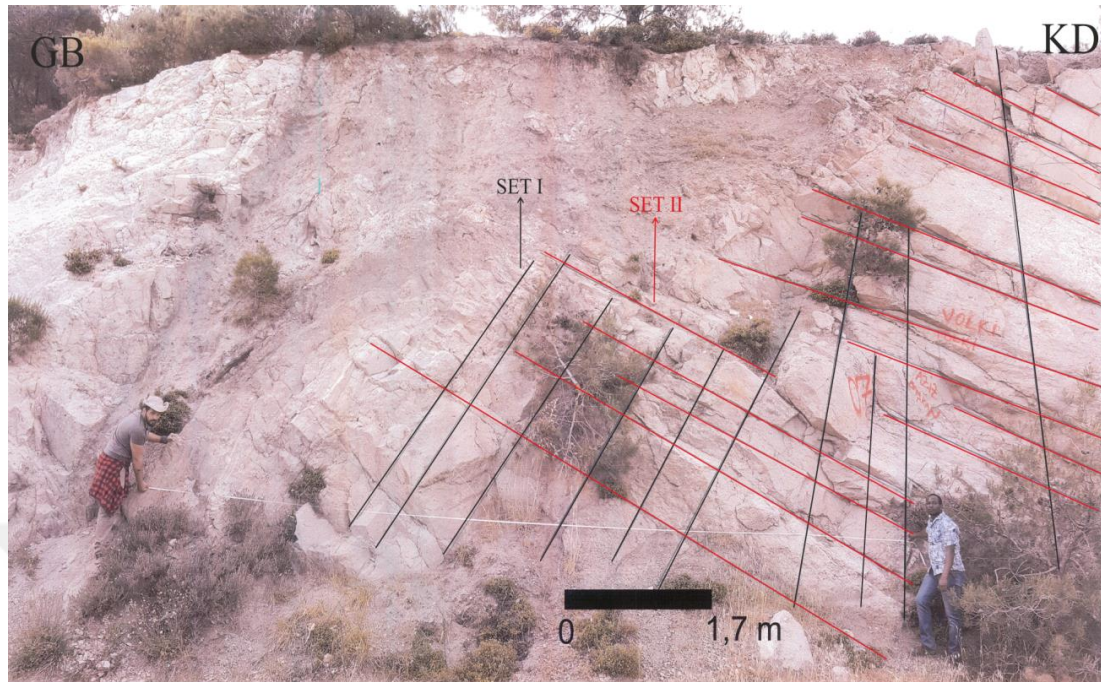
SET I	SETII
Scanline Length : 3.02 m	Scanline Length: 5.14 m
No. of discontinuities : 14	No. of discontinuities : 25
λ : 4.6 m^{-1}	λ : 4.9 m^{-1}
S : 0.22 m	S : 0.2 m

A.5.3 Slope C (SC) scanline mapping
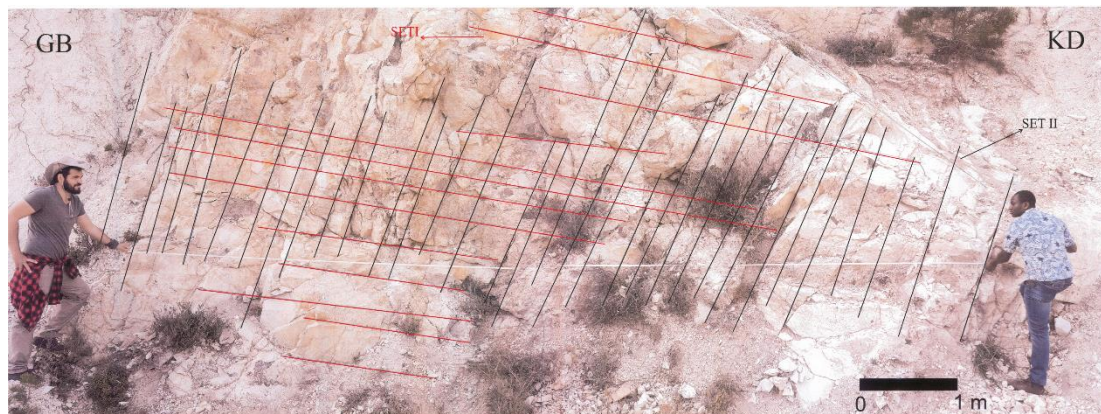
SET I	SETII
Scanline Length : 7.6 m	Scanline Length: 6.3 m
No. of discontinuities : 9	No. of discontinuities : 15
λ : 1.18 m^{-1}	λ : 2.3 m^{-1}
S : 0.8 m	S : 0.42 m